

**Azimuthal angular distributions  
of  $K^+$  and  $K^-$  mesons  
from Au+Au collisions  
at a kinetic beam energy of 1.5 AGeV**

Dissertation  
zur Erlangung des Doktorgrades  
der Naturwissenschaften

vorgelegt am Fachbereich Physik  
der Johann Wolfgang Goethe-Universität  
in Frankfurt am Main

von  
**Mateusz Płoskoń**  
aus Krakau

Frankfurt 2005  
(D F 1)

vom Fachbereich Physik der  
Johann Wolfgang Goethe-Universität als Dissertation angenommen.

Dekan: Prof. Dr. Assmus  
Gutachter: Prof. Dr. Senger, Prof. Dr. Ströbele  
Datum der Disputation: 21. Dezember 2005

## Abstract

The Kaon-Spectrometer (KaoS) at the heavy-ion synchrotron (SIS) at the Gesellschaft für Schwerionenforschung (GSI) in Darmstadt has been used to study production and propagation of  $K^+$  and  $K^-$  mesons from Au+Au collisions at a kinetic beam energy of 1.5 AGeV. This energy for  $K^+$  mesons is close to the corresponding production threshold in binary nucleon-nucleon collisions and far below for  $K^-$  mesons. The azimuthal angular distributions of particles as a function of the collision centrality and particle transverse momenta have been measured.

The properties of strange mesons are expected to be modified by the in-medium meson-baryon potential. Theoretical calculations show that the superposition of the scalar and vector potentials leads to a small repulsive  $K^+N$  and a strong attractive  $K^-N$  potential. Additionally, the interaction of kaons and antikaons with nuclear matter is different. The strangeness conservation law inhibits the absorption probability of  $K^+$  mesons as they contain an  $\bar{s}$ -quark.  $K^-$  mesons, however, interact with nucleons via *strangeness-exchange* ( $K^-N \rightarrow Y\pi$ , where  $Y = \Lambda, \Sigma$ ). Moreover, the reverse process ( $\pi Y \rightarrow K^-N$ ) is the dominant production mechanism of  $K^-$  mesons at SIS energies.

The azimuthal angular emission patterns of kaons are expected to be sensitive to the in-medium potentials. An enhanced out-of-plane emission of  $K^+$  mesons was observed in Au+Au reactions at 1.0 AGeV and 1.5 AGeV, and also in Ni+Ni at 1.93 AGeV. The out-of-plane emission of  $K^+$  mesons in Au+Au reactions at 1.0 AGeV was interpreted as a consequence of a repulsive  $K^+N$  potential in the nuclear medium, however, recent transport calculations show that the emission patterns obtained in Au+Au at 1.5 AGeV and Ni+Ni at 1.93 AGeV are additionally influenced by the re-scattering of kaons. For  $K^-$  mesons the calculations predict an almost isotropic emission pattern due to the attractive  $K^-N$  potential which counteracts the absorption of  $K^-$  mesons in the spectator fragments. In Ni+Ni collisions at 1.93 AGeV the azimuthal distribution of  $K^-$  mesons has been found to be isotropic. In this case, however, the spectators are rather small and have large relative velocities. In addition, the delay of antikaon emission due to strangeness-exchange reaction minimizes the interaction with the spectators. As a consequence the sensitivity of the  $K^-$  meson emission pattern to the  $K^-N$  in-medium potential is reduced. In Au+Au collisions we found a dependence of the  $K^-$  meson azimuthal emission pattern on the transverse momentum. The antikaons registered with  $p_t < 0.5$  GeV/c are preferentially emitted in the reaction plane and the particles with  $p_t > 0.5$  GeV/c show strong out-of-plane enhancement. The emission patterns of  $K^-$  can be explained in terms of two competing phenomena: one of them is indeed the influence of the attractive  $K^-N$  potential, however, the second one originates from the strangeness-exchange process.

## Abstract

### Einleitung

Mit dem Kaonen-Spektrometer (KaoS) am Schwerionen-Synchrotron (SIS) der Gesellschaft für Schwerionenforschung (GSI) in Darmstadt wurde die Produktion und Propagation von  $K^+$  und  $K^-$  Mesonen in Au+Au Kollisionen bei einer kinetischen Strahlenergie von 1,5 AGeV untersucht. Diese Energie liegt nahe der Produktionsschwelle für  $K^+$  Mesonen in binären Nukleon-Nukleon Kollisionen und weit unter derjenigen für  $K^-$  Mesonen. Die azimuthalen Winkelverteilungen der Teilchen als Funktion der Stoßzentralität sowie ihre Transversalimpulsverteilungen wurden gemessen.

Für Mesonen mit Strangeness wird eine Modifikation ihrer Eigenschaften durch Meson-Baryon-Potentiale in Materie erwartet. Theoretische Rechnungen zeigen, daß die Überlagerung des skalaren und des Vektorpotentials zu einem leicht repulsiven  $K^+N$  und einem stark attraktiven  $K^-N$  Potential führen. Desweiteren ist die Wechselwirkung von Kaonen und Antikaonen mit Kernmaterie unterschiedlich. Die Erhaltung der Strangeness vermindert die Absorptionswahrscheinlichkeit für  $K^+$  Mesonen, da diese ein  $\bar{s}$ -quark enthalten.  $K^-$  Mesonen dagegen wechselwirken mit Nukleonen durch den *strangeness-exchange* Kanal ( $K^-N \rightarrow Y\pi$ , mit  $Y = \Lambda, \Sigma$ ). Gleichzeitig ist der umgekehrte Prozeß ( $\pi Y \rightarrow K^-N$ ) der dominante Produktionsmechanismus für  $K^-$  Mesonen bei SIS Energien.

Es wird erwartet, daß die azimuthale Verteilung der Kaonenemission sensitiv auf In-Medium Potentiale ist. Eine bevorzugte Emission senkrecht zur Reaktionsebene wurde für  $K^+$  Mesonen in Au+Au Reaktionen bei 1,0 AGeV und 1,5 AGeV sowie in Ni+Ni Reaktionen bei 1,93 AGeV beobachtet. In Au+Au Reaktionen bei 1,0 AGeV wurde dies als Konsequenz eines repulsiven  $K^+N$  Potentials in Kernmaterie interpretiert. Neuere Transportmodellrechnungen zeigen allerdings, daß die azimuthalen Verteilungen in Au+Au bei 1,5 AGeV und in Ni+Ni Stößen bei 1,93 AGeV zusätzlich durch die elastische Streuung der Kaonen beeinflußt werden. Für  $K^-$  Mesonen sagen die Rechnungen eine im wesentlichen isotrope Verteilung voraus, bedingt durch das attraktive  $K^-N$  Potential, welches der Absorption der  $K^-$  Mesonen in den Spektator Fragmenten entgegenwirkt. In Ni+Ni Kollisionen bei 1,93 AGeV wurde eine isotrope azimuthale Verteilung der  $K^-$  Mesonen gefunden. In diesem Fall sind die Spektatoren allerdings relativ klein und haben große Relativgeschwindigkeiten. Zusätzlich wird die Wechselwirkung der Antikaonen mit den Spektatoren durch ihre späte Emission verringert. Als Konsequenz hiervon ist die Sensitivität der azimuthalen Verteilung von  $K^-$  Mesonen auf  $K^-N$  in-Medium Potentiale reduziert.

In Au+Au Kollisionen wurde eine Abhängigkeit der azimuthalen Verteilung der  $K^-$  Emission vom Transversalimpuls beobachtet. Antikaonen mit  $p_t < 0,5$  GeV/c werden bevorzugt innerhalb der Reaktionsebene emittiert, solche mit  $p_t > 0,5$  GeV/c zeigen dagegen eine stark bevorzugte Emission senkrecht zur Reaktionsebene. Dieses Emissionsverhalten der  $K^-$  kann durch zwei konkurrierende Phänomene erklärt werden: Eines

davon ist tatsächlich der Einfluß des attraktiven  $K^-N$  Potentials, das andere dagegen basiert auf dem strangeness-exchange Prozeß.

### Experimentaufbau

Das in dieser Arbeit behandelte Experiment wurde im Sommer 2001 an der GSI durchgeführt. Der verwandte Teilchenstrahl hatte eine kinetische Energie von  $295.5 \text{ GeV}$  ( $1.5 \text{ AGeV}$ ) und bestand aus Goldkernen  $^{197}\text{Au}^{79+}$ . Die Intensität betrug  $5 \cdot 10^8$  pro Strahlpuls bei einer Pulslänge von etwa 10 ns. Nach der primären Beschleunigung im Linearbeschleuniger UNILAC wurden nicht vollständig ionisierte Ionen ( $^{197}\text{Au}^{63+}$ ) in das Synchrotron SIS injiziert und auf etwa  $0.3 \text{ AGeV}$  beschleunigt. Von dort wurde der Strahl zum Speicherring ESR geleitet und vollständig ionisiert. Im ESR Ring wurde der Strahl mit einem Elektronenkühler zur Minimierung seiner Transversalimpulskomponenten gekühlt. Der letzte Abschnitt des Zyklus war eine zweite Beschleunigung im Synchrotron SIS bis zur vollen Strahlenergie. Ein Zyklus dauerte etwa 30 Sekunden. Im Experiment wurde ein Goldtarget ( $^{197}\text{Au}$ ) von 0.5 mm Dicke verwendet, welches einer Wechselwirkungswahrscheinlichkeit von 1.8% entspricht.

Der Experimentaufbau besteht aus dem Kaonenspektrometer KaoS und weiteren Detektoren. Das Spektrometer besteht aus einem Quadrupol- und einem Dipolmagnet und hat eine große Akzeptanz sowohl im Impuls ( $p_{max}/p_{min} \approx 2$ ) als auch im Raumwinkel ( $\Omega \leq 35 \text{ msr}$ ). Die Teilchenidentifikation wird durch gleichzeitige Messung von Trajektorien und Flugzeit ermöglicht. Die Flugzeitmessung erfolgte über den Unterschied zwischen den Zeitsignalen zweier Detektoren (D und F), die jeweils aus mehreren Szintillationsmodulen bestehen, welche an beiden Enden von Photovervielfacherröhren ausgelesen werden. Der D-Detektor, der das Startsignal liefert, befindet sich zwischen dem Quadrupol und dem Dipol. Der Flugzeitstopp-Detektor (F) befindet sich in der Fokalebene des Spektrometers. Eine zweite Flugzeitmessung wurde zwischen dem Großwinkelhodoskop (T-Detektor) und dem F-Detektor durchgeführt. Der T-Detektor besteht aus 84 Szintillationsmodulen, die in drei Ringen mit unterschiedlichen Polarwinkeln ( $12^\circ \leq \theta_{lab} \leq 48^\circ$ ) um den Targetpunkt angeordnet sind. Die Anzahl der angesprochenen Module diente zur Bestimmung der Stoßzentralität. Die Teilchentrajektorien im Spektrometer wurden mit Hilfe dreier Vieldrahtproportionalkammern (MWPC) rekonstruiert. Eine dieser Kammern (L) befindet sich zwischen dem Quadrupol und dem Dipol. Die beiden anderen (M und N) befinden sich zwischen dem Dipol und dem F-Detektor. Um hochenergetische Kaonen besser von Protonen unterscheiden zu können, befindet sich hinter der Fokalebene noch ein Cherenkov-Detektor. Die Strahlintensität wurde mit einem Plastikszintillationsteleskop bestimmt, das auf das Target ausgerichtet ist. Die Orientierung der Reaktionsebene wurde mit Hilfe der Trefferverteilung im Kleinwinkelhodoskop bestimmt, das sich 7 m strahlabwärts befindet. Die 380 Szintillationsmodule des Hodoskops sind in drei Gruppen unterschiedlicher Größe aufgeteilt und um die Strahlachse herum angeordnet. Sie decken einen Polarwinkelbereich von  $0^\circ$  bis  $8^\circ$  ab. Die Datenaufnahme ermöglichte Messungen mit unterschiedlichen Triggerbedingungen. Neben einem "Minimum-Bias-Trigger" wurde ein sogenannter "Spektrometer-Trigger" eingerichtet, der ein Signal generiert, sobald ein Teilchen im Spektrometer nachgewiesen wird. Um zusätzlich Pionen und Protonen zu unterdrücken und den niedrigen Produktionswirkungsquerschnitt für Kao-

nen bei SIS Energien zu kompensieren, wurde ein spezieller “Kaonen-Flugzeit-Trigger” eingerichtet.

Das Datenaufnahmesystem basierte auf dem GSI-Standard MBS (*Multi Branch System*). Die Zeit- und Energieverlustsignale wurden mit Analog-zu-Digital-Konvertern umgewandelt. Daten aus den Modulen im FASTBUS Überrahmen wurden per VSB-Bus zu einer Reihe E7-VME Rechnern übermittelt. Die Signale der Vieldrahtproportionalkammern wurden digitalisiert und durch ein *Event Builder Interface* zur Aufzeichnung durch ein DLT (*Digital Linear Tape*) Bandlaufwerk vorbereitet. Die Experimentsteuerung bestand aus fünf CAMAC Überrahmen, die über VSB-Bus verbunden waren. Einer der Überrahmen war mit einem E6 Rechner verbunden um eine Ethernet-Verbindung herzustellen. Die Module in diesen Überrahmen kontrollieren die Schwellen für die Diskriminatoren und die Hochspannungen für die Szintillatoren und Cherenkov-Detektoren. Desweiteren liefert einer der CAMAC-Überrahmen Statusinformationen über die Trigger Einstellungen und dient zur Auslese des Strahlintensitätsmonitors. Ein “Master-Slave Serial-Bus”-System wurde für die Targetpositionierung und die Kontrolle der Magnetstromversorgung genutzt.

### Datenanalyse

Der erste Schritt der Datenanalyse war die Eichung der Detektoren. Die Signale der Flugzeitdetektoren wurden mit Hilfe des Simulationspackets GEANT unter Berücksichtigung aller Materialien, der Detektorgeometrie und der vermessenen Magnetfeldkarte angepaßt. Die Teilchentrajektorien wurden anhand der Trefferpositionen in den Vieldrahtproportionalkammern rekonstruiert und mit den getroffenen Modulen im D- und F-Detektor korreliert. Die so ermittelten Spurkandidaten wurden mit Teilchentrajektorien verglichen, die mit Monte-Carlo-Simulationen mit dem Packet GEANT generiert wurden. Die Länge der Flugstrecken zwischen allen Kombinationen von D- und F-Modulen und die Teilchenimpulse pro Ladung  $p/Z$  wurden mit den Flugzeitmessungen kombiniert, um das Verhältnis von Masse über Ladung  $m/Z$  zu bestimmen. Die Unterdrückung des Untergrunds aus zufälligen Koinzidenzen und Vielfachstreuung erfolgte über die Anwendung von Auswahlkriterien auf die Unterschiede zwischen GEANT-Trajektorien und gemessenen Spurkandidaten wie auch auf die Unterschiede zwischen den zwei Flugzeitmessungen. Der Stoßparameter und die durchschnittliche Anzahl partizipierender Nukleonen wurde im Rahmen des nuklearen Überlappmodells von Eskola berechnet. Dieses Modell beschreibt Kern-Kern-Stöße als Überlapp binärer Nukleon-Nukleon-Stöße. Unter Verwendung des Überlappmodells und unter der Annahme, daß das integrierte Multiplizitätsspektrum der T-Detektors unter “Minimum-Bias”-Triggerbedingungen proportional zum totalen Reaktionswirkungsquerschnitt ist, kann der Stoßparameterbereich und die mittlere Anzahl partizipierender Nukleonen für jede Zentralitätsklasse abgeschätzt werden. Insgesamt wurden die Daten in fünf Zentralitätsklassen eingeteilt. Für die Analyse der azimutalen Teilchenemission mußte die azimutale Orientierung der Reaktionsebene rekonstruiert werden. Hierfür wurde eine Variation der Fourierkoeffizientenanalyse angewandt. Für jedes Ereignis wird der  $n$ -te Fourierkoeffizient  $\vec{Q}_n = \sum_{i=1}^N w_i e^{in\phi_i} = (Q_n^x, Q_n^y)$  definiert, wobei  $N$  die gemessene Teilchenmultiplizität des Ereignisses ist,  $\phi_i$  der Azimutwinkel des Teilchens  $i$  und  $w_i$  ein Wichtungsfaktor.

Normalerweise wird als Wichtungsfaktor  $w_i$  die transversale Energie des Teilchens  $i$  oder sein Transversalimpuls verwandt. Im Falle des in diesem Experiment verwandten Detektors genügt die Wahl  $w_i = \sin(\theta_i)$ , wobei  $\theta_i$  der Polarwinkel des Teilchens  $i$  relativ zur Strahlachse ist, bestimmt aus den Trefferpositionen im Kleinwinkelhodoskop. Die resultierende Orientierung der Reaktionsebene wurde nach  $\Phi_{RP} = \arctan(\frac{Q_n^y}{Q_n^x})|_{n=1}$  bestimmt. Daraufhin kann das azimutale Emissionsmuster einer gewählten Teilchensorte bestimmt und nach  $\frac{dN}{d\phi} \approx 1 + 2v_1 \cos(\phi) + 2v_2 \cos(2\phi)$  parametrisiert werden. Hierbei ist  $\phi$  der azimutale Emissionswinkel relativ zur Orientierung der Reaktionsebene und  $v_1$  und  $v_2$  sind die Asymmetrieparameter zur beschreibung des gerichteten und des elliptischen Flusses. Bei der Bestimmung dieser Parameter muß berücksichtigt werden, daß die experimentelle Bestimmung der Reaktionsebene durch die Detektorakzeptanz, die Detektorauflösung und durch Fluktuationen auf Grund der beschränkten Teilchenzahl beschränkt ist. Der gemessene Azimutwinkel  $\psi$  für ein Ereignis kann vom tatsächlichen Azimutwinkel  $\phi$  um einen Wert  $\Delta\phi$  abweichen. Daher wurde eine Prozedur zur Bestimmung von Korrekturparametern entwickelt und auf die resultierenden Parameter angewandt, so daß die in dieser Arbeit gezeigten Verteilungen auf die Auflösung der Reaktionsebene korrigiert sind.

### Experimentelle Ergebnisse

Als Ergebnis der Datenanalyse wurden die Produktionswirkungsquerschnitte für Pionen und Kaonen bestimmt. Für Protonen in semi-peripheren Stößen ( $b > 6.4 fm$ ) bei Targedrapidität wurde kollektiver Fluß beobachtet und die Abhängigkeit des gerichteten Flusses von Rapidity und Transversalimpuls entspricht den Erwartungen. Die für Kaonen und Antikaonen gemessene grosse Statistik bei mittlerer Rapidity ( $0.2 < y/y_n < 0.6$ ) und in semi-peripheren Stößen ( $b > 6.4 fm$ ) ermöglichte die Bestimmung der azimutalen Emissionsmuster auch für diese Teilchen. Die azimutale Emission der  $K^+$  und  $K^-$  Mesonen wurde weiterhin mit der der Pionen verglichen. Sowohl  $\pi^+$  als auch  $\pi^-$  zeigen eine ausgeprägte Emission senkrecht zur Emissionsebene. Dieser negative elliptische Fluß kann durch den Produktionsmechanismus, hauptsächlich über die  $\Delta$ -Resonanz, und Abschattungseffekte erklärt werden. Diese Emission senkrecht zur Reaktionsebene ist konstant über den gemessenen Transversalimpulsbereich ( $0.3 < p_t < 0.8$ ). Das gleiche Verhalten wurde für Kaonen beobachtet. Diese zeigen eine bevorzugte Emission senkrecht zur Reaktionsebene und ihr azimutales Emissionsmuster zeigt kaum eine Transversalimpulsabhängigkeit. Dies ist bemerkenswert, da für Kaonen die Wechselwirkungswahrscheinlichkeit innerhalb der Reaktionszone deutlich kleiner ist als für Pionen. Über den Transversalimpuls integriert zeigt die azimutale Verteilung der  $K^-$  bei mittlerer Rapidity das gleiche Verhalten wie die für  $K^+$ . Die Analyse der Emissionsmuster als Funktion des Transversalimpulses zeigt, daß  $K^-$  Mesonen mit  $p_t < 0.5$  GeV nahezu isotrop emittiert werden während  $K^-$  mit  $p_t > 0.5$  eine starke Präferenz für eine Emission senkrecht zur Reaktionsebene zeigen. Eine feinere Unterteilung im Transversalimpuls zeigt eine starke Abhängigkeit des elliptischen Flusses der  $K^-$  Mesonen. Der Übergang von einer bevorzugten Emission senkrecht zur Reaktionsebene zu einer bevorzugten Emission in die Reaktionsebene läßt auf eine hohe Sensitivität dieser azimutalen Emissionsmuster auf die Reaktionsdynamik schließen. Die Vorhersagen sagen

ein annähernd isotropes Emissionsmuster für  $K^-$  Mesonen als Konsequenz eines Ausgleichs zwischen dem attraktiven  $K^-N$  Potential und der großen Streu- und Absorptionswahrscheinlichkeit der  $K^-$  in den Spektorfragmenten vor.

### Vergleich mit theoretischen Modellen

Theoriemodelle sagen die Existenz von Kaon-Nukleon-Potentialen voraus, die eine wichtige Rolle in dichter und heißer Materie spielen, zum Beispiel die Veränderung von Kaonenmassen bewirken. Die Potentiale beeinflussen auch die Produktionswirkungsquerschnitte: Die Schwelle für die  $K^-$ -Produktion wird abgesenkt während sie für die  $K^+$  erhöht wird. Als Konsequenz erhöht sich die  $K^-$ -Ausbeute in Schwerionenkollisionen bei Strahlenergien unterhalb der Schwelle deutlich. Im Gegensatz dazu wird für die  $K^+$ -Ausbeute eine Verkleinerung vorhergesagt. Ein Vergleich der invarianten Wirkungsquerschnitte von  $K^+$  und  $K^-$  Mesonen bei  $\Theta_{CM} = 90^\circ$  mit verschiedenen mikroskopischen Transportrechnungen wird gezeigt. Im Fall der  $K^+$  Mesonen können die Daten keines der präsentierten Modelle ausschließen. Die Ergebnisse der Rechnungen mit In-Medium-Potentialen (zum Beispiel Chirale Störungsrechnung und G-Matrix) unterscheiden sich nicht von denjenigen ohne  $K^+N$  Potential. Die  $K^-$  Wirkungsquerschnitte dagegen scheinen die Rechnungen mit Kaon-Nukleon-Potentialen zu bevorzugen. Die Tatsache, daß die In-Medium-Potentiale unterschiedlich auf die beiden Kaonarten wirken hat Untersuchungen des  $K^-/K^+$ -verhältnisses als Observable, die noch sensitiver auf In-Medium-Effekte ist, angeregt. Die theoretischen Modelle zeigen, daß sich das Verhältnis als Funktion der kinetischen Energie, der transversalen Masse oder der Anzahl partizipierender Nukleonen mit und ohne In-Medium-Potentiale sowohl in Form als auch im absoluten Wert unterscheiden. Tatsächlich zeigt die Analyse von C+C Reaktionen bei 1.8 AGeV, durchgeführt am Kaonenspektrometer, eine starke Abhängigkeit des  $K^-/K^+$ -Verhältnisses von der kinetischen Energie. In dieser Arbeit wurde das  $K^-/K^+$ -Verhältnis für das deutlich schwerere Stoßsystem Au+Au bei 1.5 AGeV ausgewertet und mit verschiedenen Modellen verglichen. Die Daten scheinen die Rechnungen mit In-Medium-Potentialen für  $E_{cm}^{kin} > 0.12 GeV$  zu bevorzugen. Für niedrigere Energien kann das gemessene Verhältnis von keinem Modell erklärt werden.

Die berechneten Emissionsmuster für  $K^+$  Mesonen stimmen mit den experimentell bestimmten gut überein, ohne eine bestimmte Rechnung zu bevorzugen. Die Transversalimpulsabhängigkeit des elliptischen Flusses der Kaonen zeigt, daß der Einfluß der Potentiale auf die  $K^+$  nicht sehr ausgeprägt ist und es ist im Rahmen der experimentellen Unsicherheiten unmöglich zwischen den verschiedenen Modellen zu unterscheiden. Die Modelle sagen sogar voraus, daß die bevorzugte Emission senkrecht zur Emissionsebene teilweise ohne In-Medium-Potentiale erklärt werden kann. Im Falle von  $K^+$  Mesonen aus Au+Au-Stößen bei 1.0 AGeV war dies anders. Die bevorzugte Emission senkrecht zur Reaktionsebene in Modellrechnungen ohne In-Medium-Potentiale muß daher auf die höhere Streuwahrscheinlichkeit in den Dichten zurückgeführt werden, die in Au+Au Kollisionen bei 1.5 AGeV erreicht werden. Weitere Informationen zur Unterscheidung lassen sich aus der azimuthalen Winkelverteilung der  $K^-$  Mesonen extrahieren. Das Emissionsmuster bevorzugt Rechnungen, die eine bevorzugte Emission der Antikaonen senkrecht zur Reaktionsebene vorhersagen. Das gemessene "squeeze-out" Signal widerspricht frühe-



ren Vorhersagen und der Chiralen Störungsrechnung. Das Verhalten der Daten wird sowohl durch G-Matrix als auch den freien Fall (dass heisst, ohne KN Potentiale), der auch eine moderate Bevorzugung der Emission senkrecht zur Reaktionsebene zeigt, reproduziert. Ein Vergleich des gemessenen elliptischen Flusses der  $K^-$  Mesonen als Funktion des Transversalimpulses mit den Rechnungen zeigt, daß die Daten für hohe  $p_t$  besser durch diejenige mit In-Medium-Effekten nach dem G-Matrix Ansatz beschrieben werden, in welchem die Antikaonenproduktion durch den Seltsamkeitsaustausch dominiert wird. Die Chirale Störungsrechnung kann den elliptischen Fluß der Antikaonen bei hohen Transversalimpulsen nicht beschreiben. Auf der anderen Seite liegen die Chirale Störungsrechnung wie auch die Rechnungen ohne In-Medium-Potentiale naeher an den Daten bei niedrigen  $p_t$ , wo der Fluß in die Reaktionsebene beobachtet wird. Der Übergang von Fluß in die Ebene zu Fluß aus der Ebene wird jedoch von keinem der Modelle beschrieben. Das Emissionsmuster der  $K^-$  kann durch zwei konkurrierende Phänomäne erklärt werden: eines ist tatsächlich der Einfluß des attraktiven  $K^-N$  Potentials, das zweite dagegen der Seltsamkeitsaustausch-Prozess.

# Contents

<b>1</b>	<b>Introduction</b>	<b>1</b>
1.1	Strange and antistrange meson production . . . . .	2
1.2	In-medium effects . . . . .	3
1.3	Collective flow phenomena and azimuthal emission pattern . . . . .	5
<b>2</b>	<b>Experimental Setup</b>	<b>9</b>
2.1	Magnet system . . . . .	10
2.2	Trigger . . . . .	10
2.3	Time-Of-Flight measurement . . . . .	12
2.4	Tracking detectors . . . . .	13
2.5	Beam normalization detectors . . . . .	13
2.6	Target detector . . . . .	14
2.7	Small Angle Hodoscope . . . . .	14
2.8	Data acquisition and the slow control . . . . .	15
<b>3</b>	<b>Data analysis procedure</b>	<b>19</b>
3.1	TOF Calibration . . . . .	19
3.2	Small angle hodoscope calibration . . . . .	19
3.2.1	The time calibration . . . . .	20
3.2.2	The energy calibration . . . . .	20
3.3	Tracking and particle identification . . . . .	21
3.3.1	Trajectory reconstruction . . . . .	22
3.3.2	Particle mass determination . . . . .	23
3.3.3	Definition of the tracking cuts . . . . .	23
3.4	Event centrality estimation . . . . .	25
3.5	Reaction plane determination . . . . .	28
3.6	Reaction plane normalization . . . . .	30
3.7	Reaction plane resolution . . . . .	33
3.7.1	Method description . . . . .	33
3.7.2	Calculation of the correction parameters . . . . .	34

<b>4</b>	<b>Experimental results</b>	<b>37</b>
4.1	The Measurement . . . . .	37
4.2	Particle yields . . . . .	37
4.3	Production cross-sections . . . . .	38
4.4	Azimuthal angular distributions . . . . .	44
4.4.1	Collective flow measurements close to target rapidity . . . . .	44
4.4.2	Elliptic flow measurements . . . . .	51
<b>5</b>	<b>Discussion</b>	<b>59</b>
5.1	Sensitivity of kaon production to in-medium effects . . . . .	59
5.2	Elliptic flow - the observations . . . . .	61
5.2.1	Pions close to mid-rapidity . . . . .	61
5.2.2	Kaons and antikaons close to mid-rapidity . . . . .	63
5.3	Elliptic flow - the observable for KN potentials ? . . . . .	65
5.4	What do we actually observe ? . . . . .	67
<b>6</b>	<b>Summary and outlook</b>	<b>71</b>
<b>A</b>	<b>Obtaining double differential cross-sections</b>	<b>73</b>
A.1	Acceptance corrections . . . . .	74
A.2	Trigger efficiencies . . . . .	74
A.3	MWPC's efficiencies . . . . .	75
A.4	Tracking efficiencies . . . . .	76
A.5	Cut efficiencies . . . . .	76
A.6	Dead time correction . . . . .	77
A.7	The beam normalization . . . . .	78
A.8	Systematic error estimations . . . . .	78
<b>B</b>	<b>Invariant cross-section</b>	<b>80</b>

# List of Figures

1.1	<i>Two gold nuclei centrally colliding at a beam energy of 2.0 AGeV presented at 3 different stages - left: just before the collision, middle - the dense phase of the overlapping nuclei, right - the reaction participants and products flying away from the collision zone. . . . .</i>	2
1.2	<i>Predictions on the kaon and antikaon energy modifications: the gray shaded bands represent the range of results from various model calculations (see [JSBB97] and references therein). . . . .</i>	4
1.3	<i>Reaction plane defined by the impact parameter <math>b</math> and the beam axis. . . .</i>	5
1.4	<i>Schematic presentations of heavy-ion collisions with beam axis pointing into the picture. Letters <math>P</math> and <math>T</math> stand for projectile and target accordingly. Arrows present the preferred directions of sideflow. Enhanced emission of particles oriented at <math>0^\circ</math> and <math>\pm 180^\circ</math> degrees with respect to the reaction plane denotes a correlation towards either projectile or target nucleus. Overlapping region of the two nuclei is the high density phase of the collision. . . . .</i>	6
1.5	<i>Two collision figures similar as in fig. 1.4, however here the arrows refer to the <u>elliptic flow</u> component. A back-to-back symmetric emission at <math>0^\circ</math> and <math>\pm 180^\circ</math> degrees is an in-plane flow and an enhanced emission of particles towards <math>\pm 90^\circ</math> degrees is an out-of-plane flow (often called squeeze-out). . . . .</i>	6
1.6	<i><math>K^+</math> azimuthal angular distribution measured in semi-central (<math>b</math> 5-10fm) Au+Au collisions at 1 AGeV around mid-rapidity (0.1 0.6) for <math>K^+</math> transverse momenta of 0.2 GeV/c pt 0.8 GeV/c. The lines represent results of RBUU calculations for an impact parameter of <math>b=7</math>fm [LKB96] without (dashed line) and with an in-medium KN potential (solid line). Both calculations take into account kaon-nucleon re-scattering [S<sup>+</sup>98]. . . . .</i>	7
1.7	<i>Theoretical calculations of the azimuthal angular emission pattern of <math>K^-</math> mesons at 1.8 AGeV with their preselected transverse momentum <math>p_t &gt; 0.5</math> GeV at a moderate centrality <math>b = 8</math>fm. The two curves present the expected influence of the mean field potential on the azimuthal angular distributions of antikaons [WFFGB99]. . . . .</i>	7
2.1	<i>Sketch of the Kaon Spectrometer and its detector system . . . . .</i>	10

2.2	<i>The layout sketch of the logic (left figure) and timing (right figure) of the trigger. . . . .</i>	11
2.3	<i>Time of flight as a function of the F detector paddle number for different particle species and three different magnetic field setting (0.6T - left, 0.9T - middle, 1.4T - right). . . . .</i>	12
2.4	<i>Target detector - cross section. . . . .</i>	14
2.5	<i>Small Angle Hodoscope. . . . .</i>	15
2.6	<i>Schematic sketch of the data acquisition system and the slow control [Koc05, Pło99]. . . . .</i>	16
3.1	<i>Energy deposition <math>\frac{dE}{dx}</math> for hits in the hodoscope as a function of the particles velocities <math>\beta</math>. . . . .</i>	22
3.2	<i>Mass per charge spectra showing the measured data with the Kaon trigger and also after applying the cuts defined with formulas 3.7, 3.8 and 3.10 for 3 different selection windows (<math>n = 1,2,3</math>). Data sample acquired with the spectrometer angle <math>\Theta_{spec} = 48^\circ</math> and magnetic field settings 0.9T</i>	24
3.3	<i>Distributions of the cut variables defined in eq. 3.7, 3.8 and 3.10 for each of the magnetic field settings. From top to bottom in rows: 0.9T, 1.4T. From left to right in columns: <math>L_{Geant}^X - L_{data}^X</math>, <math>N_{Geant}^Y - N_{data}^Y</math> and <math>\beta^{norm} = \frac{\frac{1}{\beta_F} - \frac{1}{\beta_{TF}}}{\frac{1}{\beta_F}}</math>. . . . .</i>	25
3.4	<i>Cut parameters for each of the magnetic field settings. From top to bottom in rows: 0.9T, 1.4T. From left to right in columns: <math>\sigma_{D_i}^{LX}</math>, <math>\sigma_{D_i}^{NY}</math>, <math>\sigma_{D_i}^\beta</math>. . . . .</i>	26
3.5	<i>Target detector multiplicity spectrum separated into 5 centrality classes - used in the centrality estimation of an event and the average nucleon participant number. . . . .</i>	27
3.6	<i>Numbers of participating nucleons of the target and the projectile as a function of the collisions impact parameter. Result of the nuclear overlap model calculation [Mis04]. . . . .</i>	28
3.7	<i>Minimum bias normalization procedure (see text). For each of the centrality bins (columns from LHS least central to most central on RHS) the upper row shows uncorrected data, the middle row shows the <math>dN/d\phi</math> distributions after the symmetrization procedure, and finally the last row presents the distributions after the last correction. Each data sample has been fitted with a function defined by 3.29 - values showing the anisotropy presented in the graphs. . . . .</i>	31
3.8	<i>Schematic front view of the small angle hodoscope showing its granularity. Shaded elements symbolize some faulty modules. The black square in the center is empty space after removal of 4 smallest detector modules allowing free passage of the beam. The two circles define a shape, fully symmetric in the azimuthal angle. This area is taken into account in the analysis. . . . .</i>	32
3.9	<i><math>\Delta\Phi_{RP}^{data}</math> distributions for different centrality selections. . . . .</i>	35

4.1	<i>Phase space populations of <math>K^+</math> (left) and <math>K^-</math> (right) measured at spectrometer angles 40deg and 48deg.</i>	38
4.2	<i>Double differential cross-sections of measured pions (upper figure - <math>\pi^+</math>, lower figure - <math>\pi^-</math>) at different spectrometer angles as a function of the laboratory momentum.</i>	39
4.3	<i>Double differential cross-sections of measured pions (upper figure - <math>\pi^+</math>, lower figure - <math>\pi^-</math>) at different spectrometer angles as a function of the laboratory momentum compared to the previous measurements by KaoS collaboration.</i>	40
4.4	<i>Double differential cross-sections of measured kaons (upper) and antikaons (lower) at different spectrometer angles as a function of the laboratory momentum.</i>	41
4.5	<i>Double differential cross-sections of measured kaons and antikaons at different spectrometer angles as a function of the laboratory momentum compared to the previous measurements by KaoS collaboration.</i>	42
4.6	<i>Invariant cross sections of <math>K^+</math> and <math>K^-</math> as a function of the energy in the center of mass system. The data have been selected for <math>\Theta_{cm} = 90^\circ \pm 7.5^\circ</math>. Distributions were fitted with Boltzmann function defined by formula 4.2.</i>	43
4.7	<i>Phase space populations of protons measured at spectrometer angles 40deg, 48deg and 72deg.</i>	45
4.8	<i>Azimuthal angular distribution of protons from Au+Au at 1.5AGeV. Data selected as events with <math>b &gt; 6.4\text{fm}</math>, rapidity range of <math>0.05 &lt; y/y_{beam} &lt; 0.5</math> and transverse momentum <math>0.4 &lt; p_t &lt; 1.5</math>.</i>	45
4.9	<i>Azimuthal angular distributions of protons from Au+Au at 1.5AGeV for two rapidity regions: <math>0.05 &lt; y/y_{beam} &lt; 0.15</math> (left) and <math>0.15 &lt; y/y_{beam} &lt; 0.45</math> (right). Data selected with impact parameter <math>b &gt; 6.4\text{fm}</math> and transverse momentum <math>0.4 &lt; p_t &lt; 1.5</math>.</i>	45
4.10	<i>Directed and elliptic flow parameters of protons as a function of normalized rapidity. Data selected with impact parameter <math>b &gt; 6.4\text{fm}</math> and transverse momentum <math>0.4 &lt; p_t &lt; 1.5</math>.</i>	46
4.11	<i>Directed flow of protons as a function of transverse momentum. Data recorded close to target rapidity (<math>0.1 &lt; y/y_{beam} &lt; 0.23</math>) with centralities <math>b &gt; 6.4\text{fm}</math>.</i>	46
4.12	<i>Phase space populations of <math>\pi^+</math> measured at spectrometer angle 72deg.</i>	47
4.13	<i>Azimuthal angular distribution of <math>\pi^+</math> mesons from Au+Au at 1.5AGeV. Data selected as events with <math>b &gt; 6.4\text{fm}</math>, rapidity range of <math>0.05 &lt; y/y_{beam} &lt; 0.25</math> and transverse momentum <math>0.2 &lt; p_t &lt; 0.8</math>.</i>	47
4.14	<i>Azimuthal angular distribution of <math>\pi^+</math> mesons from Au+Au at 1.5AGeV. Data selected as events with <math>b &gt; 6.4\text{fm}</math>, rapidity range of <math>0.05 &lt; y/y_{beam} &lt; 0.25</math> and two transverse momentum <math>0.2 &lt; p_t &lt; 0.5</math> (left) and <math>0.5 &lt; p_t &lt; 0.8</math> (right).</i>	48

4.15	<i>Transverse momentum dependence of the asymmetry parameters <math>v_1</math> for azimuthal emission pattern of <math>\pi^+</math> measured close to target rapidity (<math>0.05 &lt; y/y_{beam} &lt; 0.25</math>) determined with formula 4.3 for non-central events (<math>b &gt; 6.4fm</math>).</i>	48
4.16	<i>Phase space populations of <math>K^+</math> measured at spectrometer angle 72deg.</i>	49
4.17	<i>Azimuthal angular distribution of <math>K^+</math> mesons from Au+Au at 1.5AGeV. Data selected as events with <math>b &gt; 6.4fm</math>, rapidity range of <math>0.05 &lt; y/y_{beam} &lt; 0.25</math> and transverse momentum <math>0.2 &lt; p_t &lt; 0.8</math>.</i>	49
4.18	<i>Azimuthal angular distribution of <math>K^+</math> mesons from Au+Au at 1.5AGeV. Data selected as events with <math>b &gt; 6.4fm</math>, rapidity range of <math>0.05 &lt; y/y_{beam} &lt; 0.25</math> and two transverse momentum <math>0.2 &lt; p_t &lt; 0.5</math> (left) and <math>0.5 &lt; p_t &lt; 0.8</math> (right).</i>	50
4.19	<i>Transverse momentum dependence of the asymmetry parameters <math>v_1</math> for azimuthal emission pattern of <math>K^+</math> measured close to target rapidity (<math>0.05 &lt; y/y_{beam} &lt; 0.25</math>) determined with formula 4.3 for non-central events (<math>b &gt; 6.4fm</math>).</i>	50
4.20	<i>Phase space populations of <math>\pi^+</math> (left) and <math>\pi^-</math> (right) measured at spectrometer angles 40deg and 48deg.</i>	51
4.21	<i>Azimuthal angular distribution of <math>\pi^+</math> (left) and <math>\pi^-</math> (right) from Au+Au at 1.5AGeV. Data selected as events with <math>b &gt; 6.4fm</math>, rapidity range of <math>0.2 &lt; y/y_{beam} &lt; 0.6</math> and transverse momentum <math>0.2 &lt; p_t &lt; 0.8</math>. Lines represent fits according to formula 4.3.</i>	52
4.22	<i>Azimuthal angular distribution of <math>\pi^+</math> mesons from Au+Au at 1.5AGeV for two transverse momentum bins: <math>0.2 &lt; p_t &lt; 0.5</math> (left) and <math>0.5 &lt; p_t &lt; 0.8</math> (right). Data selected as events with <math>b &gt; 6.4fm</math>, rapidity range of <math>0.2 &lt; y/y_{beam} &lt; 0.6</math>. Lines represent fits according to formula 4.3.</i>	52
4.23	<i>Azimuthal angular distribution of <math>\pi^-</math> mesons from Au+Au at 1.5AGeV for two transverse momentum bins: <math>0.2 &lt; p_t &lt; 0.5</math> (left) and <math>0.5 &lt; p_t &lt; 0.8</math> (right). Data selected as events with <math>b &gt; 6.4fm</math>, rapidity range of <math>0.2 &lt; y/y_{beam} &lt; 0.6</math>. Lines represent fits according to formula 4.3.</i>	53
4.24	<i>Transverse momentum dependence of the asymmetry parameter <math>v_2</math> for azimuthal emission pattern of <math>\pi^+</math> and <math>\pi^-</math> parametrized with formula 4.3.</i>	53
4.25	<i>Azimuthal angular distribution of <math>K^+</math> (left) and <math>K^-</math> (right) from Au+Au at 1.5AGeV. Data selected as events with <math>b &gt; 6.4fm</math>, rapidity range of <math>0.2 &lt; y/y_{beam} &lt; 0.6</math> and transverse momentum <math>0.2 &lt; p_t &lt; 0.8</math>. Lines represent fits according to formula 4.3.</i>	54
4.26	<i>Azimuthal angular distribution of <math>K^+</math> mesons from Au+Au at 1.5AGeV for two transverse momentum bins: <math>0.2 &lt; p_t &lt; 0.5</math> (left) and <math>0.5 &lt; p_t &lt; 0.8</math> (right). Data selected as events with <math>b &gt; 6.4fm</math>, rapidity range of <math>0.2 &lt; y/y_{beam} &lt; 0.6</math>. Lines represent fits according to formula 4.3.</i>	54

- 4.27 *Azimuthal angular distribution of  $K^-$  mesons from Au+Au at 1.5AGeV for two transverse momentum bins:  $0.2 < p_t < 0.5$  (left) and  $0.5 < p_t < 0.8$  (right). Data selected as events with  $b > 6.4\text{fm}$ , rapidity range of  $0.2 < y/y_{\text{beam}} < 0.6$ . Lines represent fits according to formula 4.3. . . . .* 55
- 4.28 *Azimuthal angular distribution of  $K^+$  mesons (left) and  $K^-$  mesons (right) from Au+Au at 1.5AGeV for 3 lowest transverse momentum bins. Data selected as events with  $b > 6.4\text{fm}$ , rapidity range of  $0.2 < y/y_{\text{beam}} < 0.6$ . Lines represent fits according to formula 4.3. . . . .* 56
- 4.29 *Azimuthal angular distribution of  $K^+$  mesons (left) and  $K^-$  mesons (right) from Au+Au at 1.5AGeV for 2 highest transverse momentum bins. Data selected as events with  $b > 6.4\text{fm}$ , rapidity range of  $0.2 < y/y_{\text{beam}} < 0.6$ . Lines represent fits according to formula 4.3. . . . .* 57
- 4.30 *Transverse momentum dependence of the asymmetry parameters  $v_2$  for azimuthal emission pattern of  $K^+$  and  $K^-$  mesons parametrized with formula 4.3. . . . .* 58
- 5.1 *Invariant cross-sections of  $K^+$  (upper plot) and  $K^-$  mesons (lower plot) reconstructed for  $\Theta_{CM} = 90^\circ \pm 7.5^\circ$  as a function of kinetic energy in the center of mass system. Comparison of the data to the theoretical models with different approaches [Bra05] for including the in-medium effects (e.g. Chiral Perturbation [MBSB<sup>+</sup>04] and G-matrix off-shell transport calculations [CTBR03]), but also without in-medium potentials. . . . .* 60
- 5.2  *$K^-/K^+$  ratio as a function of the kinetic energy in the center of mass system. Comparison of the data to the theoretical models with different approaches [Bra05] for including the in-medium effects (e.g. Chiral Perturbation [MBSB<sup>+</sup>04] and G-matrix off-shell transport calculations [CTBR03]), but also without in-medium potentials - “free” case. . . . .* 61
- 5.3 *Azimuthal angular emission patterns of  $\pi^+$ ,  $\pi^-$  mesons measured in Au+Au at 1.5 AGeV collisions close to mid-rapidity in non-central events segmented in rows accordingly. Figures of a single column correspond to one of the transverse momentum sets: without  $p_t$  selection (left column), with low  $p_t$  ( $0.2 < p_t < 0.5$  - middle column) and high  $p_t$  ( $0.5 < p_t < 0.8$  - right column). Lines represent fits according to formula 4.3. . . . .* 62
- 5.4 *Azimuthal distribution of  $\pi^+$  and  $K^+$  mesons for semi-central Au+Au collisions at 1.5 AGeV. The data are corrected for the resolution of the reaction plane and refer to impact parameters of  $5.9\text{fm} < b < 10.2\text{fm}$ , rapidities of  $0.3 < y/y_{\text{beam}} < 0.7$  and momenta of  $0.2\text{GeV}/c < p_t < 0.8\text{GeV}$ . The lines are fits with function 4.3 resulting in the values for  $v_1$  and  $v_2$  as given in the figure. Figure taken from [U<sup>+</sup>04]. . . . .* 63



- 5.5 Azimuthal distribution of  $\pi^+$ ,  $K^+$  and  $K^-$  mesons for semi-central Ni+Ni collisions at 1.93 AGeV. The data are corrected for the resolution of the reaction plane and refer to impact parameters of  $3.8\text{fm} < b < 6.5\text{fm}$ , rapidities of  $0.3 < y/y_{\text{beam}} < 0.7$  and momenta of  $0.2\text{GeV}/c < p_t < 0.8\text{GeV}$ . The lines are fits with function 4.3 resulting in the values for  $v_1$  and  $v_2$  as given in the figure. Figure taken from [U<sup>+</sup>04]. . . . . 63
- 5.6 Azimuthal angular emission patterns of  $K^+$  mesons measured in Au+Au at 1.5 AGeV collisions close to mid-rapidity in non-central events. Figures from left to right correspond to one of the transverse momentum sets: without  $p_t$  selection (left), with low  $p_t$  ( $0.2 < p_t < 0.5$  - middle) and high  $p_t$  ( $0.5 < p_t < 0.8$  - right). Lines represent fits according to formula 4.3. . . . . 64
- 5.7 Azimuthal angular emission patterns of  $K^-$  mesons measured in Au+Au at 1.5 AGeV collisions close to mid-rapidity in non-central events. Figures from left to right correspond to one of the transverse momentum sets: without  $p_t$  selection (left), with low  $p_t$  ( $0.2 < p_t < 0.5$  - middle) and high  $p_t$  ( $0.5 < p_t < 0.8$  - right). Lines represent fits according to formula 4.3. . . . . 64
- 5.8 Elliptic flow of  $K^+$  and  $K^-$  mesons as a function of transverse momenta measured in Au+Au at 1.5 AGeV collisions close to mid-rapidity. Data selected for  $b > 6.4\text{fm}$ . . . . . 65
- 5.9 Azimuthal angular distribution of  $K^+$  (left) mesons measured close to mid-rapidity in Au+Au at 1.5 AGeV collisions compared to various transport model calculations. . . . . 66
- 5.10 Elliptic flow of  $K^+$  mesons as a function of transverse momentum. The results of the calculations [Bra05, CTBR03, MBSB<sup>+</sup>04] and data from the measurement selected for non-central Au+Au collisions at 1.5 AGeV close to mid-rapidity. . . . . 66
- 5.11 Azimuthal angular distribution of  $K^-$  mesons measured close to mid-rapidity in Au+Au at 1.5 AGeV collisions compared to various transport model calculations. . . . . 67
- 5.12 Elliptic flow of  $K^-$  mesons as a function of transverse momentum. The results of the calculations [Bra05, CTBR03, MBSB<sup>+</sup>04] and data from the measurement selected for non-central Au+Au collisions at 1.5 AGeV close to mid-rapidity. . . . . 67
- 5.13 Production rates of  $K^+$  (upper panel) and  $K^-$  (lower) as functions of collision time according to different theoretical models. . . . . 68
- 5.14 Number of  $K^+$  (upper panel) and  $K^-$  (lower) as functions of collision time according to selected theoretical models. . . . . 68
- 5.15 Elliptic flow evolution of  $K^-$  mesons in different models. Additionally for calculations close to mid-rapidity the total elliptic flow has been decomposed into part associated with the strangeness-exchange production channel and all other. Calculations for semi-central Au+Au collisions at 1.5 AGeV [Bra05]. . . . . 69

A.1 *The acceptance and the in-flight decay corrections for Kaons as a function of the kaon momentum in the laboratory frame for the three measured magnetic field settings of the dipole magnet. . . . .* 74

A.2 *Trigger efficiency for the TOF setting as a function of the kaon momentum in the laboratory frame for the three measured magnetic field settings of the dipole magnet. . . . .* 75

A.3 *Total efficiency of the  $3\sigma$  cut for the two magnetic field settings . . . . .* 77



# List of Tables

3.1	<i>The centrality bins selection as well as the calculated average number of participants and the average number of collisions. . . . .</i>	28
3.2	<i>The correction parameters for reaction plane resolution and the systematic error estimates for <math>v_1</math> and <math>v_2</math>. . . . .</i>	35
4.1	<i>Detailed measurements: elliptic flow of <math>K^+</math> mesons at <math>36^\circ &lt; \theta_{lab} &lt; 52^\circ</math> (see fig. 4.28 and fig. 4.29). . . . .</i>	55
4.2	<i>Detailed measurements: elliptic flow of <math>K^-</math> mesons at <math>36^\circ &lt; \theta_{lab} &lt; 52^\circ</math> (see fig. 4.28 and fig. 4.29). . . . .</i>	57
4.3	<i>Previous measurements of elliptic flow of <math>K^+</math> mesons in Au+Au reactions at 1.5 AGeV [För03]. . . . .</i>	58



# Chapter 1

## Introduction

Relativistic heavy ion collisions give the unique opportunity to study hot and dense nuclear matter which is a strongly interacting many-body system, ultimately to be described by nonperturbative quantum chromodynamics (QCD). By varying the bombarding energy as well as projectile and target combinations it is possible to create systems of different baryon density and temperature. This allows the study of different phases of nuclear matter. At low densities, a phase transition from the nuclear liquid to a gas of nucleons is investigated, whereas at high densities, the phase transition to the quark gluon plasma is predicted to occur, where chiral symmetry is restored and quarks are deconfined. In the energy range of several GeV/u nuclear densities are created as in the interior of neutron stars. A collision of two gold nuclei with an incident beam energy of 2 AGeV<sup>1</sup> may create a fireball with nuclear densities reaching  $3 \cdot \rho_0$  (where  $\rho_0$  is the normal nuclear density). A schematic presentation of such reaction simulated in the UrQMD [B<sup>+</sup>98] transport model is shown in fig. 1.1.

The aim of the experiments performed with high energy heavy ions at Gesellschaft fuer Schwerionenforschung (GSI), Darmstadt is to investigate the properties of nuclear matter under such extreme conditions. The compressibility of nuclear matter, in-medium properties of hadrons, as well as the reaction dynamics, are being studied. The KaoS collaboration has been addressing these topics using its versatile Kaon Spectrometer and GSI's accelerator facility.

This work focuses on the properties of strange mesons inside the nuclear medium. The goal is to extract information on their production mechanism and interaction characteristics from their azimuthal emission pattern.

---

<sup>1</sup>Units used in this document are  $\hbar = c = 1$  or stated otherwise.

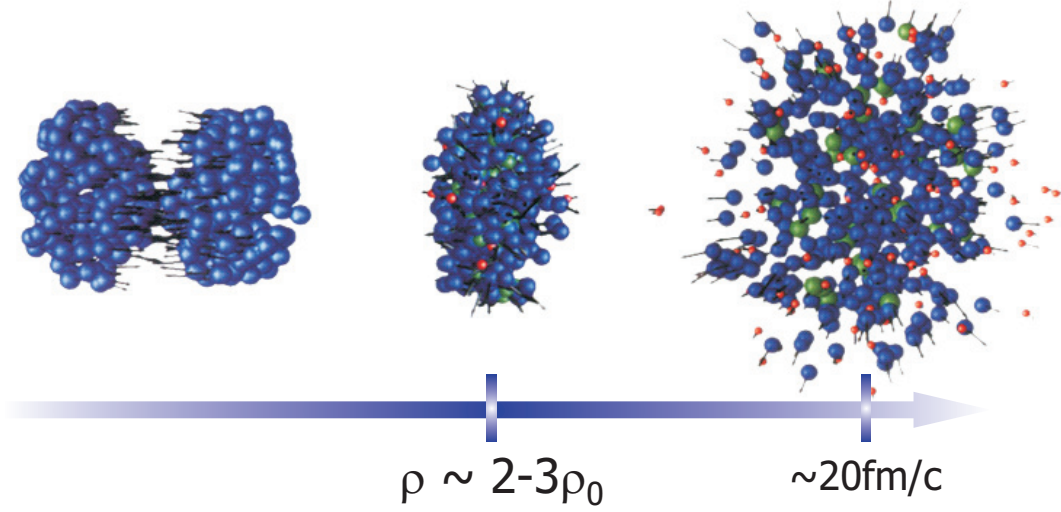


Figure 1.1: Two gold nuclei centrally colliding at a beam energy of 2.0A GeV presented at 3 different stages - left: just before the collision, middle - the dense phase of the overlapping nuclei, right - the reaction participants and products flying away from the collision zone.

## 1.1 Strange and antistrange meson production

The production of  $K$  meson in elementary nucleon-nucleon collisions has its threshold at a kinetic beam energy of 1.58 GeV for the channel



where the kaon ( $K^+$  or  $K^0$ ) contains the antistrange quark and the  $\Lambda$  hyperon the strange quark. On the other hand the production threshold for antikaons is significantly higher. Flavor conservation and minimum energy preference dictates in this case a production mechanism to be



with its threshold at 2.5 GeV. Here, the  $\bar{K}$  meson contains the s-quark.

Additional kaon and antikaon production channels become available in the A+A reactions. Heavy-ion collisions open the possibility for multi-step processes to take place. In this case nucleons collide with newly created particles like pions or  $\Delta$  resonances which act as an energy reservoir. An example of such multi-step process may begin with a reaction



The products of 1.3 may later collide, creating a  $K$  meson, according to the processes

$$\Delta N \rightarrow NKY \quad \text{or} \quad N\pi \rightarrow KY \quad (\text{after: } \Delta \rightarrow N + \pi),$$

where a hyperon  $Y$  may be a  $\Lambda$  or  $\Sigma$ . Also, the collision of a  $\Delta$  resonance with a nucleon may occur at sufficiently high energy to produce a kaon-antikaon pair:

$$N\Delta \rightarrow K\bar{K}NN. \quad (1.4)$$

Another important reaction channel contributing to the  $\bar{K}$  production is the *strangeness exchange* process:

$$Y\pi \rightarrow \bar{K}N. \quad (1.5)$$

The inverse process of 1.5 may result in the absorption of  $\bar{K}$  meson as with cross-section of about  $40mb$  [Ko84, Oes01]. This affects the propagation features of antikaons and reduces their probability to leave the reaction zone.  $K$  mesons however are not absorbed as they contain an antistrange quark. Their elastic interaction cross-section with nucleons is small ( $\sigma_{K+N} = 10mb$ ) and the probability of an encounter with a  $\Lambda$  or  $\Sigma$  and annihilation is negligible hence they may emerge from the dense phase of a collision almost undisturbed. Therefore,  $K$  mesons are well suited to probe the hot nuclear matter and their spectrum is expected to provide information on the dense phase. On the other hand, the number of  $\bar{K}$  may be reduced by absorption after they are produced by the processes 1.4 and 1.5.

The production of a particle in a heavy-ion collision, in which the incident beam energy per nucleon is smaller than the threshold for its production in elementary collisions, is referred to as *subthreshold production*. Let us notice that the subthreshold production is especially sensitive to the in-medium effects and to the compressibility of nuclear matter, as the number of multi-step processes is baryon density dependent.

Indeed, the subthreshold production of kaons has proved to be a sensitive observable for the compressibility of the nuclear matter. Systematic studies of  $K^+/K^-$  ratios performed by KaoS collaboration with different collision systems (very light - C+C, and very heavy - Au+Au) of the kaon production resulted in an important observation of a preference for a soft nuclear *Equation-Of-State* (EOS) [S<sup>+</sup>02]. The stiffness of the nuclear EOS plays an important role within astrophysics for the description of the supernova explosions and stability of the neutron stars [BB82, LP00].

## 1.2 In-medium effects

Theoretical considerations predict that kaon-nucleon potentials [GEBT94, WKW96, KN86] play an important role for  $K^+$  and  $K^-$  properties in the dense nuclear matter. The K



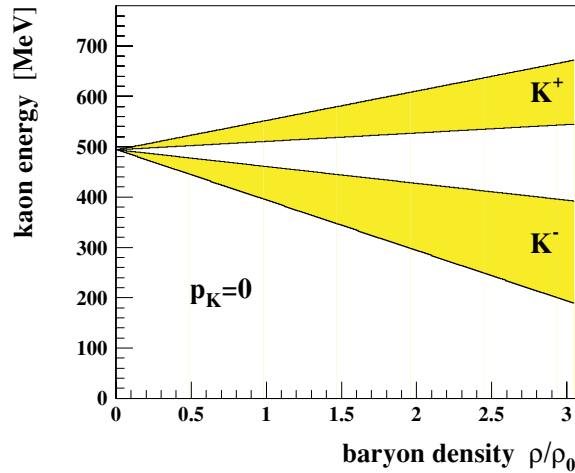


Figure 1.2: Predictions on the kaon and antikaon energy modifications: the gray shaded bands represent the range of results from various model calculations (see [JSBB97] and references therein).

mesons are affected by the influence of both a scalar and a vector meson-baryon potentials. The scalar potential acts attractively on both kaon species, while the vector potential repels  $K^+$  and attracts  $K^-$ . For  $K^+$ , these two contributions mainly cancel each other leading to a small repulsive  $K^+N$  interaction, whereas the superposition of both attractive interactions results in a strong attractive potential for  $K^-$  [JSBB97]. Theoretical predictions discuss that the effective particle mass  $m^*$  might change in the dense nuclear matter from the free value. The change of the particles' effective mass can be ascribed to a potential  $V$  so the in-medium energy of a particle, i.e. the dispersion relation, can be expressed as

$$E = \sqrt{m^{*2} + p^2} = V(\rho) + \sqrt{m_o^2 + p^2}. \quad (1.6)$$

Within such a picture, gradients of the potential  $V(\rho)$  give rise to forces  $F = -\nabla V$  that influences the path of the particles as they propagate through the dense medium. Although this is valid for all particles, it is especially interesting for kaons. Figure 1.2 shows the range of various theoretical predictions for the kaon and antikaon energy modifications as a function of the baryon density. It is expected that apart from the in-medium mass and production characteristic also the propagation of kaons and antikaons is modified. Therefore a sensitive observable for in-medium properties of strange mesons should be their azimuthal angular distribution [LKL95]. The investigations related with the in-medium mass modifications of antikaons are relevant for modeling of the properties and dynamics of stellar objects, especially neutron stars as pointed in [LLB97].

### 1.3 Collective flow phenomena and azimuthal emission pattern

Bulk properties of nuclear matter under extreme conditions should be visible most clearly in collective features of the data. Collective flow is the prototype of such a common feature. It manifests itself in particle correlations, both in angle and in magnitude of velocity. The collective flow in transverse direction in heavy-ion has been predicted by Scheid et al [SHG] based on a hydrodynamical picture. For the first time collective flow was observed in azimuthal distributions by GSI/Lawrence Berkeley National Laboratory (LBNL) Plastic Ball[G<sup>+</sup>84] and Streamer Chamber[R<sup>+</sup>84] collaborations at the Bevelac accelerator.

The main focus of this work is set on the observation of the collective phenomena of *directed flow* (often called *sideflow*) and *elliptic flow* of strange mesons. The sideflow is characterized by an enhanced emission into the azimuthal direction defined by the impact parameter vector. Whereas elliptic flow describes an emission pattern in which particles are found to be preferentially emitted with respect to the reaction plane and with back-to-back symmetry.

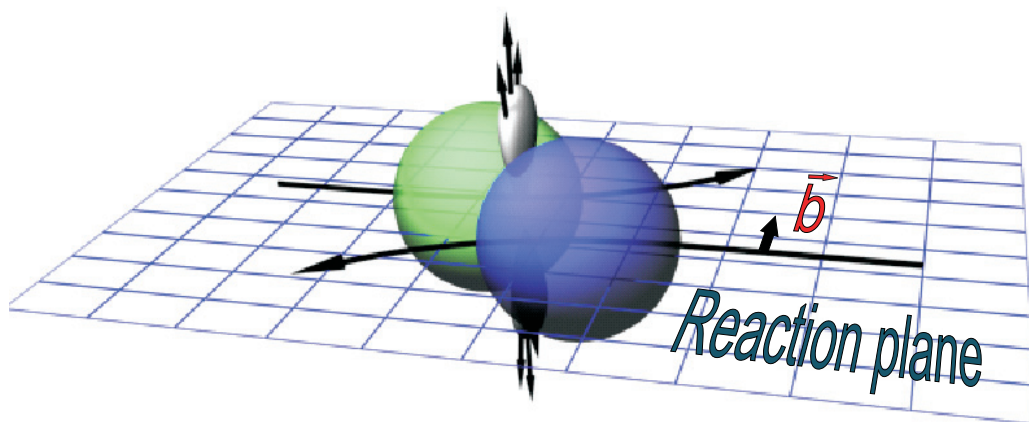


Figure 1.3: Reaction plane defined by the impact parameter  $b$  and the beam axis.

In a heavy-ion collision at a finite impact parameter only a part of the nucleons undergo a collision. These nucleons are called participants. The spectators, i.e. the nucleons which do not collide, continue their flight almost undisturbed in the direction of the beam axis and with velocities close to the beam velocity as they experience only the (distorted) mean field of their parent nuclei. The little deflection of the spectators plays a crucial role in diagnosing the reaction geometry. The detection of the projectile fragments at forward polar angles gives the possibility to reconstruct the orientation of the impact parameter vector. In order to establish the azimuthal angular particle emission it is necessary to ob-

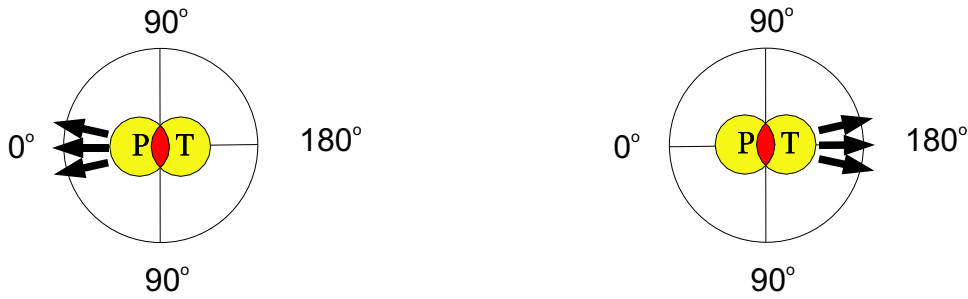


Figure 1.4: Schematic presentations of heavy-ion collisions with beam axis pointing into the picture. Letters *P* and *T* stand for projectile and target accordingly. Arrows present the preferred directions of sideflow. Enhanced emission of particles oriented at  $0^\circ$  and  $\pm 180^\circ$  degrees with respect to the reaction plane denotes a correlation towards either projectile or target nucleus. Overlapping region of the two nuclei is the high density phase of the collision.

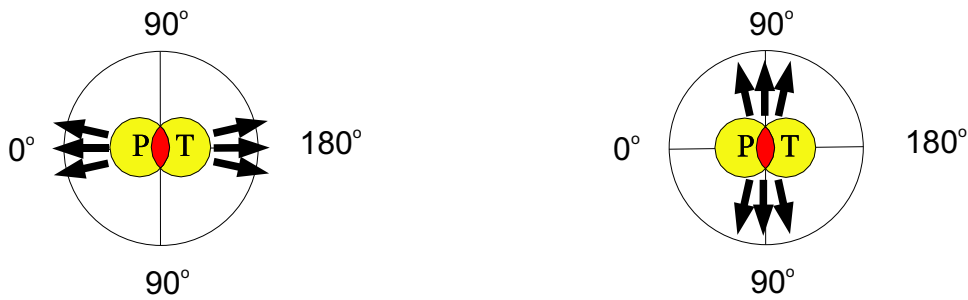


Figure 1.5: Two collision figures similar as in fig. 1.4, however here the arrows refer to the elliptic flow component. A back-to-back symmetric emission at  $0^\circ$  and  $\pm 180^\circ$  degrees is an in-plane flow and an enhanced emission of particles towards  $\pm 90^\circ$  degrees is an out-of-plane flow (often called *squeeze-out*).

tain the information about the reaction plane. The reaction plane is defined by the beam axis and the impact parameter (see fig.1.3). One of the general procedures to extract the reaction plane information is the Fourier coefficient method [Oll95]. One of its variations described in chapter 3.5 and has been applied in the presented analysis. The underlying fact is that it is possible to construct a vector  $\vec{Q}$  composed out of geometrical distribution of the spectators. The vector  $\vec{Q}$  is supposed to be correlated with the orientation of the true reaction plane angle.

Figures 1.4 and 1.5 show schematic representations of the directed and elliptic flow components in heavy-ion collisions. The arrows define directions for sideflow (1.4) and elliptic flow (1.5) with respect to the reaction plane defined by the  $0^\circ - 180^\circ$  horizontal line and the beam axis pointing into the picture.

The Kaos collaboration has been studying kaon and antikaon production in heavy-ion collisions in several reaction systems and at different incident beam energies. The reported, out-of-plane emission of  $K^+$  in Au+Au collisions at 1.0 A GeV [S<sup>+</sup>98] has been in-

### 1.3. COLLECTIVE FLOW PHENOMENA AND AZIMUTHAL EMISSION PATTERN 7

terpreted as a consequence of the repulsive  $K^+N$  potential [LKB96, LKB98, WFFGB99] (see fig. 1.6). Theoretical considerations claim that the repulsive potential for  $K^+$  mesons enhances their emission in the direction where the gradient of the pressure build up in a collision is lower (e.g. out-of-plane). On the other hand the attractive potential for  $K^-$  mesons should counter act their emission in the perpendicular direction to the reaction plane balancing large re-scattering and absorption probability in the spectator matter. The transport models has shown almost no preference in the direction of the emission of  $K^-$  mesons when including the mean field influence [WFFGB99] (see fig. 1.7).

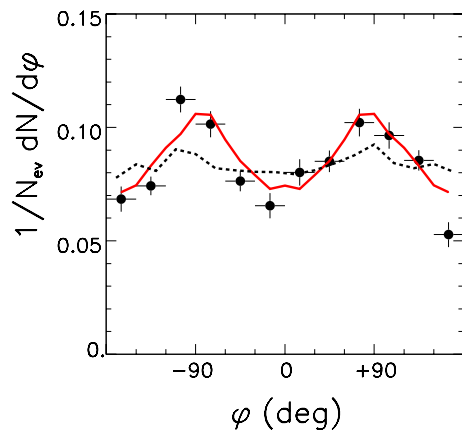


Figure 1.6:  $K^+$  azimuthal angular distribution measured in semi-central ( $b = 5-10\text{fm}$ ) Au+Au collisions at 1 AGeV around mid-rapidity ( $0.1 < y < 0.6$ ) for  $K^+$  transverse momenta of  $0.2\text{GeV}/c < p_t < 0.8\text{GeV}/c$ . The lines represent results of RBUU calculations for an impact parameter of  $b=7\text{fm}$  [LKB96] without (dashed line) and with an in-medium KN potential (solid line). Both calculations take into account kaon-nucleon re-scattering [S<sup>+</sup>98].

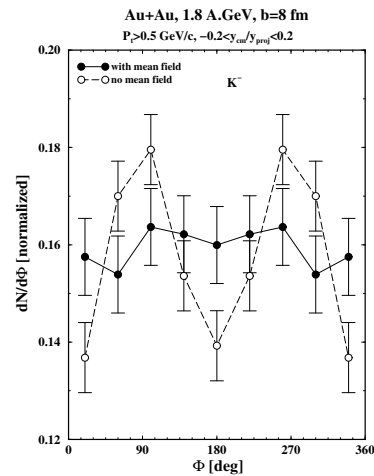


Figure 1.7: Theoretical calculations of the azimuthal angular emission pattern of  $K^-$  mesons at 1.8 AGeV with their preselected transverse momentum  $p_t > 0.5\text{GeV}$  at a moderate centrality  $b = 8\text{fm}$ . The two curves present the expected influence of the mean field potential on the azimuthal angular distributions of antikaons [WFFGB99].

Similar, out-of-plane, emission patterns of  $K^+$  mesons have been observed in Au+Au at 1.5 AGeV [U<sup>+</sup>04, För03]. Additionally, the observed out-of-plane emission pattern of  $\pi^+$  which is in agreement with previous observations [B<sup>+</sup>93, B<sup>+</sup>97] has been attributed to re-scattering and absorption, whereas a similar explanation for kaons cannot hold as

the mean free path of  $K^+$  mesons is significantly larger than that of the pions, thus only a moderate out-of-plane enhancement would be expected.

Ultimately, the missing measurement was the azimuthal emission pattern of the  $K^-$  mesons. Antikaon flow at subthreshold energies is predicted to exhibit a different behavior from  $K^+$  [LK96, BCM97]. In order to obtain sufficient  $K^-$  statistics, a dedicated experiment Au+Au at 1.5AGeV has been scheduled and performed in June/July 2001 at GSI Darmstadt. This work describes the experimental setup (the Kaon Spectrometer) used for the measurement, the analysis methods used to obtain the results presented in following chapters, as well as the conclusions on the observation.

## Chapter 2

# Experimental Setup

The Kaon Spectrometer, KaoS[S<sup>+</sup>93] at GSI is composed of a quadrupole and a dipole magnet having large acceptance in momentum ( $p_{max}/p_{min} \approx 2$ ) and solid angle ( $\Omega \leq 35$  msr). The maximum dipole magnetic field is  $B = 1.95$  T corresponding to a momentum of  $p_{max} = 1.6$  GeV/c for singly charged particles. The setup consists of:

- a magnet system - the magnetic quadrupole field provides vertical focusing into the gap of the dipole and the magnetic dipole field
- the Time-Of-Flight detectors:
  - the D detector marking the start for the TOF measurement,
  - the F detector providing the TOF stop signal,
- the target detector - T - called Large Angle Hodoscope, located close to the target, detecting particles at polar angles from 12 to 48 degrees, allows reaction centrality estimation and additionally is used for a second TOF measurement,
- the Cherenkov radiation detector - C detector - used for separation of the high momenta kaons from protons,
- three Multi-Wire Proportional Chambers (named L, M, N, respectively) used for particle trajectory reconstruction,
- the Small Angle Hodoscope - a wall of scintillators used for the reconstruction of the reaction plane orientation, covering 1 to 10deg of the polar angle,
- the beam monitoring detectors.

Let us choose a Cartesian coordinate system with its origin at the target such that the beam direction defines the Z-axis and the X-axis parallel to the ground pointing to the left

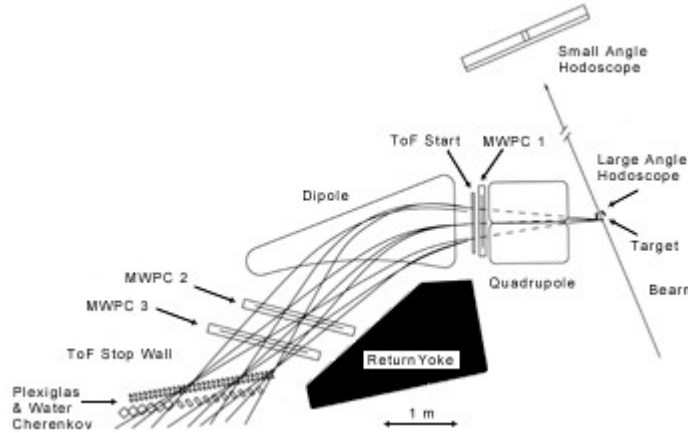


Figure 2.1: *Sketch of the Kaon Spectrometer and its detector system*

hand side when facing the small angle hodoscope at the target, and the Y-axis pointing upward. A cross-section in the ZX plane of the kaon spectrometer is shown in fig.2.1. The support structure allows rotation around the target area, giving access to polar angles from 30 to 130 degrees. This flexibility combined with different magnetic field settings extensively enhances the geometrical acceptance of the detector setup.

## 2.1 Magnet system

The particles are focused vertically by the quadrupole magnet (into the 20cm gap of the dipole) and horizontally by the tilted exit boundary of the dipole. The quadrupole aperture is 30 cm and its maximum pole tip field is  $B = 1\text{T}$ . The maximum dipole magnetic field of  $B = 1.95\text{T}$  is generated by a coil current of  $I = 2500\text{A}$ . At this current setting the power consumption of both magnets is 550kW. The central ray deflection angle of the spectrometer is 45 degree, and the dispersion along the focal plane is 2.2cm per percent momentum. The setup has a total weight of 120 tons.

## 2.2 Trigger

The experimental challenge of strange meson production in the SIS energy range is the low production cross-section of kaons as compared to the abundant pions and protons. Taking into account the limitations in the processing rates of the data acquisition system it was necessary to provide a dedicated hardware trigger in order to select and record only interesting events (e.g. with a kaon candidate). Within the KaoS setup several trigger settings are possible:

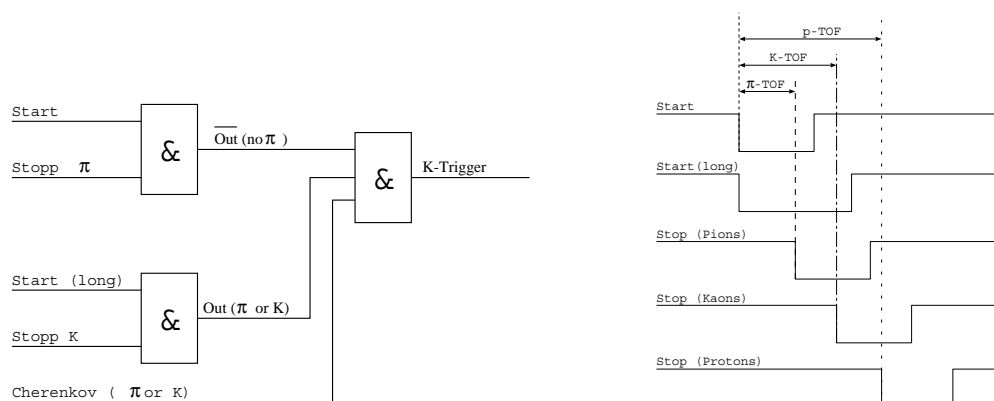


Figure 2.2: The layout sketch of the logic (left figure) and timing (right figure) of the trigger.

- the minimum bias trigger,
- the spectrometer trigger,
- the kaon-TOF trigger.

### Minimum bias trigger

The reaction trigger is generated when at least two modules of the target detector register particles within a  $200ns$  time gate. This ensures that the projectile has interacted with a target nuclei. These minimum bias events serve for an accurate input to the reaction plane normalization procedure (see section 3.6) and the collisions centrality estimation (see section 3.4).

### Spectrometer trigger

The spectrometer trigger is established with a coincidence of a start signal from D-detector and a stop signal from F-detector. The coincidence of signals from the D- and F-detectors is a good indication that a particle has traveled through the spectrometer.

### Kaon trigger

The logic of the kaon-TOF trigger is shown in the left part of fig.2.2. To suppress the bulk of pions and select kaons, a sequence of coincidence gates was set up. The start signal from the D-detector is split. One of the start signals was extended providing an additional time gate. The width of the gate was optimized for the expected time of flight of kaons and to eliminate the protons. As indicated in the timing diagram in the right part of



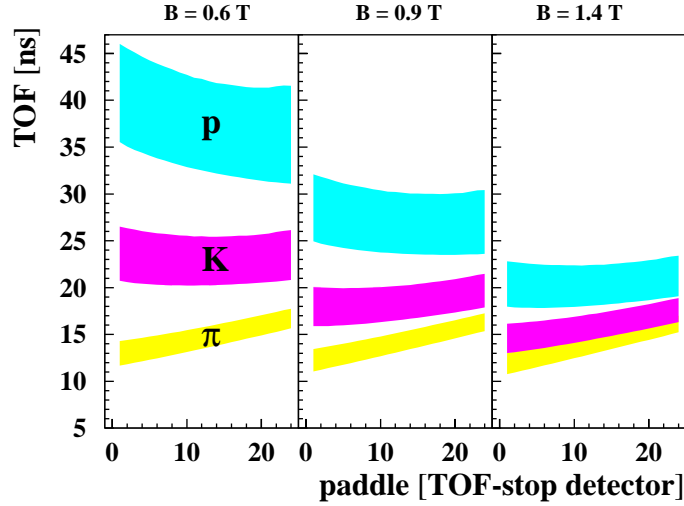


Figure 2.3: *Time of flight as a function of the F detector paddle number for different particle species and three different magnetic field setting (0.6T - left, 0.9T - middle, 1.4T - right).*

figure 2.2, the stop signal of protons is outside the time gates opened by both start signals, however the pions may still deliver a proper trigger. To exclude this possibility, an anti-coincidence with short time of flight signal of pions was set. Additional suppression of protons is provided by a coincidence with the signals from the Cherenkov detectors. This trigger latch is used for measurements with high magnetic field where the time difference between kaons and protons is too small to be discriminated by the TOF only (see fig. 2.3)

Figure 2.3 shows the time of flight for pion, kaons and protons as a function of the F-detector paddle (TOF-stop detector). The three sections of the figure represent three different magnetic field settings. Clearly, to ensure the correct functionality of the trigger, the time gates for the signals have to be modified whenever the magnetic field setting is changed. This is done with use of the slow control system.

## 2.3 Time-Of-Flight measurement

The measurements of the TOF of a particle is one of the key observables used for particle identification. TOF start signal is provided by the D detector located between the quadrupole and the dipole magnets. The D detector consists of 16 vertically aligned plastic scintillators (paddles) of dimensions 22 cm (height) x 3 cm (width) x 0.4 cm (thickness). Each scintillator is read out via a light guide by two 3/4" HAMAMATSU R3478 photo-tubes mounted at both ends. The horizontal segmentation allows a rough determination of the emission angle (10 mrad). For additional information see [S<sup>+</sup>90, Wag92].

The F detector (TOF stop) located approximately in the focal plane of the spectrometer consists of a row of 30 plastic scintillators (38cm x 3.7cm x 2cm) tilted by 9 degrees in the direction of incoming particles, allowing them almost perpendicular flight path through the paddles. The scintillators are read out on both ends by HAMAMATSU R1828 phototubes. The position of the trajectory in the focal plane is known with accuracy determined by the dimensions of the scintillators resulting in the momentum resolution of about 4%. With this setup, a time resolution of 100ps (FWHM) for protons ( $\beta \approx 0.75$ ) has been reached, and of 140ps for pions. Figure 2.3 shows the time of flight as a function of the F detector paddle number for different particle species and different magnetic field settings.

Another method of the TOF measurement makes use of the signals from the T-detector. The timing signals from the modules of the target detector are used as a reference for the additional TOF-start signal. The TOF-stop for this measurement is delivered by one of the paddles of the F detector.

## 2.4 Tracking detectors

In order to reconstruct the trajectories of the particles three large area multi-wire proportional chambers (MWPC) were used. The first MWPC (L) has an active area of 40x70 cm<sup>2</sup> and is located between the quadrupole and the dipole. The second and third (M and N) MWPC positioned between dipole magnet and the F detector have sensitive areas of 40x120cm<sup>2</sup>. The position resolution of the chambers is 0.5 mm (FWHM). More information on the construction and performance of the detectors can be found in [Heh90, Sar91, Gei93]. The coordinates of the hit positions from the chambers is used to reconstruct the particle trajectories. The momentum of a particle can be determined by extrapolating the measured trajectory to the focal plane (see section 3.3.1).

## 2.5 Beam normalization detectors

In order to reconstruct the production cross-sections of particles it is necessary to know the flux of incident beam particles (see appendix A). The intensity is determined with two plastic scintillator telescopes (*Moni<sub>left</sub>* and *Moni<sub>right</sub>*) which consist of 3 detectors (40x40 mm<sup>2</sup>) each. The telescope arms point to the target at  $\Theta_{lab} = 110^\circ$  in the horizontal plane. The distance between the target and the first detector and between the subsequent detectors is 15 cm. The count rate of the threefold coincidences of the detectors of each telescope arm is recorded with a scaler. The calibration factor (beam intensity/telescope count rate) is determined by reducing the beam intensity to about  $10^5 ions/s$  and counting the beam directly with a movable plastic scintillator (20x20x3mm<sup>3</sup>). The telescope count rate increases linearly with the beam current up to the highest intensities used in the experiment ( $1 \times 10^8/s$ ). A detailed description of these detectors can be found in [Bec93].

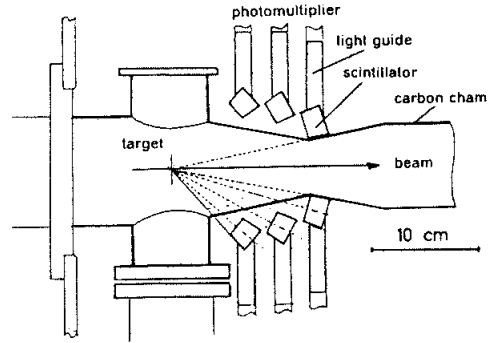


Figure 2.4: *Target detector - cross section.*

## 2.6 Target detector

The number of fired modules of the target detector is used to determine the centrality of the events (see section 3.4). Fig. 2.4 shows a cross-section of the T-detector. Its 84 modules are located near the target, arranged in 3 rings at 3 different polar angles (covering the range of  $12^\circ \leq \theta_{lab} \leq 48^\circ$ ). Each ring is located at a different distance from the target (8cm, 10.5cm, 13cm). The rings do not cover the full azimuth having a gap allowing the free passage of the particles towards the spectrometer. Each of the modules delivers the time and the energy information. The multiplicity of the charged particles emitted from a heavy-ion collision at high polar angles varies monotonously with the impact parameter. Therefore the multiplicity measured by the T-detector in combination with the geometrical model ([Gla]) of the heavy-ion collision allows for the event centrality reconstruction. In addition, with the help of the cluster method analysis described in [Stu01], it is possible to generate a separate start signal for the TOF measurement within the spectrometer (see section 2.3).

## 2.7 Small Angle Hodoscope

The small angle hodoscope (see fig.2.5) gives the possibility to measure the time of flight, energy loss and the emission angle of the particles at polar angles from 1-10 degrees.

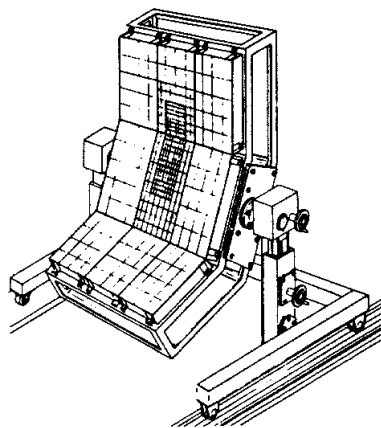


Figure 2.5: *Small Angle Hodoscope.*

Therefore, it provides the possibility for the reaction plane reconstruction (see section 3.5). The hodoscope consists of 380 scintillator modules located 7 m downstream the from the target. The modules are divided into 3 groups of different size. The inner part around the beam axis consists of modules of 4x4 cm dimension, while the middle modules are 8x8 cm and the outer - 16x16 cm.

## 2.8 Data acquisition and the slow control

The data acquisition system is based on the GSI's standard MBS (*Multi Branch System* [B<sup>+</sup>00]). The timing and the energy loss signals from the scintillators (after splitting, amplifying and deriving timing signals) are sent to the appropriate analog-to-digital converters. The data from the converters located in both FASTBUS crates were transferred via the VSB bus to the corresponding E7-VME type CPUs. The signals from the multi-wire chambers were digitized via 8-Bit-Flash-ADCs, read out in groups of 16 channels by a Transputer(T225, 16bit), synchronized by a Transputer T801 and delivered to one of the FASTBUS crates through an improved version of *Event Builder Interface*[Ba193], again read out by an E7 via VSB. Information from the beam intensity monitors as well as the timing information was delivered from scalers and DACs read out in an CAMAC crate via VSB by an additional E7 placed in the VME Crate as well. One of the E7 CPUs in the main VME Crate has been dedicated for the sub-event information collection and

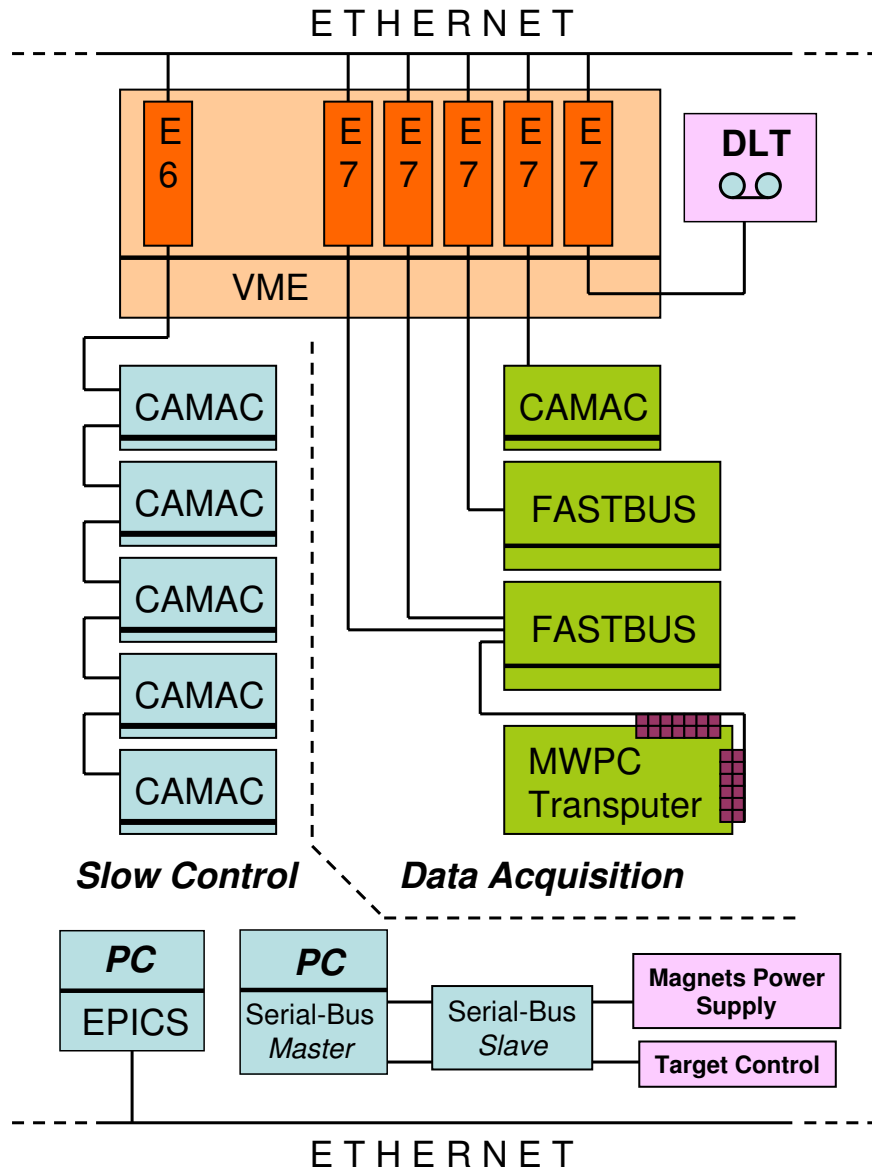


Figure 2.6: Schematic sketch of the data acquisition system and the slow control [Koc05, Pto99].

connected via a SCSI bus to a DLT (*Digital Linear Tape*) drive for data recording on magnetic tape cartridges.

The slow control of the experiment consists of five CAMAC crates linked via the VSB bus to an E6-VME type CPU providing the Ethernet access. In addition, the E6 CPU has been connected to a standard PC running the slow control software (EPICS [Lab05]) providing the interface managing the threshold and walk adjusting parameters

of the constant fraction modules and the high voltage controller of the scintillators' and Cherenkov detectors' photo-multipliers. Additional CPU equipped with a master-slave type Mill-Bus (serial RS232) interface and a dedicated software has been provided for the target positioning, and the power supply control for the magnets [Pfo99]. The data acquisition system and the slow control of the experiment are presented in the schematic sketch in fig.2.6.



# Chapter 3

## Data analysis procedure

### 3.1 TOF Calibration

The TOF calibration has been performed with a measurement of negatively charged pions. In order to minimize the random coincidences in the TOF-start (D) and TOF-stop (F) detectors the beam intensity has been reduced and only events with the hit multiplicity 1 have been selected. The GEANT [Gro93] simulation package in conjunction with a measured magnetic field map [Uhl04], has been used to calculate the times of flight of all pions in a chosen momentum range from the D and to the F detectors paddles. The comparison of the simulated values with the experimental data determines additive correction parameters for each of the detector modules.

Additionally, due to the short distance from the target to the T-detector modules, charged particles (mostly protons) participating in the reaction and detected in the target detector are used for defining *the reaction time* ( $t = 0$ ), thus, enabling a second flight measurement. Also for this measurement, a set of additive correction parameters is calculated with the help of Monte-Carlo simulation.

### 3.2 Small angle hodoscope calibration

The time of flight is a crucial information used for reaction plane determination. The procedure requires to select spectators of the collision from the set of all particles registered in the detector in a event. The selection is made with a TOF window tailored for the particles traveling close to the beam velocity.

Although the energy loss information has neither been used in the reaction plane determination, nor in any other analysis presented in this work it has provided a fine check of the detectors performance.



### 3.2.1 The time calibration

The time calibration procedure is to fix the time of flight value of projectile-like particles registered in the hodoscope such that it is similar to TOF of the beam particles. Assuming the hodoscope distance to the target  $d = 6.84m$  and the beam particles velocity  $\beta = 0.923$ , the flight time should be 24.7 ns.

The first step in the time calibration of the small angle hodoscope is to eliminate differences in signals from the detector modules caused by the setup of the hardware (e.g. different cable lengths). For this purpose, the hits with the highest energy deposition have been selected. This choice ensures selection of the heaviest projectile-like fragments which travel with the velocities close to velocities of the particles of the beam. Thus, the time of flight of a particle detected in a chosen module is approximately the time difference between the signals from the target detector and the timing signal from that module.

A so called "time-walk" correction is necessary for the *Leading Edge Discriminators* (LED) which were used in the readout of the modules of the hodoscope. It is known that the output signal of the LEDs depends on the amplitude of the input signal [Bel66]. The time-walk effect is defined as the time difference  $\delta t$  between two simultaneous signals, which have different amplitudes, detected by a given type of LED. In order to estimate the correction factor for each of the hodoscopes module a time difference for each of the TDC channels  $\delta t$  as a function of the QDC signal ( $Q$ ) has been plotted and parameterized in the form:

$$\delta t = C_1 \cdot \frac{1}{\sqrt{Q}} + C_2 \sqrt{Q} + C_3 \cdot \frac{1}{Q} + C_4 \cdot Q + C_5, \quad (3.1)$$

where the  $C_1, \dots, C_5$  are numerical coefficients.

### 3.2.2 The energy calibration

The procedure estimating the charge of the particles detected in the hodoscope is the consequence of the particles' energy loss in the scintillator described by the Bethe-Bloch formula [E<sup>+</sup>04]:

$$-\frac{dE}{dx} = 4\pi N_A r_e^2 m_e \rho \frac{Z_t}{A_t} \frac{Z_p^2}{\beta^2} \left[ \frac{1}{2} \ln \left( \frac{2m_e \beta^2 \gamma^2 T_{max}}{I_2} \right) - \beta^2 \right] \quad (3.2)$$

- $N_A$  - Avogadro constant
- $A_t$  - mass number of the target material
- $r_e$  - classical radius of an electron
- $Z_p$  - charge of the particle
- $m_e$  - mass of an electron
- $\beta$  - velocity of the particle
- $\rho$  - density of the target material
- $T_{max}$  - maximum energy transfer
- $Z_t$  - charge number of the target material
- $I$  - mean ionization energy of the target material.

As all projectile-like particles have velocities of the similar values, the dominant factor in the energy loss information is the charge  $Z_p$ . Therefore, in the energy spectrum for each of the detectors, several maxima marking the individual particle or fragment species with different  $Z_p$  can be seen. However, the peak positions do not strictly follow the  $Z_p^2$  relation and a correction is necessary. In order to correct for this effect, the maxima of the 10 first well visible charged fragments for each of the detectors have been marked and the correction parameterized by the function:

$$-\frac{dE}{dx} = \frac{a_1}{Z_p} + a_2 \cdot Z_p + a_3, \quad (3.3)$$

where  $a_i$  are free parameters, has been fitted.

Figure 3.1 shows the energy loss as a function of the velocity  $\beta$  for all of the hodoscope elements after the calibration procedure.

### 3.3 Tracking and particle identification

The Lorentz force acting on a moving charged particle is defined as

$$\frac{d\vec{p}}{dt} = q\vec{\beta} \times \vec{B}. \quad (3.4)$$

- $\vec{p}$  - particle momentum
- $t$  - time
- $q$  - particle charge
- $\vec{\beta}$  - particle velocity
- $\vec{B}$  - magnetic field vector

A trajectory can be parameterized by specifying a position vector  $\vec{r} = (r_x, r_y, r_z)$  and a momentum vector  $\vec{p} = (p_x, p_y, p_z)$ . We assume the z-axis to be the optical axis of the spectrometer, x-axis as the horizontal and y-axis as a vertical one.

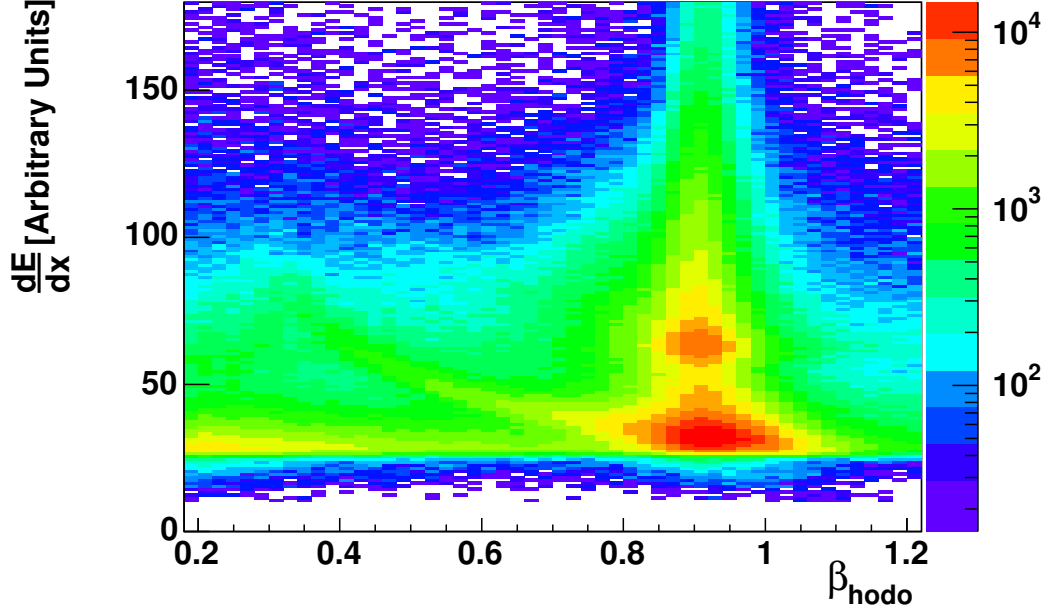


Figure 3.1: Energy deposition  $\frac{dE}{dx}$  for hits in the hodoscope as a function of the particles velocities  $\beta$ .

### 3.3.1 Trajectory reconstruction

The hit positions of the particles in the multi-wire chambers have been obtained separately for x- and y-cathode. Exact coordinates have been calculated from the charge distributions detected by the wires. A detailed description of the hit reconstruction procedure is given in [Sar91]. The achieved position resolution is of  $500\mu m$  (FWHM).

The particle trajectories are reconstructed by measuring the particle position with the multi-wire chambers and the TOF detectors. The procedure is based on the correlation functions of the hit coordinates. A detailed description of the method obtaining these functions can be found in [Uhl04, Wag96, Stu01]. The algorithm employs a Monte-Carlo simulation within the GEANT [Gro93] package including the geometry of the experiment and the 3 dimensional magnetic field map [Uhl04] to generate a set of possible particle trajectories. In order to extract the hit information in a chosen detector from the information obtained with the other detectors, the simulated tracks are fitted with a up to the 4<sup>th</sup> order polynomials. Therefore, for example, the correlation function  $\widehat{L}^x$  for the x-component of a hit position in the chamber L with the hit positions in the N and M chambers is described by:

$$\widehat{L}^x = \sum_{i=0}^4 \sum_{j=0}^4 c_{ij} M_i^x N_j^x. \quad (3.5)$$

Similar functions are obtained for the y-coordinates of three MPWCs, for D and F detectors, and also for the interaction vertex.

With help of the described method the conditions for the track candidates are defined, and with additional selection criteria defined in section 3.3.3 it is possible to eliminate most of the hit combinations which do not belong to the real particles or are generated by particles coming not from the interaction zone. Such false combinations and disturbing particles are often referred as *the background tracks* (or *the background particles*).

### 3.3.2 Particle mass determination

In order to assign a particle mass to a reconstructed track, another Monte-Carlo simulation with the GEANT [Gro93] package has been performed. For all the combinations of possible hits in the D and F detector paddles a flight path length  $\delta s$  and a corresponding  $p/Z$  (particle momentum per charge) factor have been calculated. Appropriate momentum spread resulting from the paddle sizes has been accounted for. Combining these quantities with the measured time of flight  $\delta t$ , the mass and the charge for a given particle track can be calculated from the relation:

$$\left(\frac{m}{Z}\right)^2 = \left(\frac{p}{Z}\right)^2 \left[ \left(\frac{\delta t}{\delta s}\right)^2 - 1 \right]. \quad (3.6)$$

The particle species were identified as tracks in the window of  $3\sigma$  around the prominent peak near their nominal mass value in the mass spectrum. Figure 3.2 presents mass spectra of particles for a chosen spectrometer angle and magnetic field settings.

### 3.3.3 Definition of the tracking cuts

Already a rough comparison of real hits in the detectors with simulated hit positions as well as the comparison of TOF information from both TOF measurements allow to define *the best track candidates* and reject most of the fake tracks, however in order to significantly reduce the contamination of the background particles in the kaon and antikaon samples, additional cuts have been applied.

The cut parameters for each positive magnetic field setting were obtained separately using files acquired with the maximum angle ( $\theta_{spec} = 72^\circ$ ) set in the experiment.

The cuts have been defined as follows:

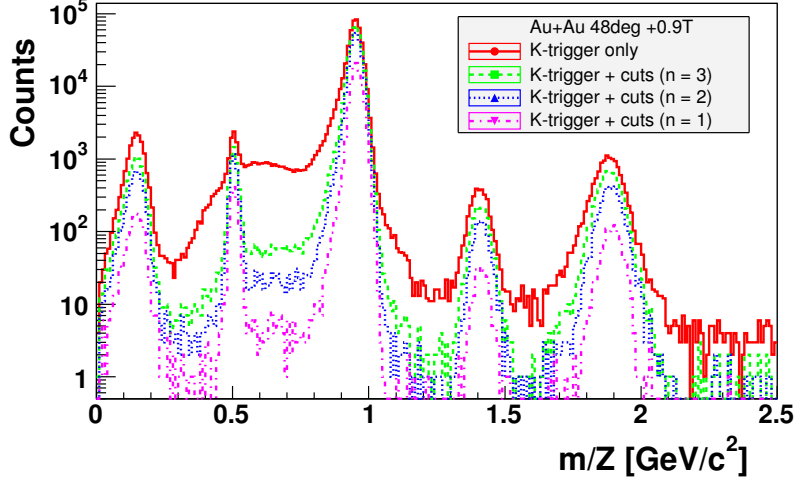


Figure 3.2: Mass per charge spectra showing the measured data with the Kaon trigger and also after applying the cuts defined with formulas 3.7, 3.8 and 3.10 for 3 different selection windows ( $n = 1, 2, 3$ ). Data sample acquired with the spectrometer angle  $\Theta_{spec} = 48^\circ$  and magnetic field settings  $0.9T$

- geometrical cut in differences, in x-axis of L-chamber and in y-axis of N-chamber, between the hits in the detectors (data) and the hit positions calculated using the correlation functions (GEANT) defined in section 3.3.1:

$$|L_{Geant}^X - L_{data}^X| \leq n \cdot \sigma^{LX} \quad (3.7)$$

and

$$|N_{Geant}^Y - N_{data}^Y| \leq n \cdot \sigma^{NY}. \quad (3.8)$$

- TOF cut in the normalized beta variable calculated from the two TOF measurements:

$$\left| \frac{\frac{1}{\beta_F} - \frac{1}{\beta_{TF}}}{\frac{1}{\beta_F}} \right| \leq n \cdot \sigma^\beta \quad (3.9)$$

Fig. 3.3 presents the distributions of the cut variables defined by the LHS of formulas 3.7, 3.8 and 3.10. The  $\sigma$  values have been obtained by fitting a Gaussian distribution defined as

$$f(x) = C \cdot e^{-\frac{1}{2} \left( \frac{x-\mu}{\sigma} \right)^2}, \quad (3.10)$$

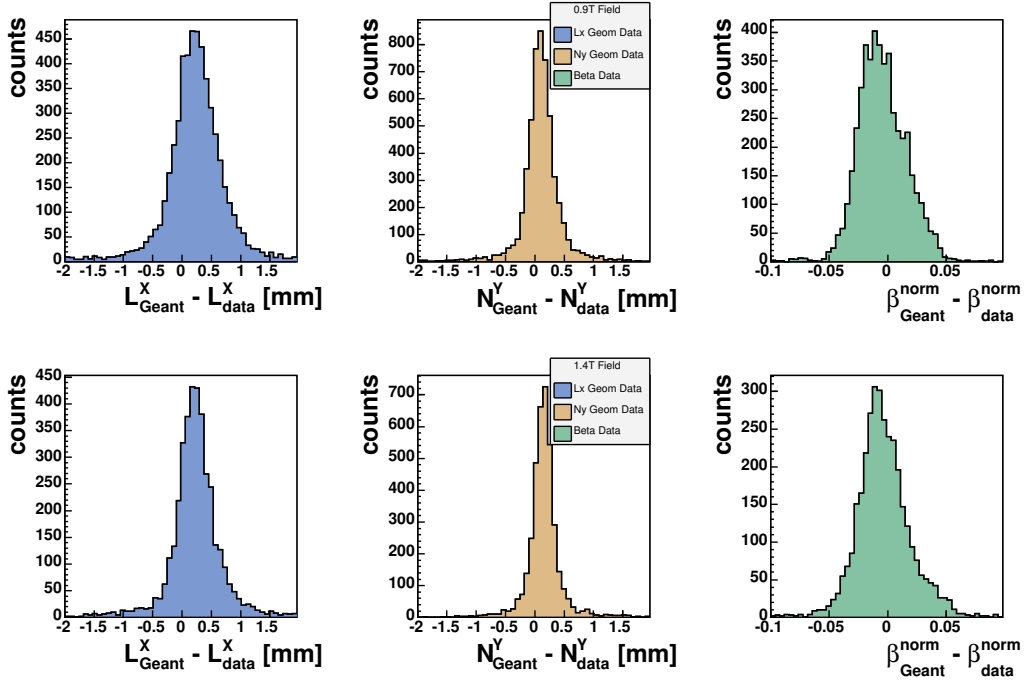


Figure 3.3: Distributions of the cut variables defined in eq. 3.7, 3.8 and 3.10 for each of the magnetic field settings. From top to bottom in rows: 0.9T, 1.4T. From left to right in columns:  $L_{Geant}^X - L_{data}^X$ ,  $N_{Geant}^Y - N_{data}^Y$  and  $\beta^{norm} = \frac{\frac{1}{\beta_F} - \frac{1}{\beta_{TF}}}{\frac{1}{\beta_F}}$

where  $C$  is a constant,  $\mu$  is a mean of the distribution.

Due to large differences in the mean values of the cut parameters distributions obtained for each D-detector paddle cut parameters have been produced and later applied with respect to each paddle  $\sigma_{D_i}^{LX}$ ,  $\sigma_{D_i}^{NY}$ ,  $\sigma_{D_i}^\beta$  (with  $i = \{1 \dots 16\}$ ). Fitted  $\sigma$  values as a function of the D detector paddle are shown in fig. 3.4. The efficiency of those cuts applied with  $n = 3$  is presented in section A.5. Figure 3.2 presents the mass spectra and the effect of applying the cuts with different values of  $n$ .

### 3.4 Event centrality estimation

The impact parameters and the average numbers of participating nucleons have been calculated within the nuclear overlap model introduced by Eskola in [EKL89]. The model represents a nucleus-nucleus collision in terms of binary collisions between nucleons.

Let us introduce the nuclear density  $n_A(r)$  normalized to the number of nucleons  $A$ :

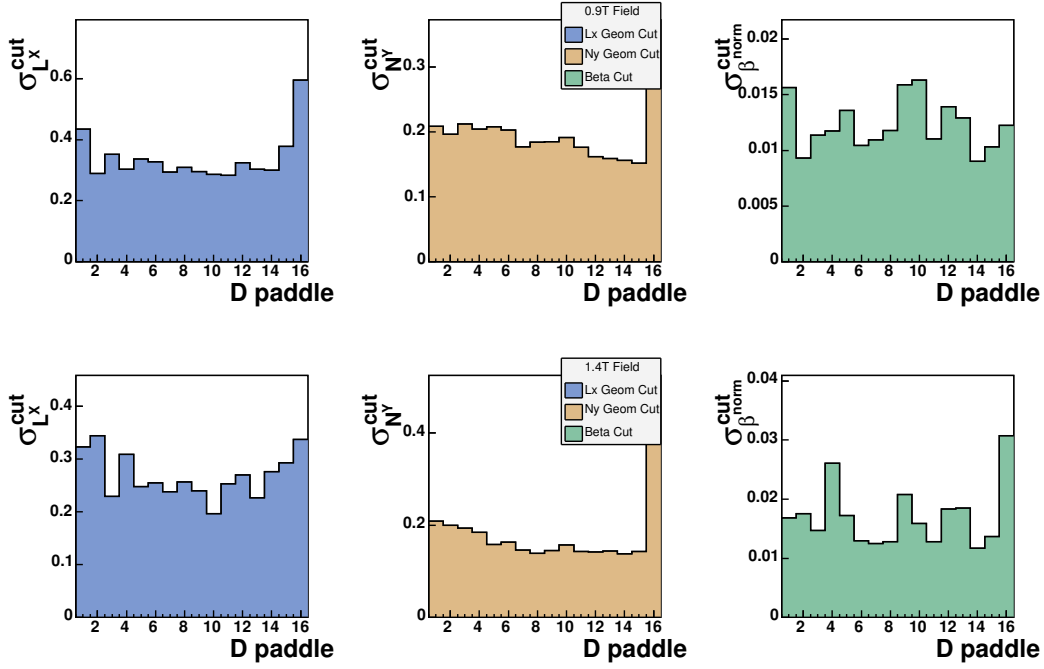


Figure 3.4: Cut parameters for each of the magnetic field settings. From top to bottom in rows: 0.9T, 1.4T. From left to right in columns:  $\sigma_{D_i}^{LX}$ ,  $\sigma_{D_i}^{NY}$ ,  $\sigma_{D_i}^{\beta}$

$$\int d^3r n_A(r) = A. \quad (3.11)$$

And the thickness function:

$$T_A(b) = \int_{-\infty}^{\infty} dz n_A(\sqrt{b^2 + z^2}), \quad (3.12)$$

also normalized to  $A$

$$\int d^2b T_A(b) = A. \quad (3.13)$$

Variable  $z$  is the longitudinal coordinate and  $\bar{b}$  is a two dimensional vector in the transverse plane ( $b = |\bar{b}|$ ). Thus, the overlap function  $T_{AB}(b)$  is defined as

$$T_{AB}(b) = \int d^2b_1 d^2b_2 \delta^2(\bar{b} - \bar{b}_1 - \bar{b}_2) T_A(\bar{b}_1) T_B(\bar{b}_2). \quad (3.14)$$

And it is normalized according to

$$\int d^2b T_{AB}(b) = AB. \quad (3.15)$$

Defined quantities compose the set necessary for calculating the number of binary collisions  $N_{BinCol}$  for a nucleus  $A$  crossing the nucleus  $B$  at impact parameter  $b$ :

$$N_{BinCol} = \sigma^{NN} T_{AB}(b). \quad (3.16)$$

Using the overlap model and assuming that the integrated spectra of the target detector multiplicity  $M_t$  acquired with the minimum bias trigger (see fig. 3.5) is proportional to the total reaction cross-section  $\sigma_{tot}^{rea}$  such that:

$$\sigma_{tot}^{rea} = c \cdot \int dM_t, \quad (3.17)$$

one can estimate the impact parameter range and the average number of participating nucleons for a set of arbitrary centrality bins.

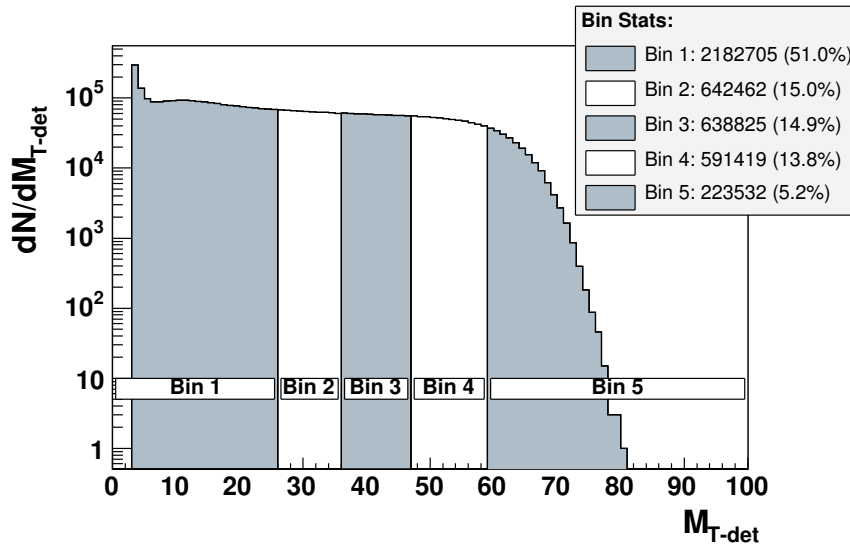


Figure 3.5: Target detector multiplicity spectrum separated into 5 centrality classes - used in the centrality estimation of an event and the average nucleon participant number.

The target detector spectrum shown in the fig.3.5 has been divided into 5 centrality bins. Each bin contains certain percentage of the integral from the formula 3.17. A detailed description of the divisions, corresponding impact parameters and average numbers of participants calculated with a dedicated computer program [Mis04], are presented in the table 3.1. Additionally, the numbers of participants from the projectile and the target as a function of the impact parameter have been presented in fig.3.6.



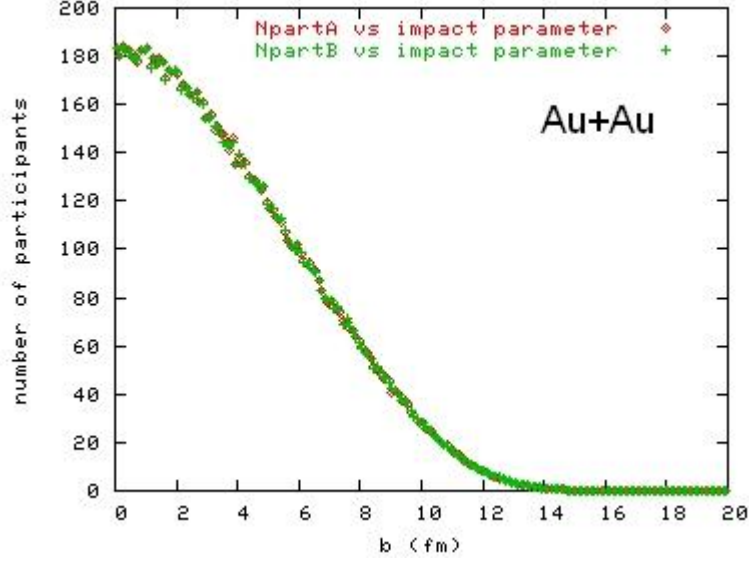


Figure 3.6: Numbers of participating nucleons of the target and the projectile as a function of the collisions impact parameter. Result of the nuclear overlap model calculation [Mis04].

Bin No.	$\% \sigma_{tot}^{rea}$	b[fm]	$\langle N_{part} \rangle$	$\langle N_{coll} \rangle$
1	51.0	> 10.5	13.0	13.0
2	15.0	8.5-10.5	70.8	96.6
3	14.9	6.4-8.5	140.6	237.5
4	13.8	3.3-6.4	235.5	464.2
5	5.2	< 3.3	332.0	720.6

Table 3.1: The centrality bins selection as well as the calculated average number of participants and the average number of collisions.

### 3.5 Reaction plane determination

For the reaction plane reconstruction, a variation of the Fourier coefficients analysis method has been applied [Oll95]. For each event, one defines the  $n^{th}$  Fourier coefficient  $\vec{Q}_n$  as:

$$\vec{Q}_n = \sum_{i=1}^N w_i e^{in\phi_i}, \quad (3.18)$$

where  $N$  is the multiplicity of particles detected in the event,  $\phi_i$  is the azimuthal angle of the particle  $i$  and the  $w_i$  is a weight factor. Usually the weight  $w_i$  is chosen to be the

transverse energy of the particle  $i$  or its transverse momentum, however in the case of the detector used in the experiment it is sufficient to choose  $w_i = \sin(\theta_i)$ , where  $\theta_i$  is the polar angle of the particle  $i$  with respect to the beam axis calculated from the hit position in the small angle hodoscope. Hence, the Fourier coefficients can be written as:

$$\vec{Q}_n = (Q_n^x, Q_n^y) \quad (3.19)$$

with

$$Q_n^x = \sum_{i=1}^N w_i \cos(n\phi_i), \quad (3.20)$$

$$Q_n^y = \sum_{i=1}^N w_i \sin(n\phi_i). \quad (3.21)$$

where  $\phi_i$  is the azimuthal angle of the particle  $i$  calculated from the hit position in the small angle hodoscope.

Finally the orientation of the reaction plane in space is given by the azimuthal angle  $\Phi_{RP}$  which can be calculated for each event from the relation:

$$\Phi_{RP} = \arctan\left(\frac{Q_n^y}{Q_n^x}\right)_{n=1}. \quad (3.22)$$

Expanding the particle spectra in harmonics ([SV96]) of the azimuthal angle with respect to  $\Phi_{RP}$

$$E \frac{dN}{d^3p} = \text{const} \cdot (1 + 2v_1 \cos(\Phi - \Phi_{RP}^{(n)}) + 2v_2 \cos(2(\Phi - \Phi_{RP}^{(n)})) + \dots) \quad (3.23)$$

one defines parameters  $v_m$  corresponding to the mean values

$$v_m = \langle \cos(m(\Phi - \Phi_{RP}^{(n)})) \rangle. \quad (3.24)$$

The parameter  $v_1$  is assigned to directed flow and  $v_2$  to elliptic flow.

In order to select the spectators of a collision, an additional cut in the time of flight of the particles detected in the small angle hodoscope is necessary. After the time of flight calibration of the hodoscope modules, the window in the particles velocity  $0.75 < \beta < 1.1$  has been applied as a selection criterion for the spectator-like fragments. Additionally, to remove the quantization of the detector, individual hit positions  $x^{hit}, y^{hit}$  are randomized within the acceptance of a given detector module  $i$ , which registered a particle:

$$x_i - \frac{a_i}{2} < x^{hit} < x_i + \frac{a_i}{2}, \quad (3.25)$$

$$y_i - \frac{b_i}{2} < y^{hit} < y_i + \frac{b_i}{2}, \quad (3.26)$$

where  $x_i$  and  $y_i$  define the position of the module  $i$ ,  $a_i$  and  $b_i$  are its width and height, respectively.

### 3.6 Reaction plane normalization

In the collision of heavy-ions, none of the directions of the impact parameter vector  $\vec{b}$  is preferred. Therefore in the ideal case, the azimuthal angular distribution of the reaction plane angle  $\Phi_{RP}$  is isotropic. Thus, the minimum bias measurements ought to provide a flat distribution. However, even small misalignment of the beam position or some detector specific features, such as poor acceptance, detector's granularity or hardware malfunctions may cause a significant distortion. Indeed, this is the case here. The upper row of figure 3.7 shows the  $dN/d\phi$  distributions before correction for each of the centrality bins. In order to account for this asymmetry a normalization procedure for each centrality class separately, has been applied.

The first step in the normalization procedure is to define a part of the hodoscope which will serve as an active area for the reaction plane reconstruction. An optimal choice is a symmetric shape in the azimuthal angle. The selection is chosen to be an area in between two circles (see fig.3.8). One around the center, where the modules have been removed allowing the beam passage, and second with a maximum acceptable diameter fitting inside the hodoscope plane. Let us define the new acceptance in the polar angle  $\delta\theta^{acc}$ :

$$\theta_I < \delta\theta^{acc} < \theta_{II}, \quad (3.27)$$

where the polar angle ( $\theta$ ) is defined by the beam axis and a vector pointing from the target to an arbitrary position in the hodoscope plane. Thus  $\theta_I$  describes the inner circle and  $\theta_{II}$  the outer one. Only hits contained within  $\delta\theta^{acc}$  are taken into the analysis.

In the second step of the procedure, the  $\delta\theta^{acc}$  area is divided into 3 equal sub-rings  $\delta\theta_j^{acc}$  (with  $j = \{1, 2, 3\}$ ) of about  $3^\circ$  each. These rings are further divided into a series of slices, with a constant  $\delta\phi_i = 3^\circ$  (with  $i = 1..K$ ) acceptance. For each of the  $\delta\phi_i$  slices in a single ring  $\delta\theta_j^{acc}$ , a correction parameter  $\alpha_i^j$  is calculated as the count rate in this slice  $N_i^j$  normalized to the mean count rate in the ring:

$$\alpha_i^j = \frac{N_i^j}{\frac{\sum_k^K N_k^j}{K}}. \quad (3.28)$$

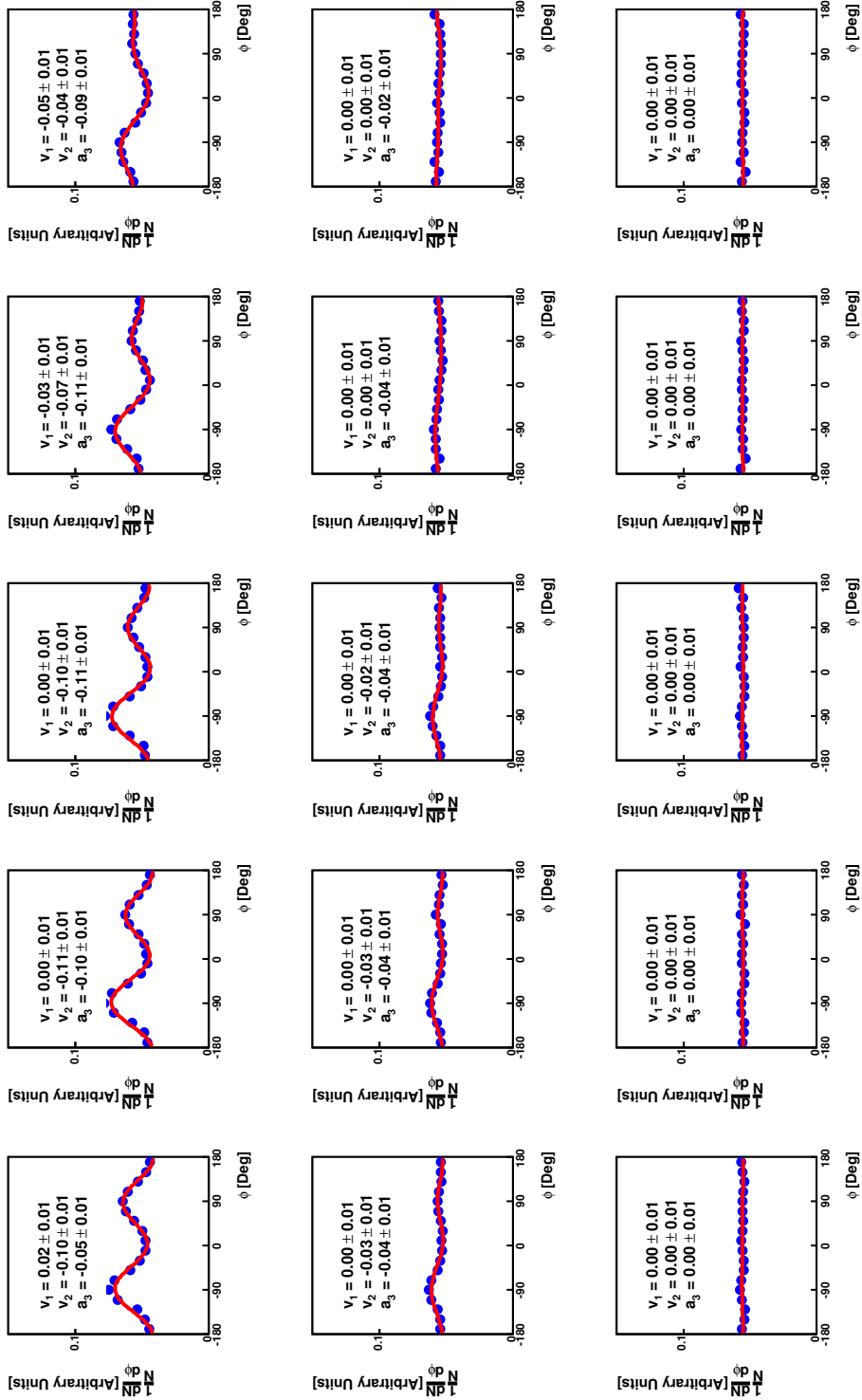


Figure 3.7: *Minimum bias normalization procedure (see text). For each of the central bins (columns from LHS least central to most central on RHS) the upper row shows uncorrected data, the middle row shows the  $dN/d\phi$  distributions after the symmetrization procedure, and finally the last row presents the distributions after the last correction. Each data sample has been fitted with a function defined by 3.29 - values showing the anisotropy presented in the graphs.*

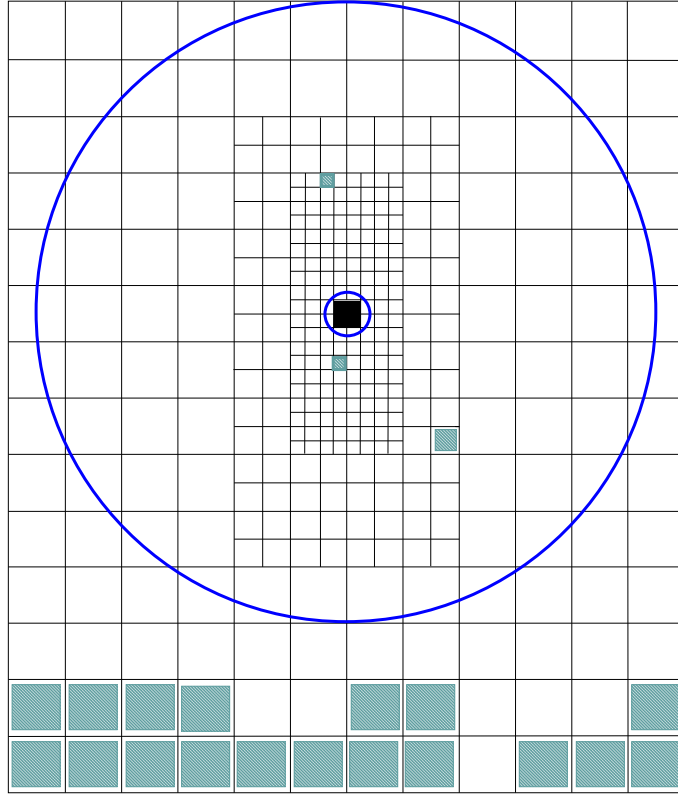


Figure 3.8: Schematic front view of the small angle hodoscope showing its granularity. Shaded elements symbolize some faulty modules. The black square in the center is empty space after removal of 4 smallest detector modules allowing free passage of the beam. The two circles define a shape, fully symmetric in the azimuthal angle. This area is taken into account in the analysis.

After applying the geometrical acceptance cut, defined by 3.27, and the correction with parameters 3.28, the resulting distributions for each of the centrality bins (middle row in fig. 3.7) are fitted with:

$$\frac{dN}{d\Phi_{RP}} \approx 1 + 2v_1 \cos(\Phi_{RP}) + 2v_2 \cos(\Phi_{RP}) + a_3 \sin(\Phi_{RP}). \quad (3.29)$$

The last step of the normalization procedure consists of weighting the event plane angle  $\Phi_{RP}$  with a correction function 3.29. The corrected minimum bias reaction plane angle distribution is to be seen in the bottom row in the figure 3.7.

## 3.7 Reaction plane resolution

### 3.7.1 Method description

The method of obtaining the correction parameters used here is based on more detailed derivations shown in [Oll97].

Azimuthal distributions expressed as Fourier series (see formula 3.23) define asymmetry coefficients  $v_n$  (eq. 3.24). In order to extract these parameters from the data one has to take into account that the experimental determination of a reaction plane is limited by detector coverage, detector resolution, and finite-number fluctuations. The measured azimuthal angle  $\psi$  in an event may differ from the true azimuthal angle  $\phi$  by a finite angle  $\Delta\phi$ . Averaging over many events, assuming that  $\phi$  and  $\Delta\phi$  are statistically independent, one obtains the relation between the measured and true Fourier coefficients:

$$\langle \cos(n\psi) \rangle = \langle \cos(n\phi) \rangle \langle \cos(n\Delta\phi) \rangle. \quad (3.30)$$

In order to reconstruct the true distribution the correction factors  $\langle \cos(n\Delta\phi) \rangle$  have to be known.

The distribution of the azimuthal angle deviation  $\Delta\phi$  and the Fourier coefficients can be expressed in terms of a real parameter  $\chi$ , which measures the accuracy of the reaction plane determination:

$$\frac{dN}{d\Delta\phi} = \frac{1}{\pi} \exp(-\chi^2) [1 + z\sqrt{\pi}[1 + \text{erf}(z)] \exp(z^2)], \quad (3.31)$$

$$\langle \cos(n\Delta\phi) \rangle = \frac{\sqrt{\pi}}{2} \chi e^{-\chi^2/2} [I_{\frac{n-1}{2}}(\frac{\chi^2}{2}) + I_{\frac{n+1}{2}}(\frac{\chi^2}{2})]. \quad (3.32)$$

where  $z = \chi \cos \Delta\phi$ ,  $\text{erf}(x)$  is the error function and  $I_k$  is the modified Bessel function of order  $k$ .

The parameter  $\chi$  can be determined in terms of statistical analysis of the azimuthal angle differences ( $\Delta\phi$ ) calculated for 2 (or more) sub-events of a given event. In the procedure presented here, each event was randomly divided into two sub-events containing half of the particles each. The  $\vec{Q}$  vectors are reconstructed for the sub-events separately resulting in  $\vec{Q}_A$  and  $\vec{Q}_B$ . Since each sub-event contains only  $N/2$  particles therefore the corresponding  $\chi$  parameter must be scaled:  $\chi_A = \chi_B = \chi/\sqrt{2}$  and the distribution of the relative angle  $\Delta\Phi_R = |\Phi_A - \Phi_B|$  can be calculated analytically as:

$$\frac{dN}{d\Delta\Phi_R} = \frac{e^{-\chi_A^2}}{2} \left\{ \frac{2}{\pi} (1 + \chi_A^2) + z(I_0(z) + L_0(z)) + \chi_A^2 (I_1(z) + L_1(z)) \right\} \quad (3.33)$$

where  $z = \chi_A^2 \cos \Delta\Phi_R$ ,  $L_0$  and  $L_1$  are modified Struve functions.

### 3.7.2 Calculation of the correction parameters

The data from the small angle hodoscope acquired with the minimum bias trigger was divided for each event into two subsets  $A_{data}$  and  $B_{data}$ . For each subset the orientations of the reaction plane were calculated ( $\Phi_{RP}^{A_{data}}$ ,  $\Phi_{RP}^{B_{data}}$ ) and the differences

$$\Delta\Phi_{RP}^{data} = |\Phi_{RP}^{A_{data}} - \Phi_{RP}^{B_{data}}| \quad (3.34)$$

accumulated over the events, separately for each centrality class. In order to obtain the  $\chi$  and correction parameters for each centrality the  $\Delta\Phi_{RP}^{data}$  distributions were fitted with function defined by eq. 3.33. The correction parameters were then obtained with formula 3.32.

For the azimuthal emission pattern parameterized in the form

$$\frac{dN}{d\phi} \approx 1 + 2v_1 \cos(\phi) + 2v_2 \cos(2\phi) \quad (3.35)$$

the corrected (real)  $v_1^{corr}$  and  $v_2^{corr}$  parameters were calculated as:

$$v_1^{corr} = \frac{v_1}{\langle \cos(\Delta\phi) \rangle} \quad (3.36)$$

and

$$v_2^{corr} = \frac{v_2}{\langle \cos(2\Delta\phi) \rangle}. \quad (3.37)$$

The values of the correction factors  $\langle \cos(\Delta\phi) \rangle$  and  $\langle \cos(2\Delta\phi) \rangle$  extracted from the procedure are listed in table 3.7.2. Additionally systematic error estimates for  $v_1$  and  $v_2$  (also shown in table 3.7.2) have been derived taking into account the errors given by the fits and the uncertainties related to small deviations of the calculations of the reaction plane resolution performed for each individual measurement setting of the magnetic field and laboratory angle. These errors are later added to the statistical uncertainties and indicated as a one number on all of the presented plots.

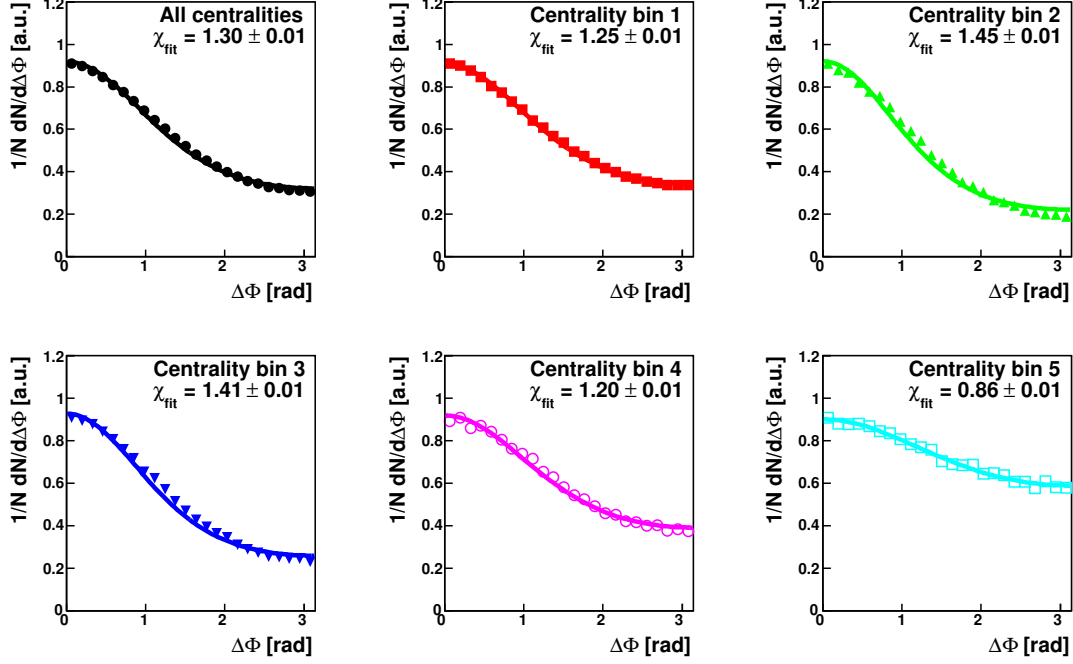


Figure 3.9:  $\Delta\Phi_{RP}^{data}$  distributions for different centrality selections.

Centrality Bin	$\chi/\sqrt{2}$	$\langle\cos(\Delta\phi)\rangle$	$\langle\cos(2\Delta\phi)\rangle$	Syst. Err. $v_1$	Syst. Err. $v_2$
Integrated	$1.30\pm 0.00$	$0.81\pm 0.01$	$0.52\pm 0.01$	$\pm 0.005$	$\pm 0.008$
1	$1.25\pm 0.01$	$0.80\pm 0.01$	$0.50\pm 0.01$	$\pm 0.005$	$\pm 0.008$
2	$1.45\pm 0.01$	$0.85\pm 0.01$	$0.58\pm 0.01$	$\pm 0.005$	$\pm 0.008$
3	$1.41\pm 0.01$	$0.84\pm 0.01$	$0.57\pm 0.01$	$\pm 0.005$	$\pm 0.008$
4	$1.20\pm 0.01$	$0.78\pm 0.01$	$0.47\pm 0.01$	$\pm 0.005$	$\pm 0.008$
5	$0.86\pm 0.01$	$0.64\pm 0.01$	$0.29\pm 0.01$	$\pm 0.011$	$\pm 0.016$

Table 3.2: The correction parameters for reaction plane resolution and the systematic error estimates for  $v_1$  and  $v_2$ .





# Chapter 4

## Experimental results

### 4.1 The Measurement

The experiment discussed in this dissertation took place in the summer of 2001 at GSI facility in Darmstadt. The beam delivered to the experimental area had a kinetic energy of  $295.5\text{GeV}$  ( $1.5A \cdot \text{GeV}$ ) and consisted of gold nuclei  $^{197}\text{Au}^{79+}$ . The intensities reached  $5 \cdot 10^8$  particles per spill with a spill length of about 10s. In a single cycle after the primary acceleration in the linear accelerator UNILAC, not fully stripped ions ( $^{197}\text{Au}^{63+}$ ) were injected into SIS synchrotron and accelerated to about  $0.3A\text{GeV}$ . From there the beam was transported to the ESR Storage Ring. Before entering the ring, the beam traversed a foil and was fully stripped. Then the fully stripped ions were injected to the ESR storage ring in order to minimize the transverse spread of the beam particles with an electron cooler. The last stage of the cycle was the second acceleration in the SIS synchrotron until the full energy has been reached. One full cycle took approximately 30s.

In the experiment a gold  $^{197}\text{Au}$  target,  $0.5\text{mm}$  thick was used, which corresponds to 1.8% interaction probability for each incident  $\text{Au}$  projectile.

### 4.2 Particle yields

The main goal of the experiment was to measure the azimuthal angular distribution of kaons and antikaons close to mid-rapidity. The measurements of  $K^+$  and  $K^-$  mesons were performed with two magnetic field settings ( $-0.9T$  and  $-1.4T$ ) and at two spectrometer angles ( $\theta_{spec} = \{40^\circ, 48^\circ\}$ ) which cover a phase-space region close to mid-rapidity ( $0.2 < y/y_{beam} < 0.55$ ) and transverse momentum range of  $0.2 < p_t < 0.8$ . In addition, positively charged particles were measured also at the spectrometer angle of  $72^\circ$  and the two magnetic field settings  $0.9T$  and  $1.4T$ . As a result the direct comparison of  $K^+$  and  $K^-$  mesons is possible for the measurements at  $36^\circ < \theta_{lab} < 52^\circ$ . The phase

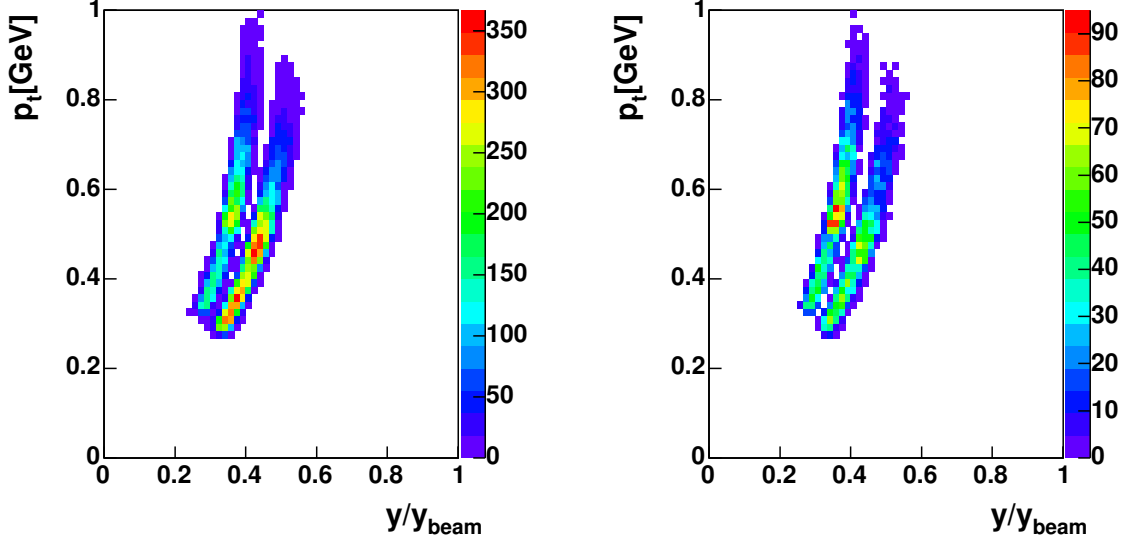


Figure 4.1: Phase space populations of  $K^+$  (left) and  $K^-$  (right) measured at spectrometer angles 40deg and 48deg.

space populations of  $K^+$  and  $K^-$  mesons measured close to mid-rapidity are presented in figure 4.1.

### 4.3 Production cross-sections

The procedure of obtaining differential cross-sections has been described in the appendix A. Double differential cross-sections for positively and negatively charged pions and kaons are presented in figures 4.2 and 4.4. Figures 4.3 and 4.5 show comparisons of the obtained cross-sections of pions and kaons with the previous measurements by KaoS collaboration [För03]. The cross-sections are in agreement within the systematic uncertainties of these measurements. The systematic errors of the cross-sections presented in this work are not indicated on the plots, but summarized in A.8.

After transformation to the center of mass frame (see appendix B), the invariant cross-section

$$\sigma_{inv} = E \frac{d^3\sigma}{dp^3} \quad (4.1)$$

for  $K^+$  and  $K^-$  mesons has been reconstructed. The distributions have been fitted with a Boltzmann function

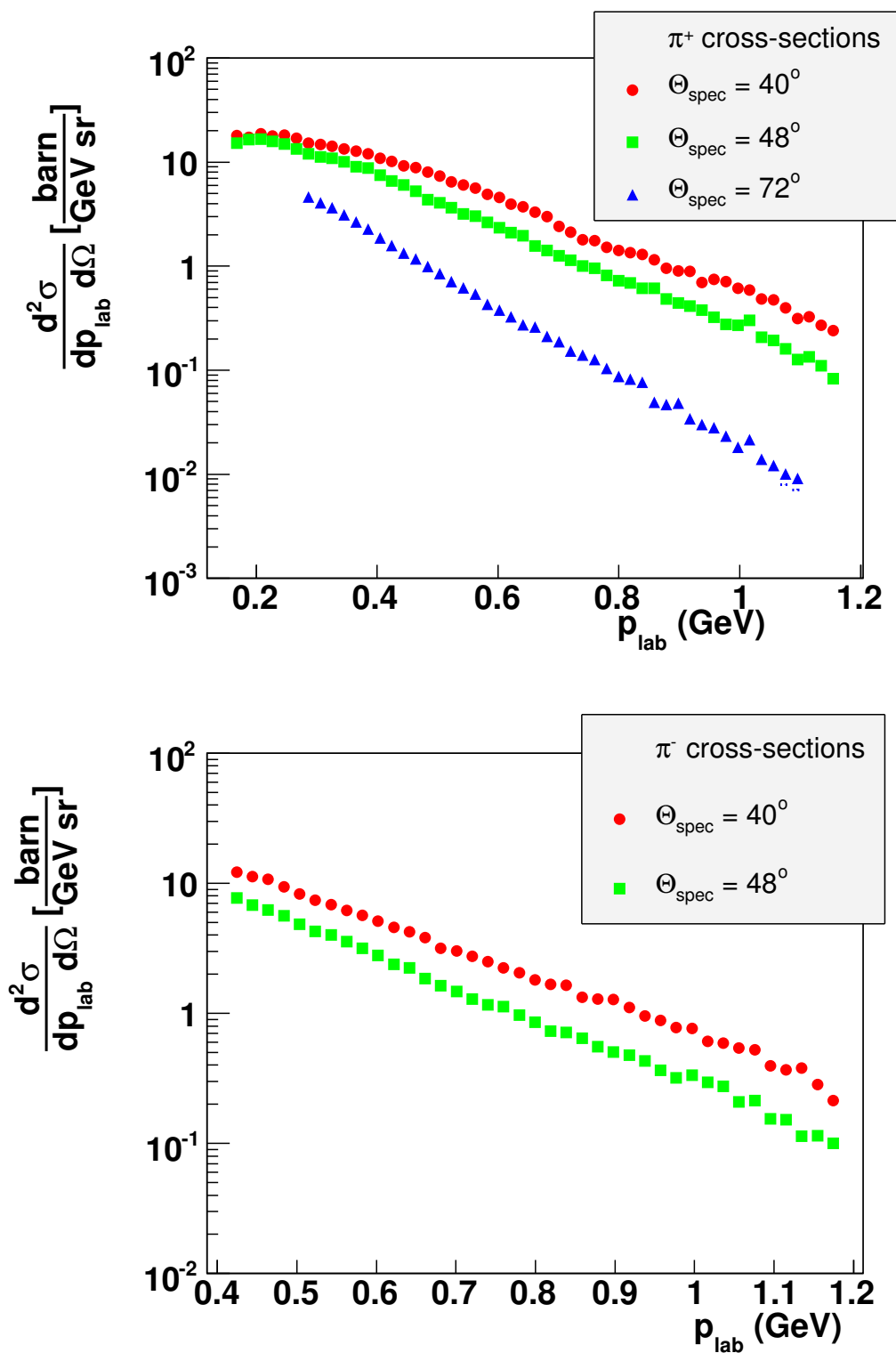


Figure 4.2: Double differential cross-sections of measured pions (upper figure -  $\pi^+$ , lower figure -  $\pi^-$ ) at different spectrometer angles as a function of the laboratory momentum.

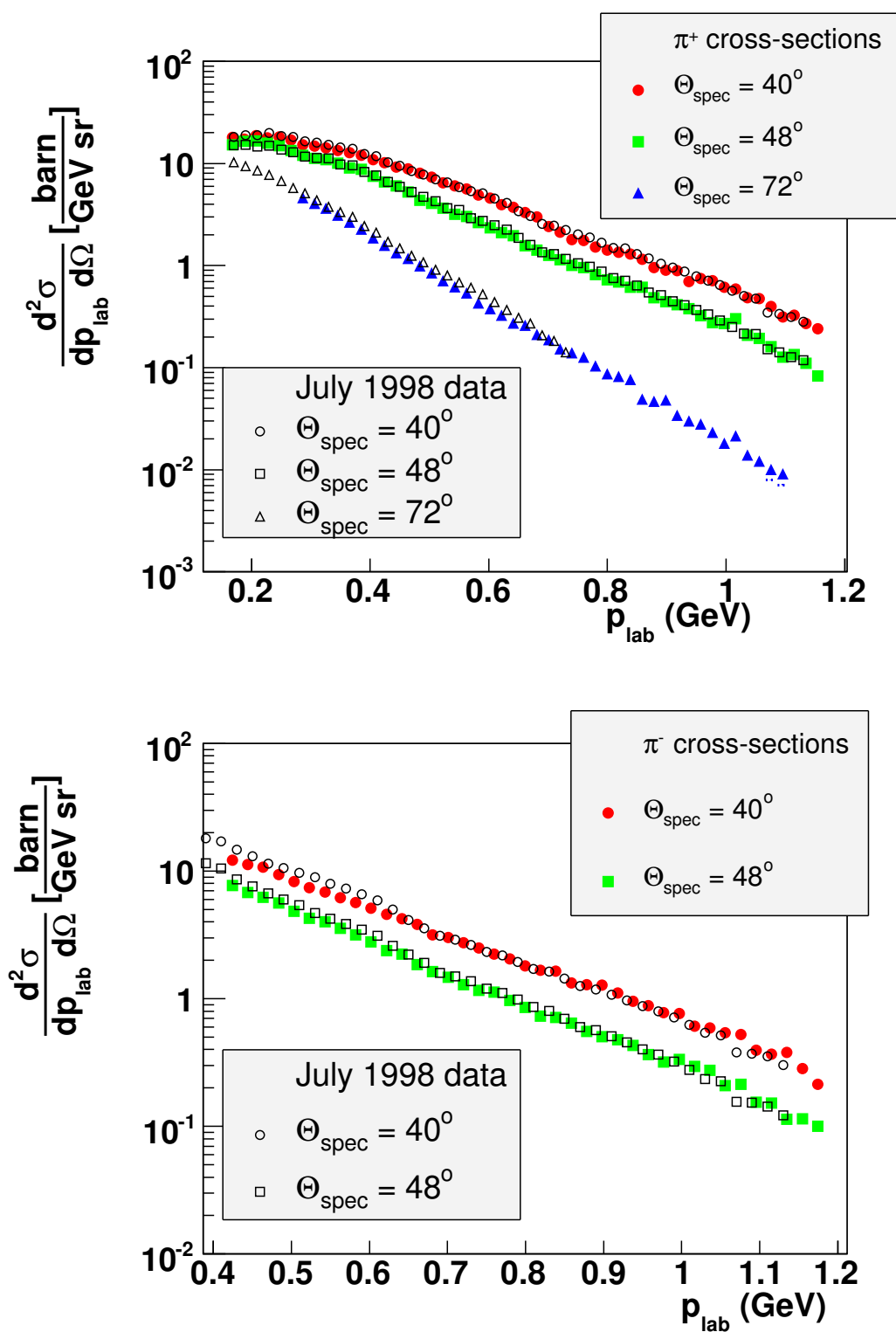


Figure 4.3: Double differential cross-sections of measured pions (upper figure -  $\pi^+$ , lower figure -  $\pi^-$ ) at different spectrometer angles as a function of the laboratory momentum compared to the previous measurements by KaoS collaboration.

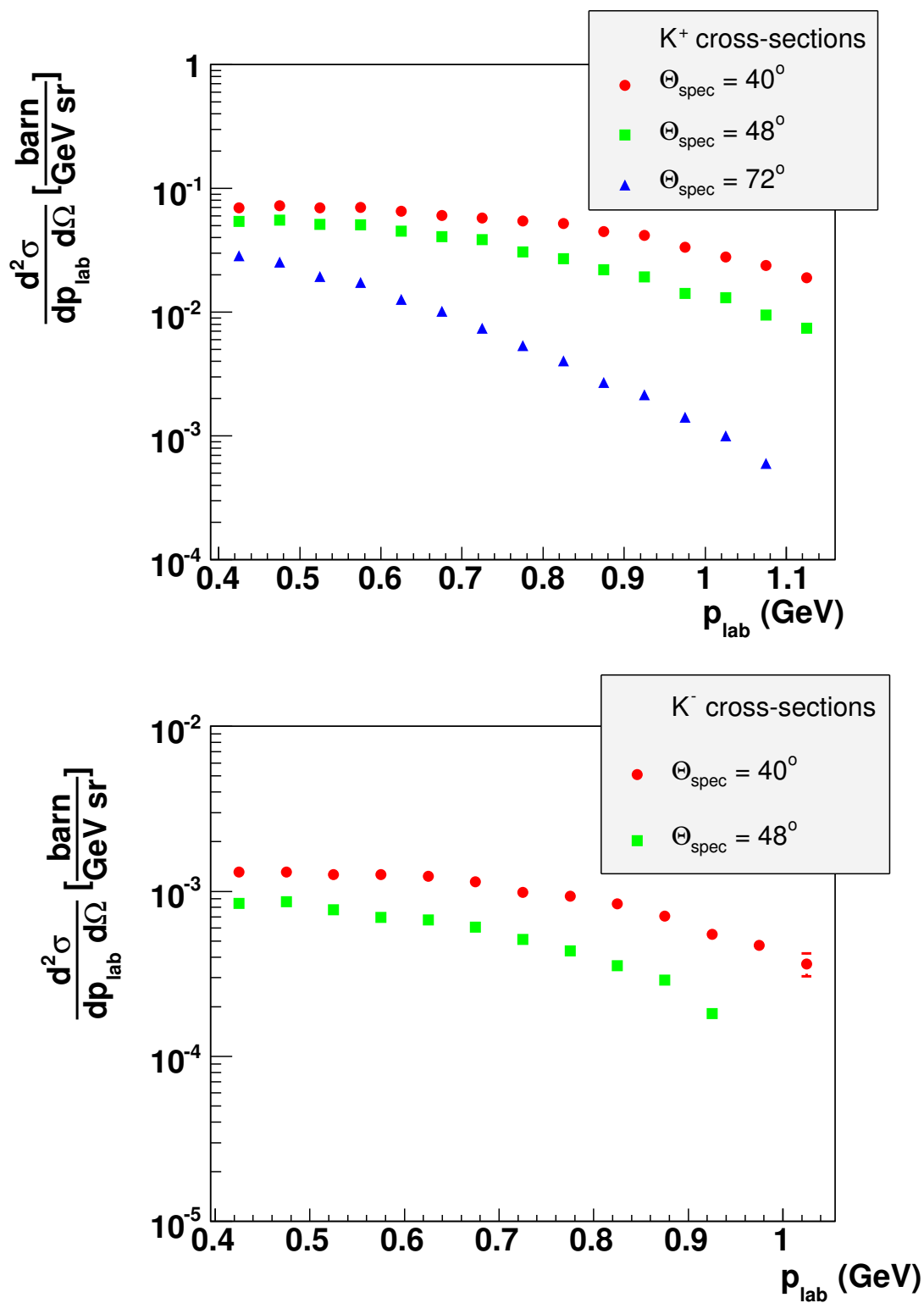


Figure 4.4: Double differential cross-sections of measured kaons (upper) and antikaons (lower) at different spectrometer angles as a function of the laboratory momentum.

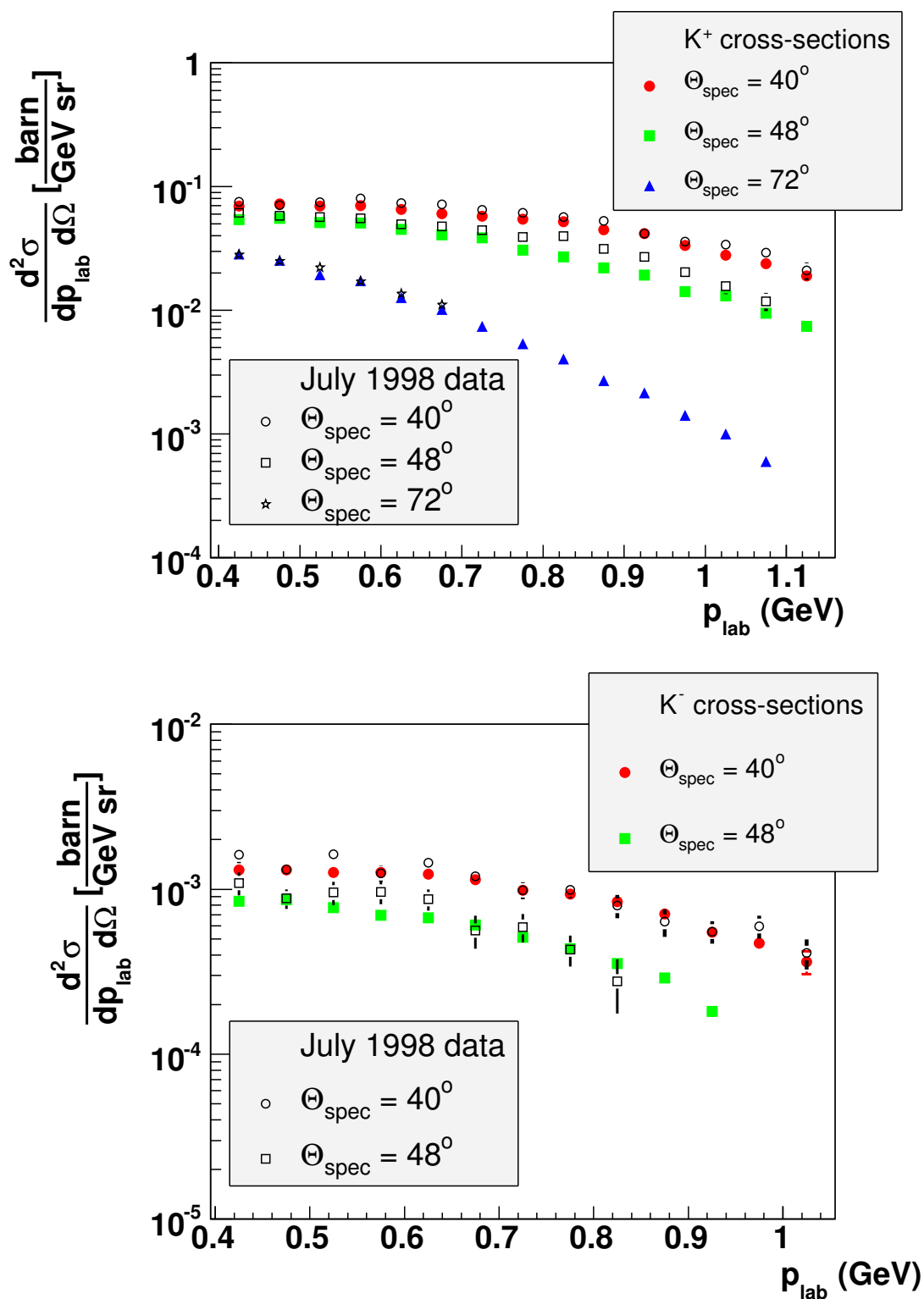


Figure 4.5: Double differential cross-sections of measured kaons and antikaons at different spectrometer angles as a function of the laboratory momentum compared to the previous measurements by KaoS collaboration.

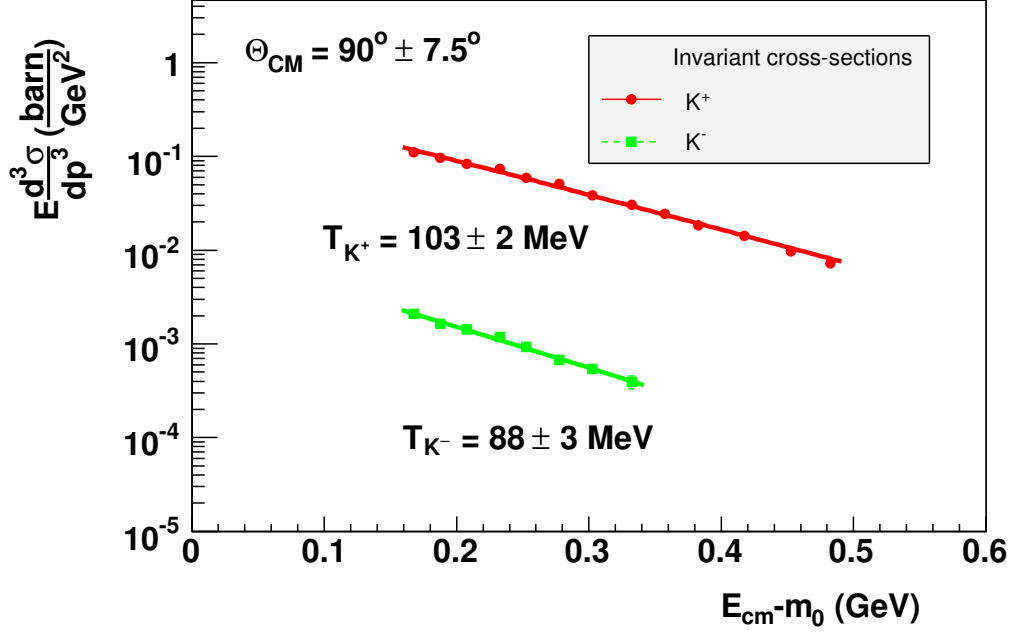


Figure 4.6: Invariant cross sections of  $K^+$  and  $K^-$  as a function of the energy in the center of mass system. The data have been selected for  $\Theta_{cm} = 90^\circ \pm 7.5^\circ$ . Distributions were fitted with Boltzmann function defined by formula 4.2.

$$E_{cm} \frac{d^3\sigma}{dE_{cm}} = C \cdot E_{cm} \exp\left(-\frac{E_{cm}}{T}\right) \quad (4.2)$$

where  $C$  is a constant,  $E_{cm}$  is the energy in the center of mass frame, and  $T$  is the inverse slope parameter. Figure 4.6 presents the invariant cross-sections of kaons and antikaons selected with a condition for emission angle in the center of mass frame  $\Theta_{cm}$  around  $90deg$  ( $82.5^\circ < \Theta_{cm} < 97.5^\circ$ ). The values of inverse slope parameters obtained by the fits  $T_{K^+} = 103 \pm 2 MeV$  and  $T_{K^-} = 88 \pm 3 MeV$  are in agreement with previous observations by KaoS collaboration [Stu01, För03] within the experimental uncertainties.



## 4.4 Azimuthal angular distributions

The emission patterns presented in this chapter are parametrized with a function

$$\frac{dN}{d\phi} \approx 1 + 2v_1 \cos(\phi) + 2v_2 \cos(2\phi). \quad (4.3)$$

where  $v_1$  and  $v_2$  are the anisotropy parameters of directed flow and elliptic flow respectively, corrected for the reaction plane resolution (see section 3.7). The distributions and values presented in figures of the next sections are corrected for the reaction plane resolution. The errors indicated on the plots contain both statistical and systematic uncertainties. In order to assure as background free as possible angular distributions of kaons and antikaons the azimuthal emission patterns have been reconstructed with cut widths of  $n = 3$  ( $3\sigma$ ) for kaons and  $n = 2$  ( $2\sigma$ ) in case of antikaons (as defined in section 3.3.3). In cases where the background was still visible the azimuthal emission pattern of the particles in the near of the kaon ( $3\sigma^{mass}$ ) mass region has been reconstructed, however, the flow signal, both  $v_1$  and  $v_2$ , has been on the order of 2% and taking into account the contamination factor being below 10% the additional uncertainties in the reconstructed flow parameters for kaons and antikaons is of the order of 0.002 and therefore it is considered as a part of the systematic error.

### 4.4.1 Collective flow measurements close to target rapidity

#### Protons

An interesting observable for collective flow phenomenon in heavy-ion collision is the azimuthal emission pattern of protons. One expects that nucleons, heavier than pions or kaons, carry most of the flow. Figure 4.7 presents multiplicities of measured protons as a function of the transverse momentum and normalized rapidity. Particles were measured at the 3 different spectrometer angles 40, 48 and 72 degrees. The range of explored rapidities is in the backward hemisphere. Azimuthal emission pattern of protons with transverse momentum larger than 0.4 GeV for all measured rapidities is shown in figure 4.8. The large (negative) value of the directed flow parameter  $v_1$  indicates a strong asymmetry in favor of the direction towards the target. Additionally a negative  $v_2$  indicates enhanced out-of-plane emission.

In order to study the collective motion of particles in more detail the data set has been divided into several rapidity regions. Figure 4.9 shows the azimuthal emission pattern of protons for two different rapidities: low ( $0.05 < y/y_{beam} < 0.15$ ) and high ( $0.15 < y/y_{beam} < 0.45$ ). It is observed that anisotropy parameters of directed flow ( $v_1$ ) and elliptic flow ( $v_2$ ) vary with rapidity. Figure 4.10 shows  $v_1$  and  $v_2$  parameters as a function of normalized rapidity. Close to target rapidity the directed flow of protons is negative, and when approaching mid-rapidity, lowers its strength, while the elliptic flow

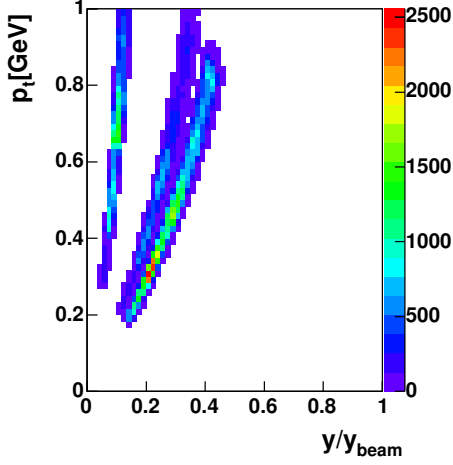


Figure 4.7: Phase space populations of protons measured at spectrometer angles 40deg, 48deg and 72deg.

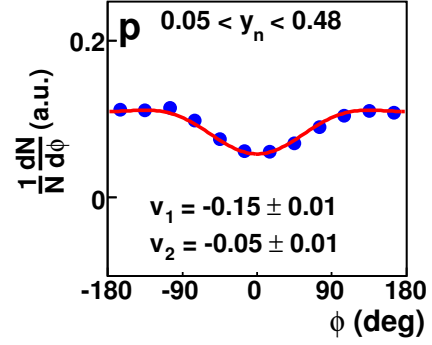


Figure 4.8: Azimuthal angular distribution of protons from Au+Au at 1.5AGeV. Data selected as events with  $b > 6.4\text{fm}$ , rapidity range of  $0.05 < y/y_{\text{beam}} < 0.5$  and transverse momentum  $0.4 < p_t < 1.5$ .

component starts slightly negative and moves towards more negative values. The out-of-plane emission close to mid-rapidity has been already observed by other experiments [G<sup>+</sup>90, L<sup>+</sup>93, B<sup>+</sup>96].

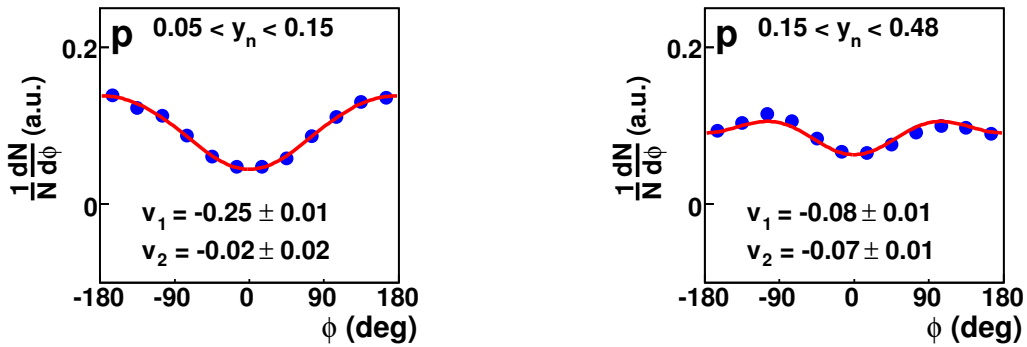


Figure 4.9: Azimuthal angular distributions of protons from Au+Au at 1.5AGeV for two rapidity regions:  $0.05 < y/y_{\text{beam}} < 0.15$  (left) and  $0.15 < y/y_{\text{beam}} < 0.45$  (right). Data selected with impact parameter  $b > 6.4\text{fm}$  and transverse momentum  $0.4 < p_t < 1.5$ .

For the data set closest to target rapidity (72 degrees measurement) the directed flow has been studied as a function of transverse momentum of the protons (see fig. 4.11). The anisotropy parameter  $v_1$  is negative over the range of measured  $p_t$ . The flow strength

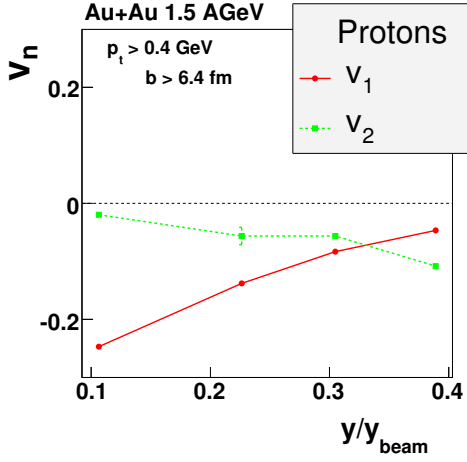


Figure 4.10: Directed and elliptic flow parameters of protons as a function of normalized rapidity. Data selected with impact parameter  $b > 6.4 \text{ fm}$  and transverse momentum  $0.4 < p_t < 1.5$ .

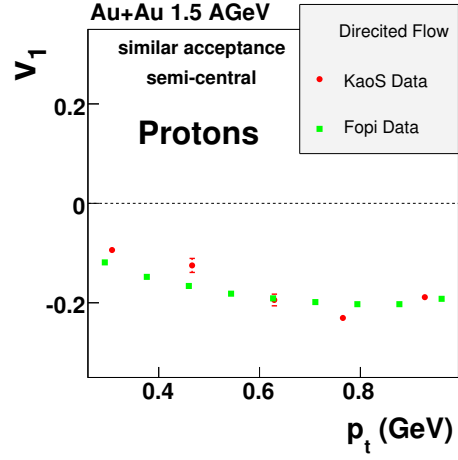


Figure 4.11: Directed flow of protons as a function of transverse momentum. Data recorded close to target rapidity ( $0.1 < y/y_{\text{beam}} < 0.23$ ) with centralities  $b > 6.4 \text{ fm}$ .

reaches an extremum around  $0.75 \text{ GeV}$  and the observed trend to decline towards zero agrees with the expected behavior as the collective flow should lower its strength for particles with  $p_t$  approaching zero. Figure 4.11 shows also a comparison of the data obtained by KaoS to the similar measurement by Fopi Collaboration [A<sup>+</sup>01, And05]. Data agree quite well and both data sets show similar trend of negative  $v_1$  over the  $p_t$  range.

### Pions

Measurements close to target rapidity were performed only for positive field settings, thus only positively charged particles were detected. The measured phase space distribution of pions at 72deg angle is presented in fig. 4.12, and the corresponding azimuthal emission pattern in fig. 4.13.

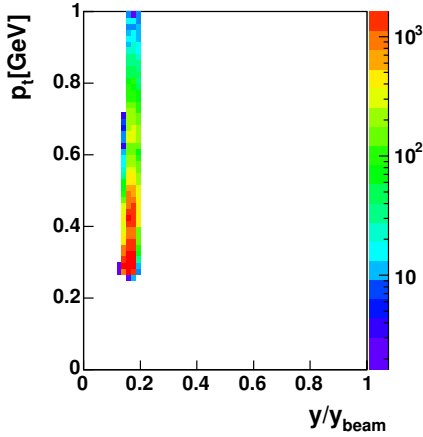


Figure 4.12: Phase space populations of  $\pi^+$  measured at spectrometer angle 72deg.

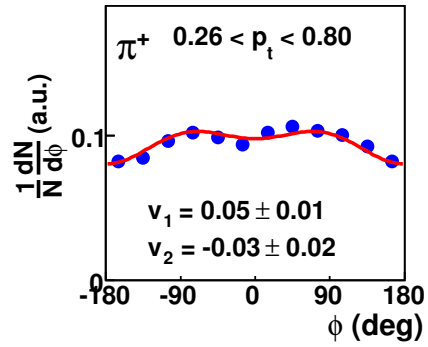


Figure 4.13: Azimuthal angular distribution of  $\pi^+$  mesons from Au+Au at 1.5AGeV. Data selected as events with  $b > 6.4\text{fm}$ , rapidity range of  $0.05 < y/y_{\text{beam}} < 0.25$  and transverse momentum  $0.2 < p_t < 0.8$ .

It shows the flow directed towards the forward hemisphere and a squeeze-out signal. Dividing the data into two transverse momentum sets (see fig.4.14) exhibits that the directed flow signal is driven by the low momentum particles and a pronounced out-of-plane emission in  $\pm 90\text{deg}$  is a characteristic of the high momentum pions.

Figure 4.15 shows the  $p_t$  dependence of the directed flow component  $v_1$  of pions close to target rapidity. The observed cross-over from positive to negative values of  $v_1$  as a function of transverse momentum provides an interesting view into the reaction dynamics. Data show that the high-energy pions are preferentially emitted towards the target spectator matter but low-energy particles are emitted in the opposite direction. The change of sign of the directed flow parameter  $v_1$  can be used to relate the transverse momenta to the time scale of a collision [W<sup>+</sup>00]. In the early stage of the collision particles are shadowed by the projectile spectator matter such that the enhanced emission towards the target is observed. On the other hand, in the late stage of the collision the situation is inverted, such that the target spectators shadow the flight path of the particles and an enhanced signal for  $v_1$  in the direction of projectile is generated. Therefore one may conclude that the high momenta particles are emitted earlier than the ones with low momenta. Moreover, let us

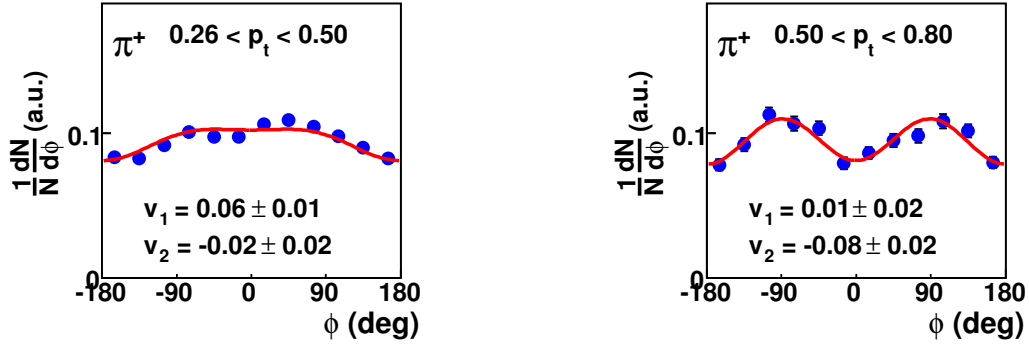


Figure 4.14: Azimuthal angular distribution of  $\pi^+$  mesons from Au+Au at 1.5 AGeV. Data selected as events with  $b > 6.4 \text{ fm}$ , rapidity range of  $0.05 < y/y_{\text{beam}} < 0.25$  and two transverse momentum  $0.2 < p_t < 0.5$  (left) and  $0.5 < p_t < 0.8$  (right).

note that specially in case of low momenta  $\pi^+$ , the Coulomb repulsion is the additional force pushing particles away from the collision zone.

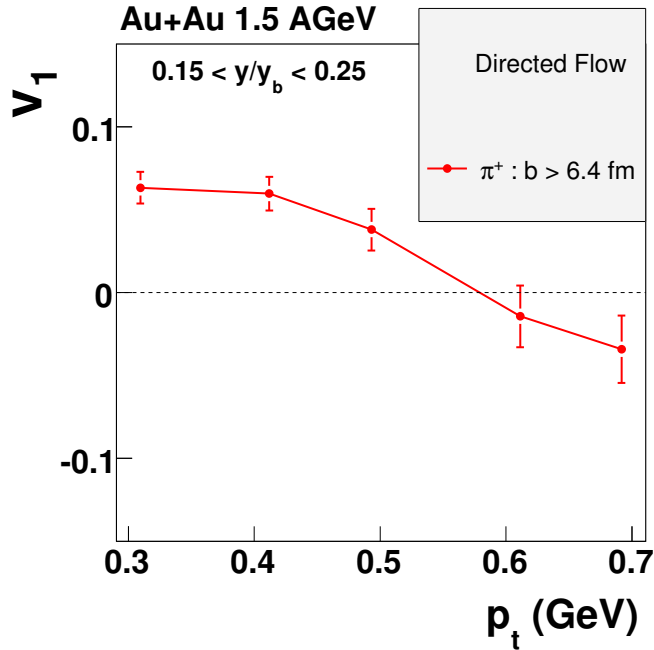


Figure 4.15: Transverse momentum dependence of the asymmetry parameters  $v_1$  for azimuthal emission pattern of  $\pi^+$  measured close to target rapidity ( $0.05 < y/y_{\text{beam}} < 0.25$ ) determined with formula 4.3 for non-central events ( $b > 6.4 \text{ fm}$ ).

### Kaons

Kaon phase space populations measured close to target rapidity are shown in fig. 4.16. Azimuthal angular emission pattern (see fig. 4.17) shows a preference of directed flow towards the target and a clear squeeze-out signal. However, the low momenta  $K^+$  mesons presented in fig. 4.18 show no preference in the emission direction, while the strong directed flow towards the target and a pronounced out-of-plane emission is to be found for the high momenta particles (right panel of figure 4.18).

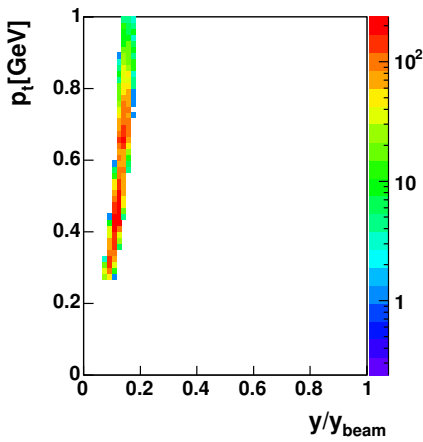


Figure 4.16: Phase space populations of  $K^+$  measured at spectrometer angle  $72\text{deg}$ .

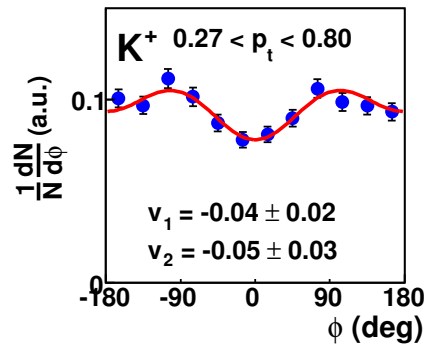


Figure 4.17: Azimuthal angular distribution of  $K^+$  mesons from Au+Au at  $1.5\text{AGeV}$ . Data selected as events with  $b > 6.4\text{fm}$ , rapidity range of  $0.05 < y/y_{\text{beam}} < 0.25$  and transverse momentum  $0.2 < p_t < 0.8$ .

Further division of the data has revealed that kaons with low transverse momenta show an enhanced emission towards the projectile and the particles with high  $p_t$  are preferentially emitted towards the target matter. The dependence of the directed flow as a function of  $p_t$  is shown in figure 4.19. The observed behavior of directed flow of kaons is very similar to the one of pions. Similarities of the observed directed flow behavior of pions and kaons may suggest that the underlying phenomenon in both cases is the shadowing mechanism. However, let us note that the re-scattering probability for pions are much larger than for kaons.

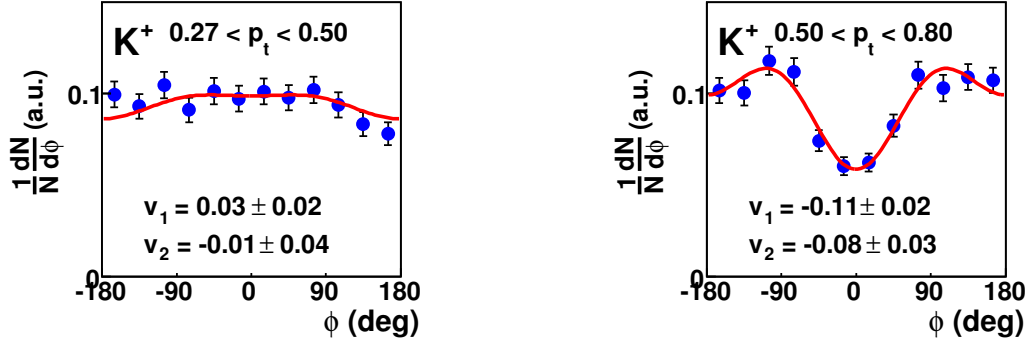


Figure 4.18: Azimuthal angular distribution of  $K^+$  mesons from Au+Au at 1.5 AGeV. Data selected as events with  $b > 6.4$  fm, rapidity range of  $0.05 < y/y_{beam} < 0.25$  and two transverse momentum  $0.2 < p_t < 0.5$  (left) and  $0.5 < p_t < 0.8$  (right).

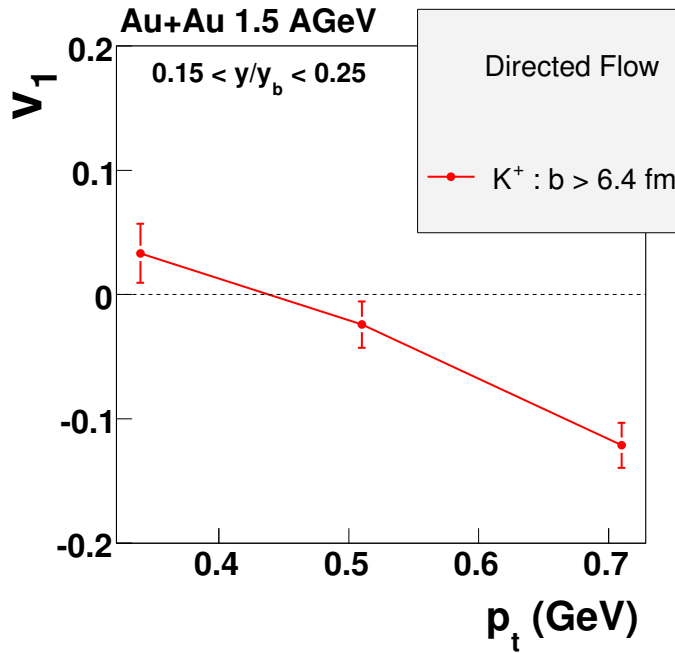


Figure 4.19: Transverse momentum dependence of the asymmetry parameters  $v_1$  for azimuthal emission pattern of  $K^+$  measured close to target rapidity ( $0.05 < y/y_{beam} < 0.25$ ) determined with formula 4.3 for non-central events ( $b > 6.4$  fm).

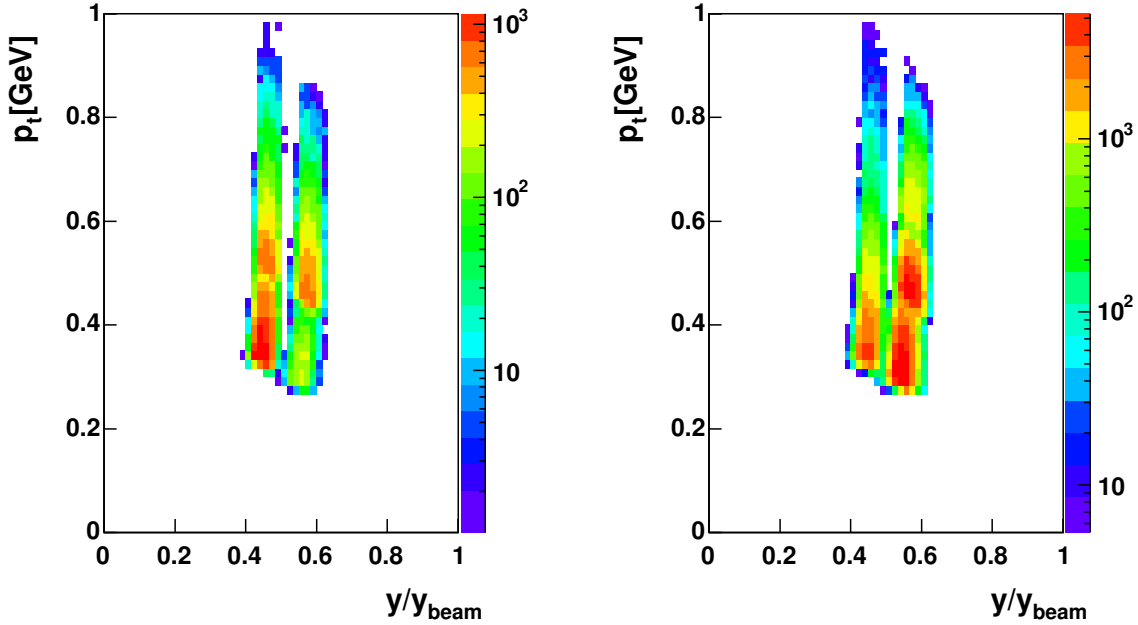


Figure 4.20: Phase space populations of  $\pi^+$  (left) and  $\pi^-$  (right) measured at spectrometer angles 40deg and 48deg.

## 4.4.2 Elliptic flow measurements

### Pions

The measured phase space populations of positively and negatively charged pions measured close to mid-rapidity ( $0.2 < y/y_{beam} < 0.6$ ) are shown in fig. 4.20. Their azimuthal angular distributions analyzed for semi-peripheral collisions ( $b > 6.4 fm$ ) are presented in figure 4.21. The anisotropy component  $v_1$  is close to zero as the directed flow of nuclear matter is expected to vanish for symmetry reasons at mid-rapidity. However, small deviations from zero appear. The measurement is not symmetric around mid-rapidity and a specific acceptance of the spectrometer also influences the result. Measurements performed at a chosen spectrometer angle are not homogeneous in the rapidity variable. Particles with low transverse momenta are measured at slightly lower rapidities than the particles with high momenta.

Figure 4.21 presents an enhanced out-of-plane emission of both  $\pi^+$  and  $\pi^-$ . The squeeze signal of pions was already found in Au+Au collisions at 1.0 AGeV [B<sup>+</sup>93, B<sup>+</sup>97] and also recent analysis of Au+Au at 1.5 AGeV and Ni+Ni at 1.93 AGeV heavy-ion experiments [För03, Uhl04] has revealed similar pattern.

Figure 4.22 shows measured pions at mid-rapidity for two different transverse momentum regions:  $0.2 < p_t < 0.5$  and  $0.5 < p_t < 0.8$ . The elliptic flow parameter shows only a slight change with increasing  $p_t$ .



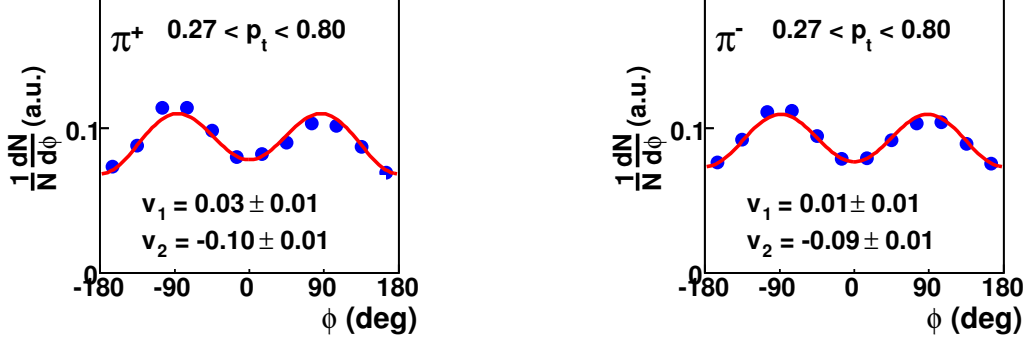


Figure 4.21: Azimuthal angular distribution of  $\pi^+$  (left) and  $\pi^-$  (right) from Au+Au at 1.5A GeV. Data selected as events with  $b > 6.4$  fm, rapidity range of  $0.2 < y/y_{beam} < 0.6$  and transverse momentum  $0.2 < p_t < 0.8$ . Lines represent fits according to formula 4.3.

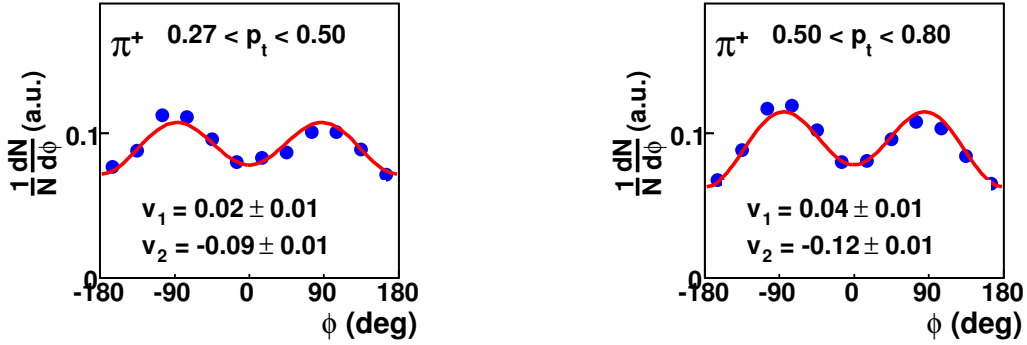


Figure 4.22: Azimuthal angular distribution of  $\pi^+$  mesons from Au+Au at 1.5A GeV for two transverse momentum bins:  $0.2 < p_t < 0.5$  (left) and  $0.5 < p_t < 0.8$  (right). Data selected as events with  $b > 6.4$  fm, rapidity range of  $0.2 < y/y_{beam} < 0.6$ . Lines represent fits according to formula 4.3.

Similar results have been obtained for  $\pi^-$ . Figure 4.23 presents azimuthal emission pattern for the two transverse momentum selections. The emission pattern has the same shape for both  $\pi^+$  and  $\pi^-$ . Further divisions of the data into several transverse momentum bins have shown very little dependence of the elliptic flow on  $p_t$  4.24.

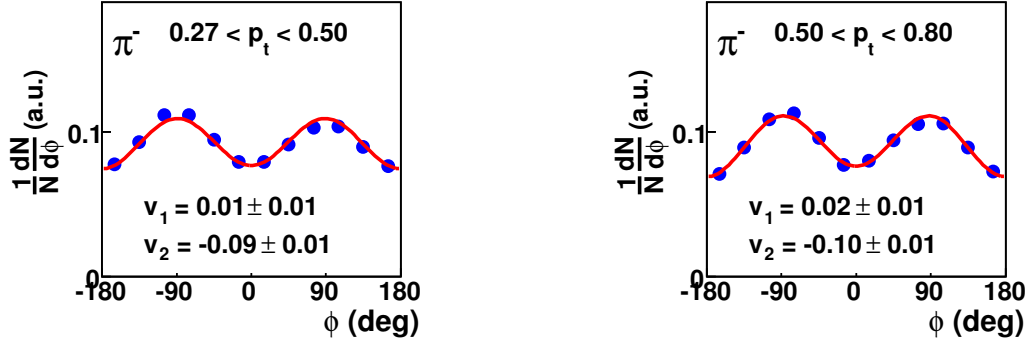


Figure 4.23: Azimuthal angular distribution of  $\pi^-$  mesons from Au+Au at 1.5 AGeV for two transverse momentum bins:  $0.2 < p_t < 0.5$  (left) and  $0.5 < p_t < 0.8$  (right). Data selected as events with  $b > 6.4$  fm, rapidity range of  $0.2 < y/y_{beam} < 0.6$ . Lines represent fits according to formula 4.3.

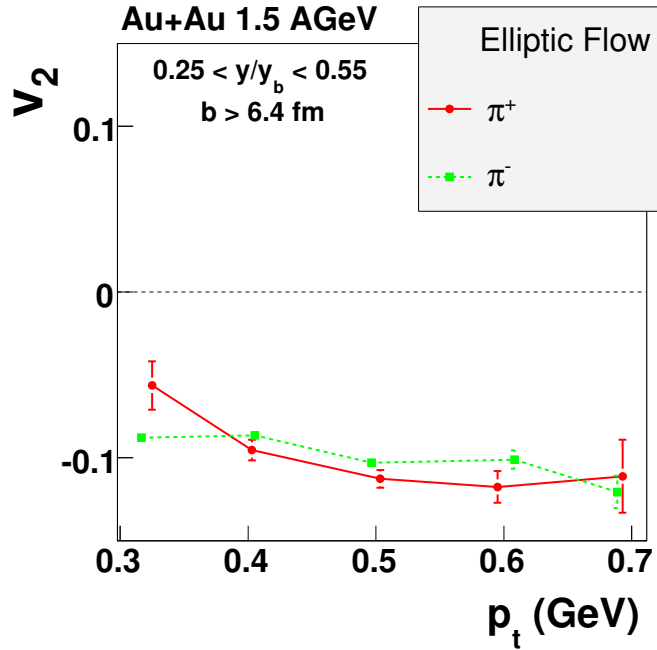


Figure 4.24: Transverse momentum dependence of the asymmetry parameter  $v_2$  for azimuthal emission pattern of  $\pi^+$  and  $\pi^-$  parametrized with formula 4.3.

### Kaons

Azimuthal angular distribution of kaons have similar characteristic as pions. Figure 4.25 shows  $K^+$  and  $K^-$  mesons measured around mid-rapidity (with spectrometer angles 40 and 48 deg) from Au+Au collisions at 1.5A GeV with impact parameters  $b > 6.4 fm$ . Both distributions show enhanced out-of-plane emission with very similar elliptic flow ( $v_2$ ) parameters.

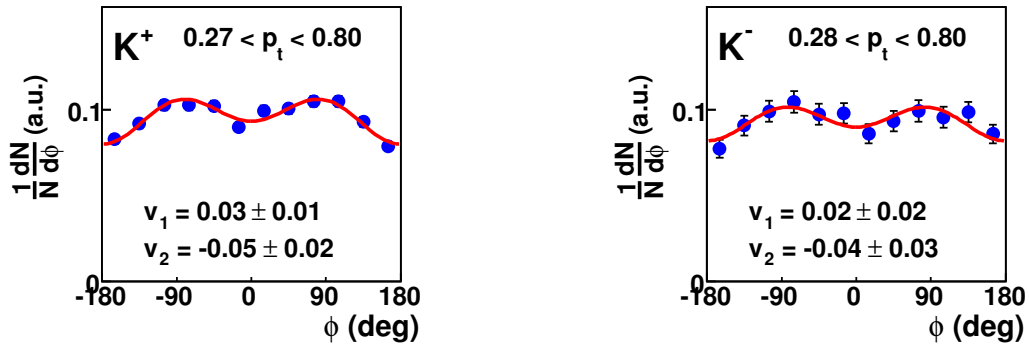


Figure 4.25: Azimuthal angular distribution of  $K^+$  (left) and  $K^-$  (right) from Au+Au at 1.5A GeV. Data selected as events with  $b > 6.4 fm$ , rapidity range of  $0.2 < y/y_{beam} < 0.6$  and transverse momentum  $0.2 < p_t < 0.8$ . Lines represent fits according to formula 4.3.

Figure 4.26 presents azimuthal emission patterns of  $K^+$  mesons for two transverse momenta sections low ( $0.2 < p_t < 0.5$ ) and high ( $0.5 < p_t < 0.8$ ). The distributions display no change of the flow components. Figure 4.30 shows that the elliptic and directed flow of  $K^+$  mesons is almost constant as a function of transverse momentum.

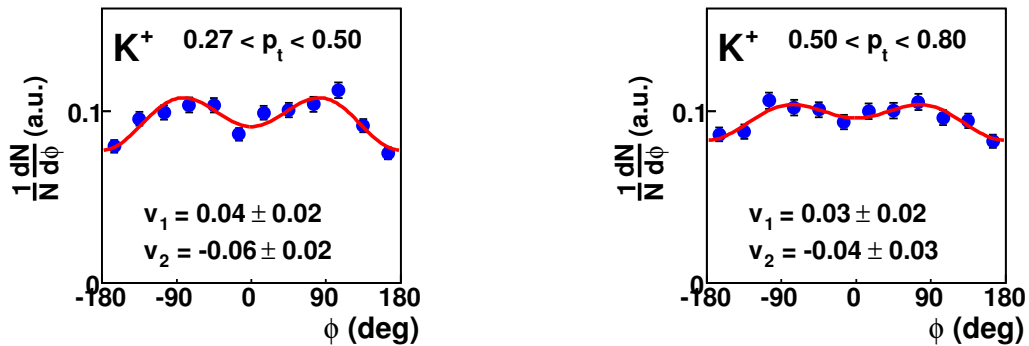


Figure 4.26: Azimuthal angular distribution of  $K^+$  mesons from Au+Au at 1.5A GeV for two transverse momentum bins:  $0.2 < p_t < 0.5$  (left) and  $0.5 < p_t < 0.8$  (right). Data selected as events with  $b > 6.4 fm$ , rapidity range of  $0.2 < y/y_{beam} < 0.6$ . Lines represent fits according to formula 4.3.

$y/y_{beam}$	$p_t(GeV)$	$v_2$
0.25 - 0.57	0.27 - 0.80	$-0.05 \pm 0.02$
0.25 - 0.48	0.27 - 0.50	$-0.06 \pm 0.02$
0.30 - 0.57	0.50 - 0.80	$-0.04 \pm 0.02$
0.25 - 0.42	0.27 - 0.35	$-0.03 \pm 0.04$
0.25 - 0.48	0.35 - 0.45	$-0.05 \pm 0.03$
0.30 - 0.50	0.45 - 0.55	$-0.05 \pm 0.03$
0.32 - 0.52	0.55 - 0.65	$-0.05 \pm 0.03$
0.35 - 0.57	0.65 - 0.75	$-0.06 \pm 0.04$

Table 4.1: Detailed measurements: elliptic flow of  $K^+$  mesons at  $36^\circ < \theta_{lab} < 52^\circ$  (see fig. 4.28 and fig. 4.29).

The situation is different for  $K^-$  mesons. Figure 4.27 presents the emission pattern of antikaons for the two different transverse momentum selections.  $K^-$  mesons with low transverse momenta ( $0.2 < p_t < 0.5$ ) exhibit almost isotropic emission (within the experimental uncertainties  $v_2 \approx 0$ ) in contrast to strong out-of-plane enhancement at high transverse momenta ( $0.5 < p_t < 0.8$ ). The data sets of  $K^+$  and  $K^-$  mesons have been subdivided into more similar acceptance transverse momentum bins. The detailed distributions are shown in fig. 4.28 and 4.29. The transverse momentum dependence of the elliptic flow for both kaon species has been gathered in figure 4.30. In addition the  $v_2$  values have been collected in table 4.1 for of  $K^+$  and 4.2 for  $K^-$  mesons. In contrast to  $K^+$  the elliptic flow of  $K^-$  mesons shows a transition from in-plane to out-of-plane emission which appears to happen at transverse momentum around  $0.4 GeV$ .

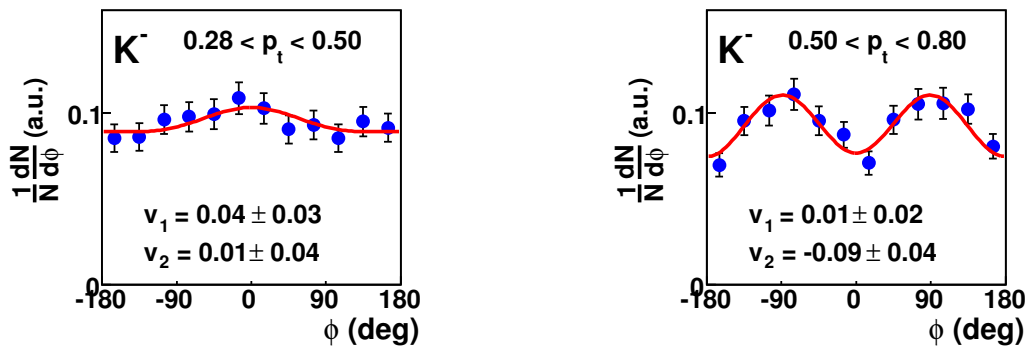


Figure 4.27: Azimuthal angular distribution of  $K^-$  mesons from Au+Au at 1.5 AGeV for two transverse momentum bins:  $0.2 < p_t < 0.5$  (left) and  $0.5 < p_t < 0.8$  (right). Data selected as events with  $b > 6.4 fm$ , rapidity range of  $0.2 < y/y_{beam} < 0.6$ . Lines represent fits according to formula 4.3.

$K^+$  mesons measured in Au+Au at 1.0 AGeV show an out-of-plane enhancement

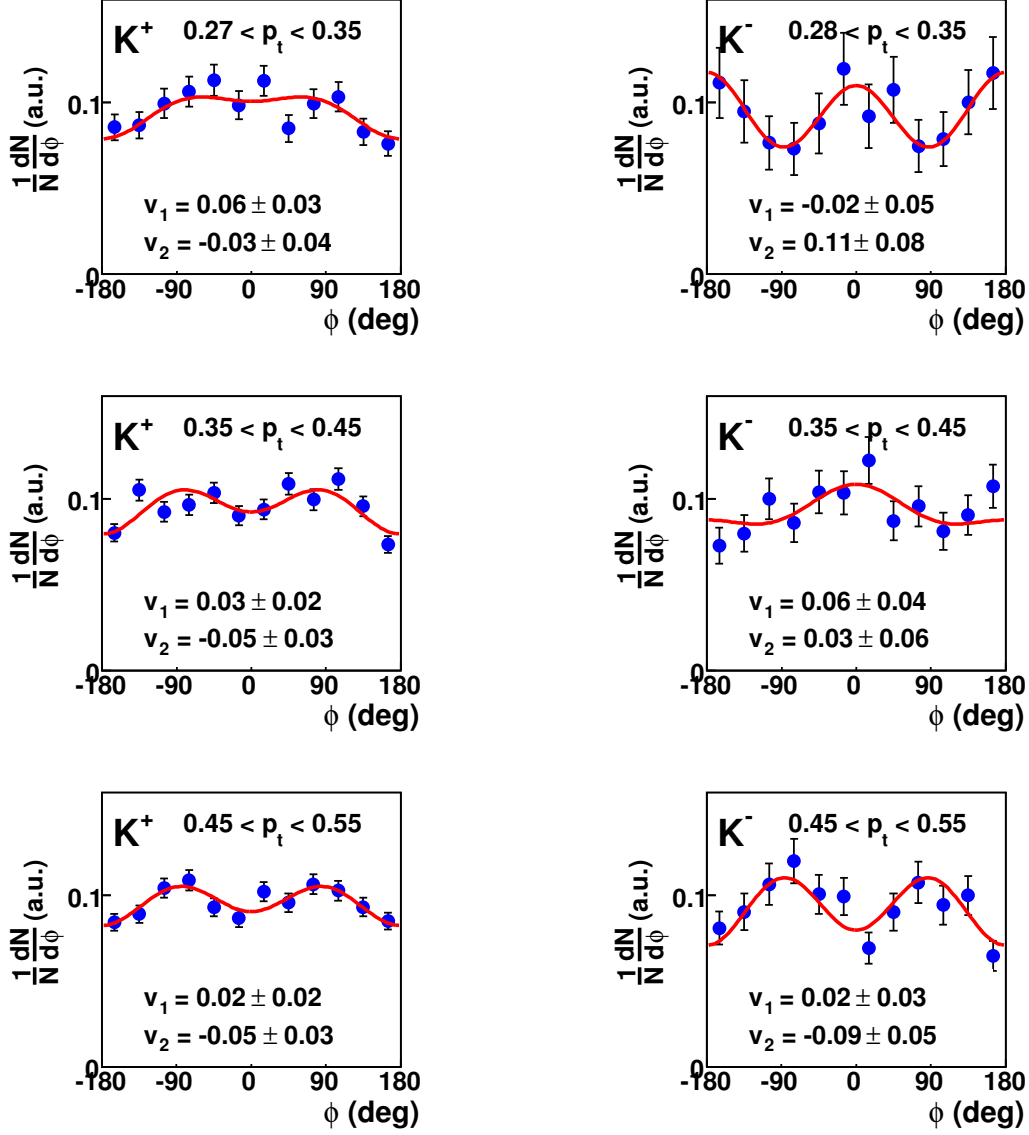


Figure 4.28: Azimuthal angular distribution of  $K^+$  mesons (left) and  $K^-$  mesons (right) from Au+Au at 1.5 AGeV for 3 lowest transverse momentum bins. Data selected as events with  $b > 6.4 fm$ , rapidity range of  $0.2 < y/y_{beam} < 0.6$ . Lines represent fits according to formula 4.3.

( $v_2 < 0$ ) in semi-peripheral collisions at mid-rapidity [S<sup>+</sup>98]. Similar observations were made with previous experiments: Au+Au at 1.5 AGeV and Ni+Ni at 1.93 AGeV [För03, U<sup>+</sup>04]. The results of the previous measurement of  $K^+$  mesons from Au+Au at 1.5 AGeV are shown in table 4.3. The  $v_2$  values are lower (stronger squeeze-out signal) and a dependence of elliptic flow on transverse momentum can be seen. Unfortunately, a complete and quantitative comparison to these results is not possible due to quite large

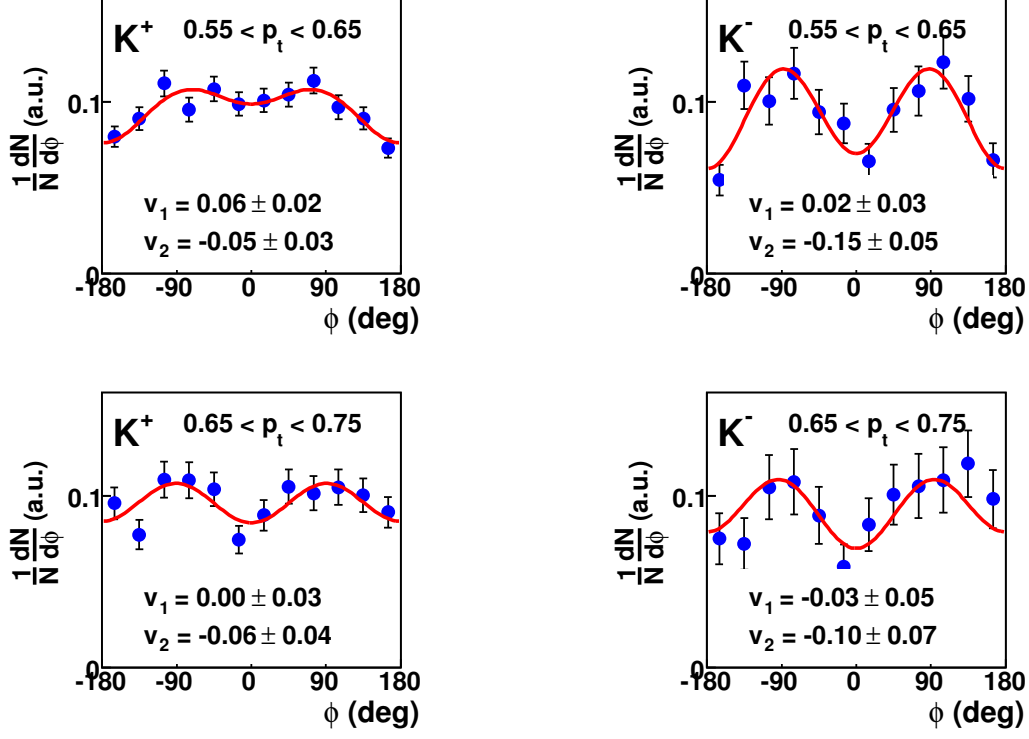


Figure 4.29: Azimuthal angular distribution of  $K^+$  mesons (left) and  $K^-$  mesons (right) from Au+Au at 1.5A GeV for 2 highest transverse momentum bins. Data selected as events with  $b > 6.4$  fm, rapidity range of  $0.2 < y/y_{beam} < 0.6$ . Lines represent fits according to formula 4.3.

$y/y_{beam}$	$p_t$ (GeV)	$v_2$
0.25 - 0.55	0.28 - 0.80	$-0.04 \pm 0.03$
0.25 - 0.50	0.28 - 0.50	$0.01 \pm 0.04$
0.32 - 0.55	0.50 - 0.80	$-0.09 \pm 0.04$
0.25 - 0.42	0.28 - 0.35	$0.11 \pm 0.08$
0.25 - 0.48	0.35 - 0.45	$0.03 \pm 0.06$
0.30 - 0.53	0.45 - 0.55	$-0.09 \pm 0.05$
0.33 - 0.55	0.55 - 0.65	$-0.15 \pm 0.05$
0.35 - 0.55	0.65 - 0.75	$-0.10 \pm 0.07$

Table 4.2: Detailed measurements: elliptic flow of  $K^-$  mesons at  $36^\circ < \theta_{lab} < 52^\circ$  (see fig. 4.28 and fig. 4.29).

differences in the rapidity regions covered by the two experiments. On the other hand, one may observe the trend of  $v_2$  as a function of  $p_t$  seen in the previous experiment is not pronounced in the new measurement.

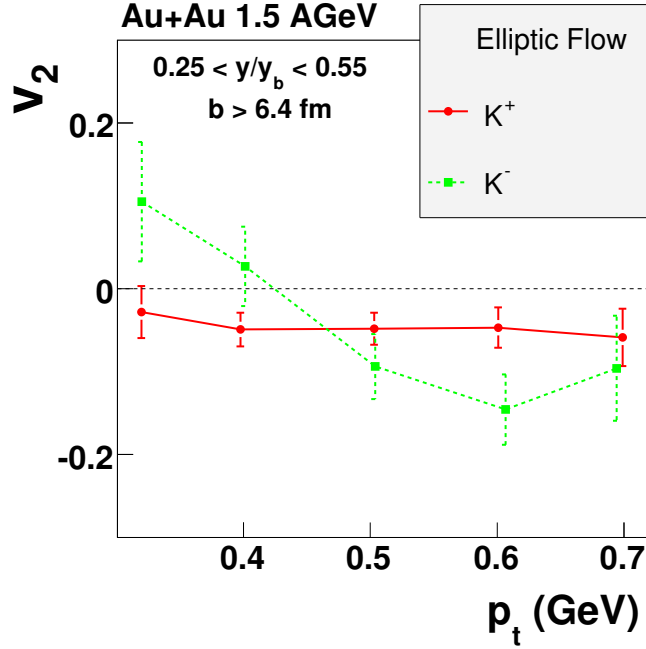


Figure 4.30: *Transverse momentum dependence of the asymmetry parameters  $v_2$  for azimuthal emission pattern of  $K^+$  and  $K^-$  mesons parametrized with formula 4.3.*

$y/y_{beam}$	$p_t(GeV)$	$v_2$
0.1 - 0.3	0.2 - 0.5	$-0.08 \pm 0.03$
0.1 - 0.3	0.5 - 0.8	$-0.1 \pm 0.06$
0.3 - 0.4	0.2 - 0.5	$-0.08 \pm 0.03$
0.3 - 0.4	0.5 - 0.8	$-0.11 \pm 0.06$
0.4 - 0.6	0.2 - 0.5	$-0.07 \pm 0.02$
0.4 - 0.6	0.5 - 0.8	$-0.15 \pm 0.03$

Table 4.3: *Previous measurements of elliptic flow of  $K^+$  mesons in Au+Au reactions at 1.5 AGeV [För03].*

Let us also note at this point that the in-plane elliptic flow pattern ( $v_2 > 0$ ) of  $K^-$  mesons has been already observed in the measurement at mid-rapidity of semi-peripheral Ni+Ni collisions at 1.93 AGeV [U<sup>+</sup>04].

# Chapter 5

## Discussion

### 5.1 Sensitivity of kaon production to in-medium effects

Theoretical models involve the existence of kaon-nucleon potentials which play an important role inside dense and hot matter - e.g. altering kaon masses[GEBT94, WKW96, KN86]. The potentials also influence the production thresholds, lowering the threshold for  $K^-$  meson production and increasing it for  $K^+$ . As a consequence, the  $K^-$  yield in heavy-ion collisions at bombarding energies below the threshold in nucleon-nucleon reactions will be enhanced significantly as compared to the case without. In contrast, the yield of  $K^+$  mesons was predicted to decrease. A comparison of the invariant production cross-sections of  $K^+$  and  $K^-$  mesons at  $\Theta_{CM} = 90^\circ$  to several microscopic transport calculations is shown in figure 5.1. In case of  $K^+$  mesons the data are unable to rule out the free case (without KN potentials) [Bra05] but they also show quite good agreement over the large range of the spectrum with the *Chiral Perturbation* model [MBSB<sup>+</sup>04, Bra05] which includes the in-medium effects. On the other hand the *G-matrix* calculations [CTBR03, Bra05] which also include the KN potentials is unable to reproduce the data. The situation is quite different for  $K^-$  mesons. Here the data are in favor of the calculations with the in-medium potentials, however it is not possible to discriminate between the models while the low energy part of the data agree with the Chiral Perturbation and the high energy part is quite well reproduced by the G-matrix model without pion dressing. The second calculation within the G-matrix approach which includes the pion dressing as well as the calculation in the free case fail to describe the data. Let us note that within the statistics of the G-matrix calculation for  $K^+$  mesons the model with pion dressing is consistent with the calculation without pion dressing.

The in-medium potentials acting differently on both kaon species have triggered investigations focused on the  $K^-/K^+$  ratio as an even more sensitive observable for the in-medium effects. The theoretical models showed that the ratio calculated as a function of kinetic energy, transverse mass or participating nucleons with the in-medium effects



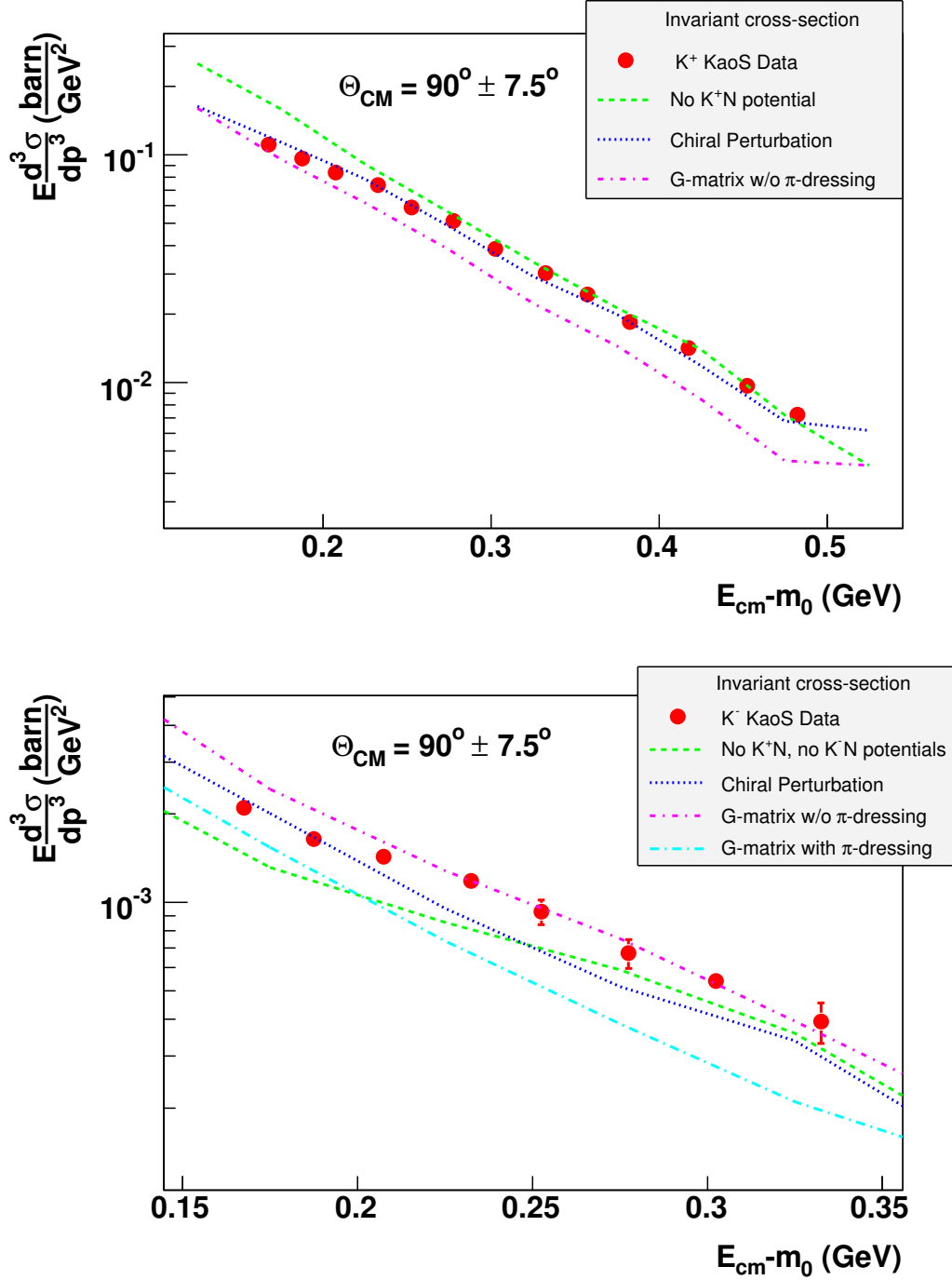


Figure 5.1: Invariant cross-sections of  $K^+$  (upper plot) and  $K^-$  mesons (lower plot) reconstructed for  $\Theta_{\text{CM}} = 90^\circ \pm 7.5^\circ$  as a function of kinetic energy in the center of mass system. Comparison of the data to the theoretical models with different approaches [Bra05] for including the in-medium effects (e.g. Chiral Perturbation [MBSB<sup>+</sup>04] and G-matrix off-shell transport calculations [CTBR03]), but also without in-medium potentials.

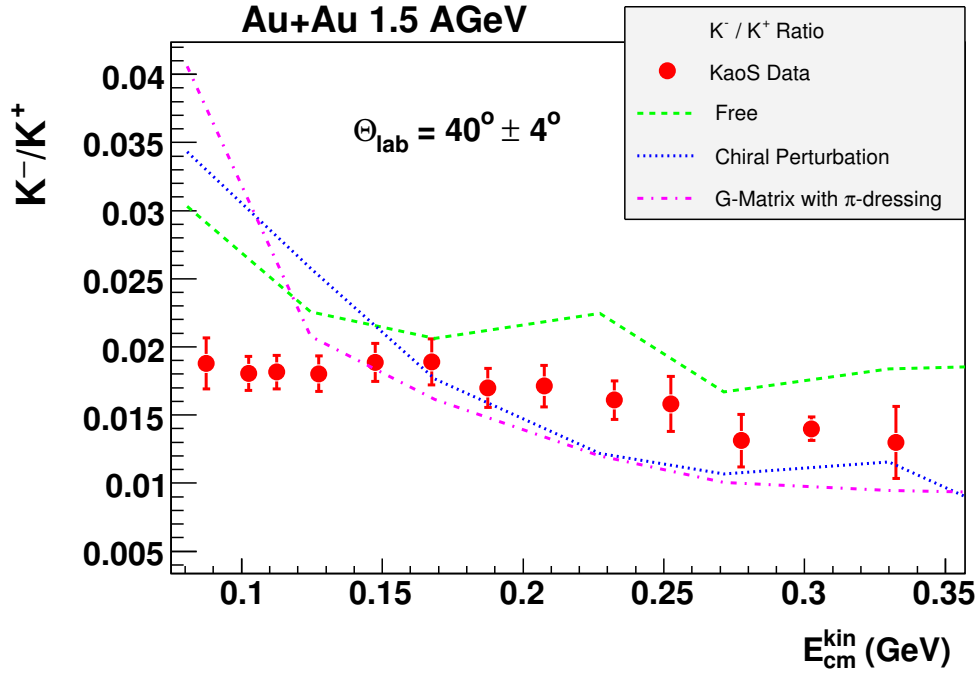


Figure 5.2:  $K^-/K^+$  ratio as a function of the kinetic energy in the center of mass system. Comparison of the data to the theoretical models with different approaches [Bra05] for including the in-medium effects (e.g. Chiral Perturbation [MBSB<sup>+</sup>04] and G-matrix off-shell transport calculations [CTBR03]), but also without in-medium potentials - “free” case.

included was different in shape and magnitude as compared to the one without taking into account potentials [Li]. Indeed the analysis of C+C collisions at 1.8 AGeV performed by KaoS collaboration has revealed a strong dependence of the  $K^-/K^+$  ratio on the kaon kinetic energy [L<sup>+</sup>99]. The  $K^-/K^+$  ratio has been reconstructed here for much heavier system - Au+Au - at 1.5 AGeV and compared to several theoretical models (see fig. 5.2). It can be seen that the data are unable to rule out any of the presented models.

## 5.2 Elliptic flow - the observations

### 5.2.1 Pions close to mid-rapidity

Azimuthal angular emission patterns of measured  $\pi^+$  and  $\pi^-$  mesons in non-central collisions close to mid-rapidity show an enhanced out-of-plane emission common to both particle species over the range studied in the experiment (see fig. 5.3). This points to a conclusion that the production and propagation of those particles are similar. In fact, the

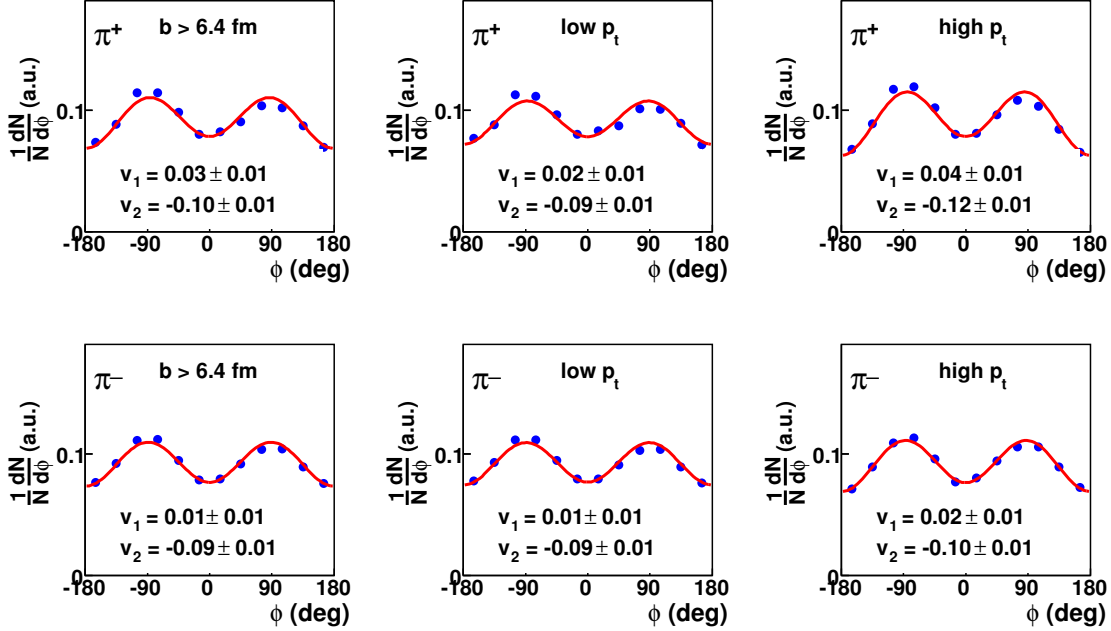


Figure 5.3: Azimuthal angular emission patterns of  $\pi^+$ ,  $\pi^-$  mesons measured in Au+Au at 1.5 AGeV collisions close to mid-rapidity in non-central events segmented in rows accordingly. Figures of a single column correspond to one of the transverse momentum sets: without  $p_t$  selection (left column), with low  $p_t$  ( $0.2 < p_t < 0.5$  - middle column) and high  $p_t$  ( $0.5 < p_t < 0.8$  - right column). Lines represent fits according to formula 4.3.

theoretical models agree with the observations [BHS93, BG95]. The enhanced out-of-plane emission is explained with help of the participant-spectator model of a heavy-ion collision. Produced pions, having a very short mean free path ( $\lambda_{\pi^\pm} \approx 0.3$  fm at  $\rho_0$ ), may easily undergo an absorption process or re-scatter in the spectator matter. The dominant processes of absorption and re-scattering of pions at the energy range discussed here are  $\pi NN \rightarrow \Delta N \rightarrow NN$  and  $\pi N \rightarrow \Delta \rightarrow \pi N$ , where  $\Delta$  is a resonance state. The production mechanism of pions at SIS energies is dominated by the decays of  $\Delta$  resonances. Additionally, large  $\pi N$  cross-section limits their in-medium mean free path. Therefore, the shadowing effect of the spectators is the reason for the bulk of pions appearing in the out-of-plane direction. This results in negative  $v_2$  values of their elliptic flow. Similar behavior has been observed in many other heavy-ion experiments with different systems and collision energies [Wag96, För03, Uhl04] (see fig. 5.4 and 5.5).

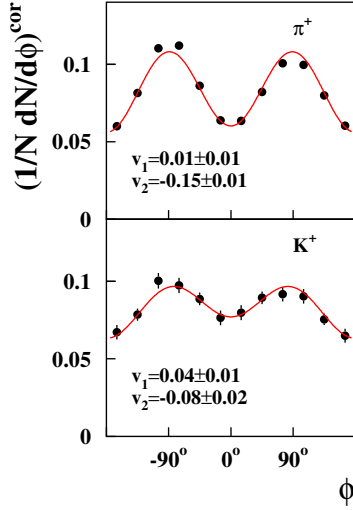


Figure 5.4: Azimuthal distribution of  $\pi^+$  and  $K^+$  mesons for semi-central Au+Au collisions at 1.5 AGeV. The data are corrected for the resolution of the reaction plane and refer to impact parameters of  $5.9\text{fm} < b < 10.2\text{fm}$ , rapidities of  $0.3 < y/y_{\text{beam}} < 0.7$  and momenta of  $0.2\text{GeV}/c < pt < 0.8\text{GeV}$ . The lines are fits with function 4.3 resulting in the values for  $v_1$  and  $v_2$  as given in the figure. Figure taken from [U<sup>+</sup>04].

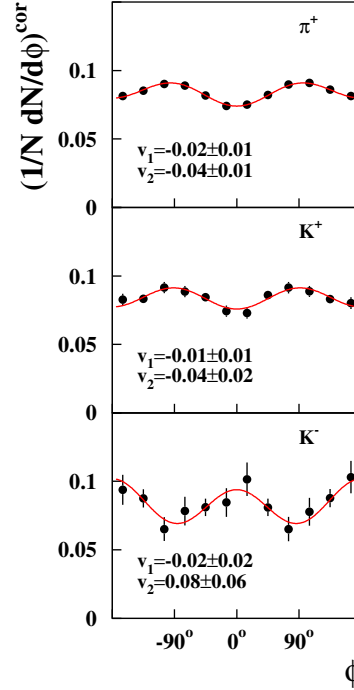


Figure 5.5: Azimuthal distribution of  $\pi^+$ ,  $K^+$  and  $K^-$  mesons for semi-central Ni+Ni collisions at 1.93 AGeV. The data are corrected for the resolution of the reaction plane and refer to impact parameters of  $3.8\text{fm} < b < 6.5\text{fm}$ , rapidities of  $0.3 < y/y_{\text{beam}} < 0.7$  and momenta of  $0.2\text{GeV}/c < pt < 0.8\text{GeV}$ . The lines are fits with function 4.3 resulting in the values for  $v_1$  and  $v_2$  as given in the figure. Figure taken from [U<sup>+</sup>04].

### 5.2.2 Kaons and antikaons close to mid-rapidity

The azimuthal angular emission patterns of  $\pi^+$  and  $\pi^-$  close to mid-rapidity in non-central collisions shows no dependence on transverse momentum of the particles (see fig. 5.3). Similar behavior is observed for kaons (see fig. 5.6). Close to mid-rapidity they show an enhanced out-of-plane emission in semi-central collisions, and their azimuthal emission patterns exhibit very little dependence on transverse momentum. The squeeze-out signal is remarkable since the probability for interaction inside the fireball is much smaller for kaons than for pions. Due to the absence of  $K^+N$  resonances kaons should leave interaction zone almost intact. Therefore, the squeeze-out of kaons cannot be justified by simple shadowing effect as compared to the pions. Out-of-plane, emission of  $K^+$  has been al-

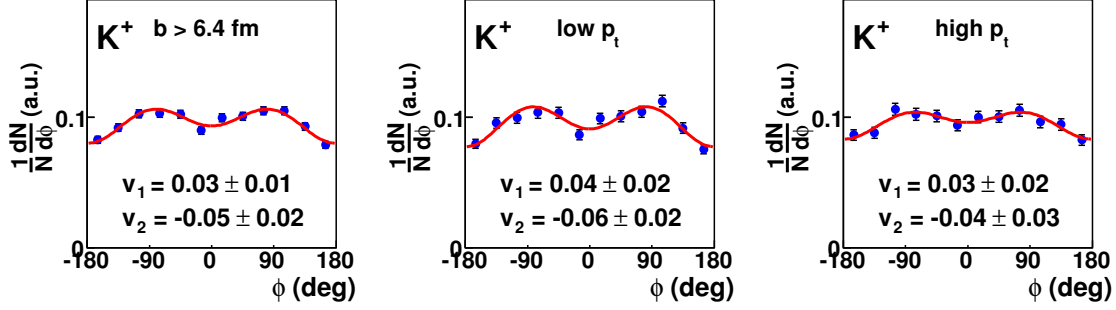


Figure 5.6: Azimuthal angular emission patterns of  $K^+$  mesons measured in Au+Au at 1.5 AGeV collisions close to mid-rapidity in non-central events. Figures from left to right correspond to one of the transverse momentum sets: without  $p_t$  selection (*left*), with low  $p_t$  ( $0.2 < p_t < 0.5$  - *middle*) and high  $p_t$  ( $0.5 < p_t < 0.8$  - *right*). Lines represent fits according to formula 4.3.

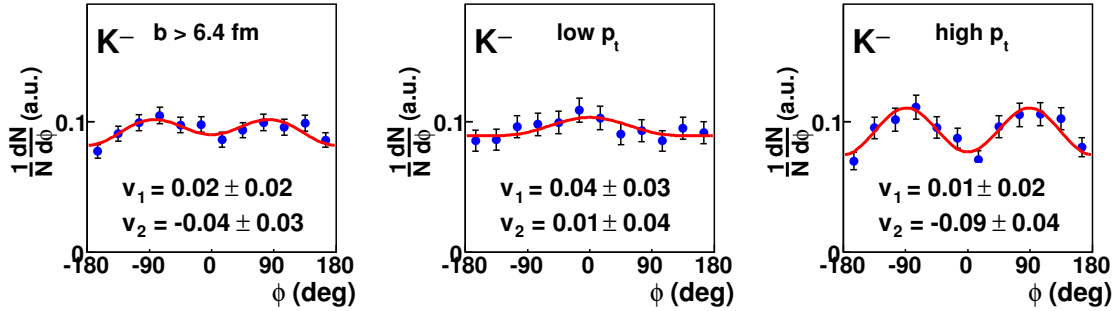


Figure 5.7: Azimuthal angular emission patterns of  $K^-$  mesons measured in Au+Au at 1.5 AGeV collisions close to mid-rapidity in non-central events. Figures from left to right correspond to one of the transverse momentum sets: without  $p_t$  selection (*left*), with low  $p_t$  ( $0.2 < p_t < 0.5$  - *middle*) and high  $p_t$  ( $0.5 < p_t < 0.8$  - *right*). Lines represent fits according to formula 4.3.

ready observed in Au+Au collisions at lower energies (1.0 AGeV) [S<sup>+</sup>98] and has been interpreted as a direct confirmation of a repulsive KN potential [WFFGB99, LKB98]. The squeeze signal for  $K^+$  mesons has also been observed in the previous experiments by the KaoS collaboration in Au+Au at 1.5 AGeV but also in Ni+Ni at 1.93 AGeV [För03, Uhl04, U<sup>+</sup>04] (see fig. 5.4 and 5.5). The  $p_t$  integrated azimuthal angular distribution of antikaons ( $K^-$ ) measured close to mid-rapidity shows similar shape as the one of  $K^+$  (see fig. 5.7). However, the analysis of the emission pattern as a function of transverse momentum reveals that  $K^-$  mesons with  $p_t < 0.5$  GeV are emitted nearly

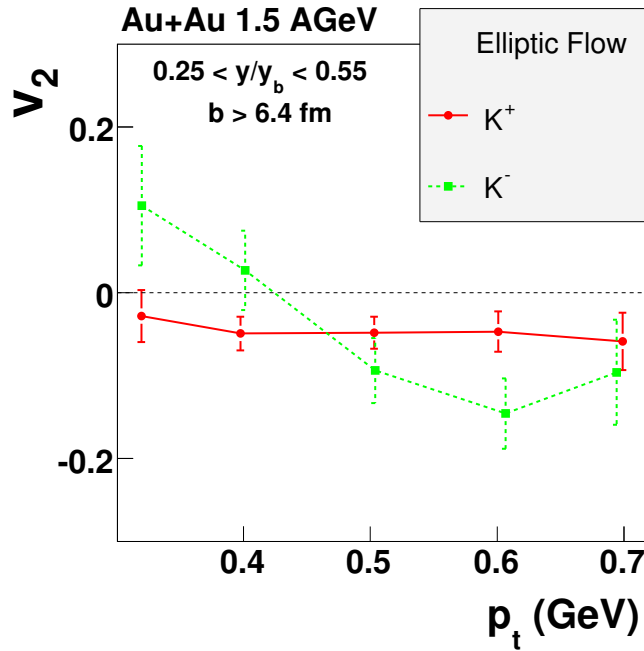


Figure 5.8: Elliptic flow of  $K^+$  and  $K^-$  mesons as a function of transverse momenta measured in Au+Au at 1.5 AGeV collisions close to mid-rapidity. Data selected for  $b > 6.4 fm$ .

isotropically whereas particles with  $p_t > 0.5$  GeV show a strong out-of-plane enhancement. Finer binning in  $p_t$  shows a strong dependence of elliptic flow of  $K^-$  mesons on transverse momentum (see fig. 5.8). The cross-over from out-of-plane at high momenta to in-plane emission at low momenta suggests a high sensitivity of their azimuthal emission pattern to the reaction dynamics. Let us note that the predictions suggested an almost isotropic emission pattern for  $K^-$  mesons as a consequence of the attractive  $K^-N$  potential balancing the large re-scattering and absorption probability of  $K^-$  mesons in the spectating fragments [WFFGB99] (see section 5.3). On the other hand, an indication of an in-plane elliptic flow of  $K^-$  mesons at mid-rapidity has been found in the Ni+Ni reactions at 1.93 AGeV by the KaoS collaboration [Uhl04, U+04] (see fig. 5.5).

### 5.3 Elliptic flow - the observable for KN potentials ?

Figure 5.9 shows a comparison of the measured azimuthal angular distributions of  $K^+$  mesons to the recent calculations [Bra05] performed with the necessary experimental acceptance cuts. The calculated emission pattern and the one obtained from the experiment

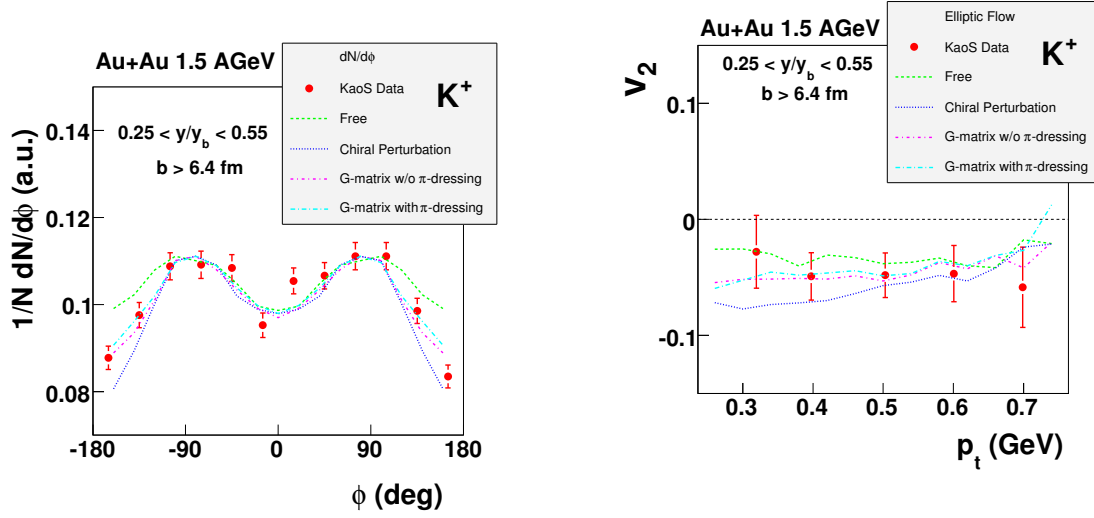


Figure 5.9: Azimuthal angular distribution of  $K^+$  (left) mesons measured close to mid-rapidity in Au+Au at 1.5 AGeV collisions compared to various transport model calculations.

Figure 5.10: Elliptic flow of  $K^+$  mesons as a function of transverse momentum. The results of the calculations [Bra05, CTBR03, MBSB<sup>+</sup>04] and data from the measurement selected for non-central Au+Au collisions at 1.5 AGeV close to mid-rapidity.

are quite consistent and it is hard to raise a strong argument in favor of any model.

The elliptic flow of kaons (fig. 5.10) as a function of their transverse momentum also shows that the influence of the potentials on kaons is not very pronounced and in fact, it is impossible to distinguish between the models within the experimental uncertainties. More to that, the calculations suggest that the out-of-plane emission of  $K^+$  can be partially explained without including the in-medium potentials. Similar observation of squeeze-out signal as an indication of kaon re-scattering have been already suggested by the IQMD model [H<sup>+</sup>98, HA04]. This was not the case in predictions for  $K^+$  mesons emitted from Au+Au at 1.0 AGeV [LKB96, LKB98, WFFGB99]. Therefore, the squeeze-out signal of  $K^+$  mesons produced in a model without in-medium potentials could be either attributed to the larger scattering probability in the densities reached in a Au+Au collision at 1.5 AGeV or to the evolution of the theoretical considerations. In addition, the comparison of the azimuthal angular distributions of  $K^+$  mesons from Ni+Ni reaction at 1.93 AGeV to the IQMD calculations [H<sup>+</sup>98, HA04] show that the squeeze-out signal can be partially reproduced by the model assuming kaon re-scattering but without including the in-medium potentials [U<sup>+</sup>04].

More discriminating information may be extracted from the azimuthal angular distribution of  $K^-$  mesons. The emission pattern presented in fig. 5.11 speaks in favor of calculations predicting out-of-plane emission of antikaons. The squeeze-out signal is in contradiction to early predictions [WFFGB99] and the *Chiral Perturbation* model. The behavior seen in the data is reproduced by G-matrix as well as the *free case* (e.g. without

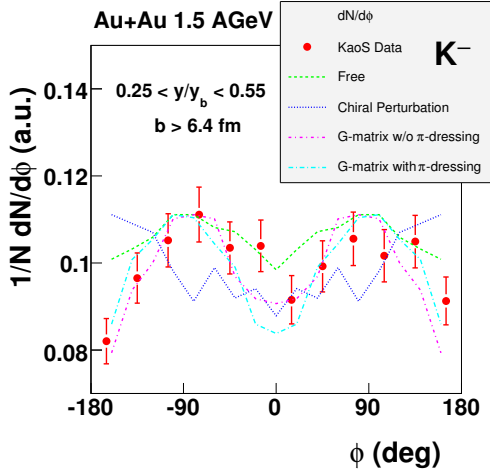


Figure 5.11: Azimuthal angular distribution of  $K^-$  mesons measured close to mid-rapidity in Au+Au at 1.5 AGeV collisions compared to various transport model calculations.

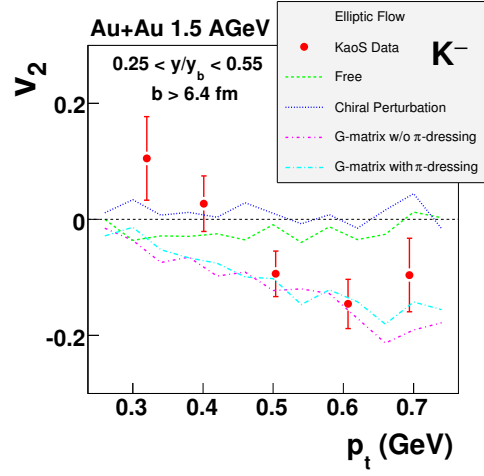


Figure 5.12: Elliptic flow of  $K^-$  mesons as a function of transverse momentum. The results of the calculations [Bra05, CTBR03, MBSB<sup>+</sup>04] and data from the measurement selected for non-central Au+Au collisions at 1.5 AGeV close to mid-rapidity.

KN potentials) which also shows moderate out-of-plane emission.

Figure 5.12 shows a comparison of the measured elliptic flow of  $K^-$  mesons to the calculations as a function of transverse momentum. It is evident that the data in the high  $p_t$  region prefer the calculations which include the in-medium effects with the G-matrix off-shell transport approach. The chiral perturbation model fails to reproduce elliptic flow of antikaons over the range of high transverse momentum. On the other hand, the Chiral Perturbation model as well as the calculations without in-medium potentials are somewhat closer to reproduce the low  $p_t$  data, where the in-plane flow is observed. However, the cross-over from in-plane to out-of-plane emission with increasing transverse antikaon momentum is not seen in any of the models.

## 5.4 What do we actually observe ?

In order to explain the emission of  $K^-$  mesons - out-of-plane at high  $p_t$  and in-plane at low  $p_t$  - it is worthwhile to compare the time evolution of the kaon and antikaon number in different transport calculations. Figure 5.13 shows the production rates of  $K^+$  and  $K^-$  mesons as a function of the freeze-out time. It is clearly seen that all of the models agree on almost simultaneous emission of  $K^+$  while only the two variations of the G-matrix



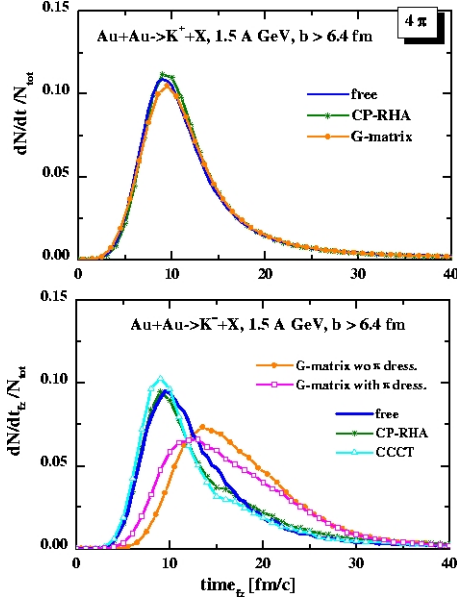


Figure 5.13: *Production rates of  $K^+$  (upper panel) and  $K^-$  (lower) as functions of collision time according to different theoretical models.*

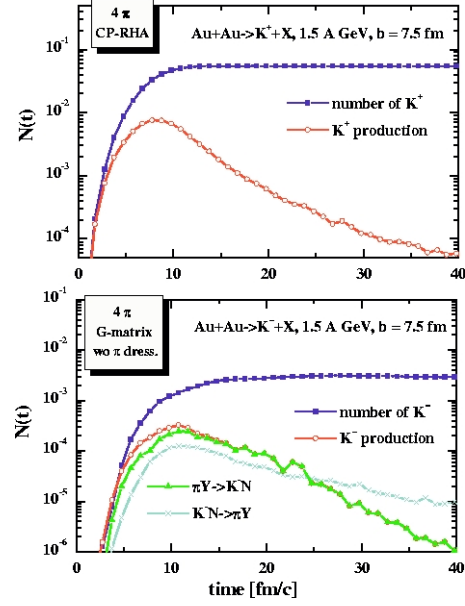


Figure 5.14: *Number of  $K^+$  (upper panel) and  $K^-$  (lower) as functions of collision time according to selected theoretical models.*

model (with- and without pion dressing) significantly modify the emission time of the  $K^-$  mesons. The calculations show that the production of  $K^-$  mesons within the G-matrix model is dominated by the strangeness-exchange ( $\pi Y \leftrightarrow K^- N$ , with  $Y = \Lambda, \Sigma$ ) reaction (see fig. 5.14). The differences between the models in emission time of  $K^-$  mesons leads to the conclusion that it is the strangeness-exchange ( $K^-$  production-absorption) mechanism responsible for retarding antikaon emission. Furthermore, the evolution of the elliptic flow studied in different models and decomposed into selected channel input indicates (see fig. 5.15) that  $K^-$  mesons produced via  $\pi Y$  reaction are responsible for the large negative  $v_2$  values. Such evolution of the elliptic flow combined with the observation that the models based on the G-matrix reproduce the high  $p_t$  part of the elliptic flow leads to the conclusion that the strangeness-exchange and consequently, the emission time plays a crucial role in shaping azimuthal angular emission pattern of  $K^-$  mesons. The late emission also implies that the freeze-out of antikaons should take place later in time and, in fact, this has been found. The inverse slopes of the invariant cross-section presented in section 4.3 are significantly smaller for  $K^-$  than for  $K^+$ . Furthermore, the centrality dependent analysis of the inverse slope parameters of the spectra measured during previous (Ni+Ni at 1.93 A GeV, and Au+Au at 1.5 A GeV) experiments performed by KaoS collaboration have revealed that the inverse slope parameters of the  $K^-$  are about 20 MeV smaller than the ones for  $K^+$  [För03, Uhl04] which indeed, suggests that antikaons have different freeze-out conditions than kaons. In addition, recently, a slight in-plane flow of  $K^-$  observed from Ni+Ni reactions at 1.93 A GeV has been observed

and compared to the IQMD model calculations [U<sup>+</sup>04]. The authors explain the effect with a scenario where the strangeness-exchange channel plays a crucial role in delaying the antikaon emission from the fireball, and thus minimizing their interaction with the spectators (see also [F<sup>+</sup>03, HOA03]). Different emission times of  $K^+$  and  $K^-$  mesons are also confirmed in measured polar angular distributions. A forward-backward enhancement of  $K^+$  mesons in polar angular distributions independent of centrality was observed, whereas the  $K^-$  mesons seem to lose their memory of the beam direction in near central collisions [För03, M<sup>+</sup>00].

Finally, let us note that the density of a heavy-ion collision is very strongly correlated

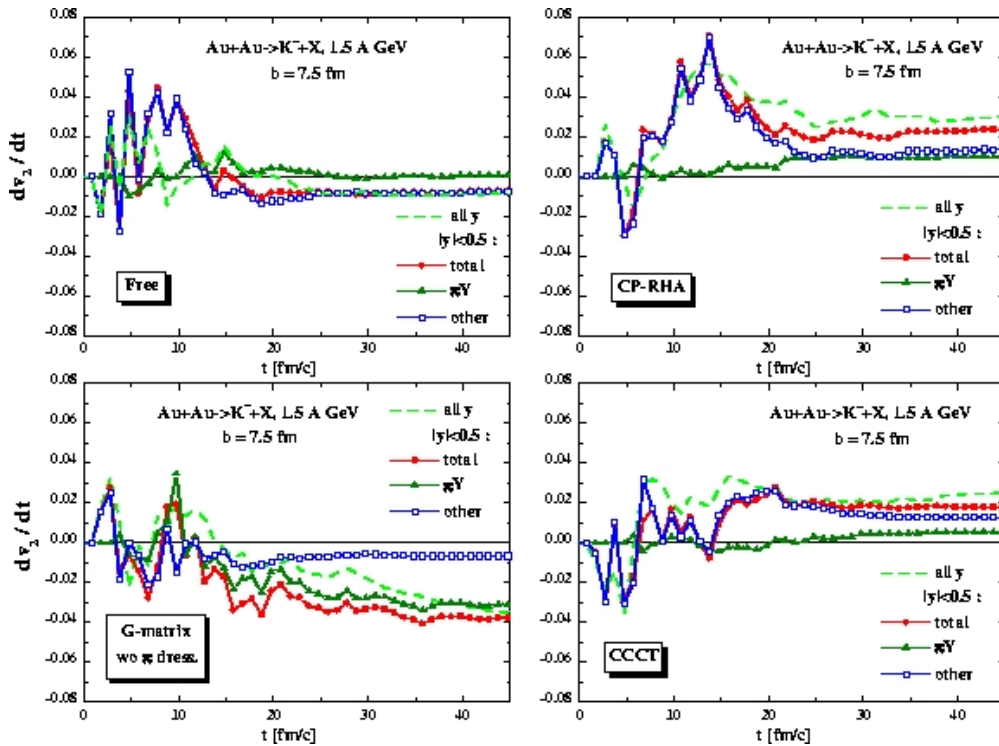


Figure 5.15: Elliptic flow evolution of  $K^-$  mesons in different models. Additionally for calculations close to mid-rapidity the total elliptic flow has been decomposed into part associated with the strangeness-exchange production channel and all other. Calculations for semi-central Au+Au collisions at 1.5 A GeV [Bra05].

with the time of the collision. Therefore, due to the different emission times, kaons are produced predominately in the most dense phase of the collision while for the  $K^-$ , produced via strangeness-exchange reaction, the maximum production rate is reached when the system already starts to expand [HA04]. Consequently, if the production time of  $K^+$  mesons is different than for  $K^-$  mesons and the densities of the nuclear medium are different, then the influence of the potentials has to be revised accordingly. For a given maximum density  $\rho_{max}$  reached in a collision,  $K^+$  mesons experience a repulsive KN potential and the strength of which is given by the densities  $\rho_{K^+} \approx \rho_{max}$ , while the

$K^-$  mesons experience an attractive KN potential corresponding to much lower densities  $\rho_{K^-} \ll \rho_{max}$ . Thus, the strength of the attractive KN potential may be, in fact, not large enough to sufficiently manifest its influence on the azimuthal emission pattern of  $K^-$  and the observation presented in fig. 5.8 is mostly a consequence of the production mechanism of  $K^-$  and their late emission times. Therefore, antikaons with high  $p_t$  are emitted early enough to be reabsorbed in the spectators. On the other hand, one may speculate that the late  $K^-$  mesons, with low  $p_t$ , are emitted from the surface of the almond shaped fireball and therefore are preferentially directed into the reaction plane by the still existing density gradient. At those late times there are no spectators to absorb, scatter them and shadow their path.

# Chapter 6

## Summary and outlook

The measurements presented in this work confirm previous observations on the collective flow of particles in heavy-ion collisions. The azimuthal angular distribution of positively charged pions measured close to target rapidity shows high sensitivity to the emission time of the particles. Similar behavior has been also observed for  $K^+$  mesons. On the other hand the azimuthal emission patterns of kaons obtained close to mid-rapidity have shown an out-of-plane elliptic flow being almost independent of the transverse momentum of the particles. However, for  $K^-$  mesons it has been found that the particles with low  $p_t$  show an enhanced in-plane emission whereas the squeeze signal has been observed for the high  $p_t$  antikaons.

The comparison of the results to the transport calculations has revealed that the out-of-plane emission of  $K^+$  mesons can be, into large extent, attributed to the re-scattering [H<sup>+</sup>98, HA04, Bra05]. On the other hand, the out-of-plane emission of the high transverse momentum  $K^-$  mesons has been reproduced by the G-matrix calculations which take into account the in-medium potentials [CTBR03, Bra05]. However, it has been also shown that the production mechanism of  $K^-$  mesons (e.g. *strangeness-exchange*) plays here the crucial role. In addition, let us note, that the comparison of the production cross-sections of kaons and antikaons to the models fits to a consistent picture, but still, none of the presented models is able to reproduce neither the  $v_2$  signal of  $K^-$  mesons over the complete range of the  $p_t$  explored in the experiment nor the measured production cross-section as a function of energy.

Therefore, it seems, that there is still some room for further studies and developments in the microscopic models. With the help of calculations one should be able to disentangle between the influence of the  $KN$  in-medium potentials and the consequences of the production mechanism. Of course, additional measurements of the azimuthal emission pattern of  $K^-$  mesons from heavy-ion collisions at target rapidities, for example, could also be a valuable source of constraints to the models. Finally, the goal is to have a definite answer on the question of interplay between particle emission times, nuclear density at the time of particle creation (with a given production mechanism) and kaon-nucleon potentials influencing the azimuthal angular distributions.



# Appendix A

## Obtaining double differential cross-sections

Double differential production cross-sections for pions and kaons have been reconstructed. The cross-section defined as

$$\frac{d\sigma}{dp_{lab}d\Omega_{lab}} = \frac{M_t}{d_t \rho_t N_A} \cdot \frac{1}{N_{beam}} \cdot \frac{1}{f_{acc}(p_{lab}, \Omega_{lab})} \cdot \frac{1}{\epsilon(p_{lab})} \cdot N(p_{lab}, \Omega_{lab}) \quad (\text{A.1})$$

$M_t$	- molar mass of the target material	$N_{beam}$	- number of the beam particles
$d_t$	- thickness of the target	$f_{Acc}$	- acceptance correction
$\rho_t$	- density of the target material	$\epsilon(p_{lab})$	- total efficiency
$N_A$	- Avogadro constant	$N(p_{lab}, \Omega_{lab})$	- number of identified particles

demands an estimation of the detector efficiencies and acceptances which differ from the unity. The total efficiency  $\epsilon(p_{lab})$  of the detector setup and measurement consists of:

$$\epsilon(p_{lab}) = \epsilon_{MWPC} \cdot \epsilon_{dead} \cdot \epsilon_{cut}^{total}(p_{lab}) \cdot \epsilon_{trig}(p_{lab}) \cdot \epsilon_{track}. \quad (\text{A.2})$$

$\epsilon_{MWPC}$	- detector efficiencies	$\epsilon_{dead}$	- DAQ dead time correction
$\epsilon_{cut}^{total}(p_{lab})$	- total cut efficiency	$\epsilon_{trig}(p_{lab})$	- trigger efficiency
$\epsilon_{track}$	- tracking efficiency		

Furthermore, the normalization to the beam current  $N_{beam}$  is necessary. The following sections briefly describe the procedures of obtaining these factors.

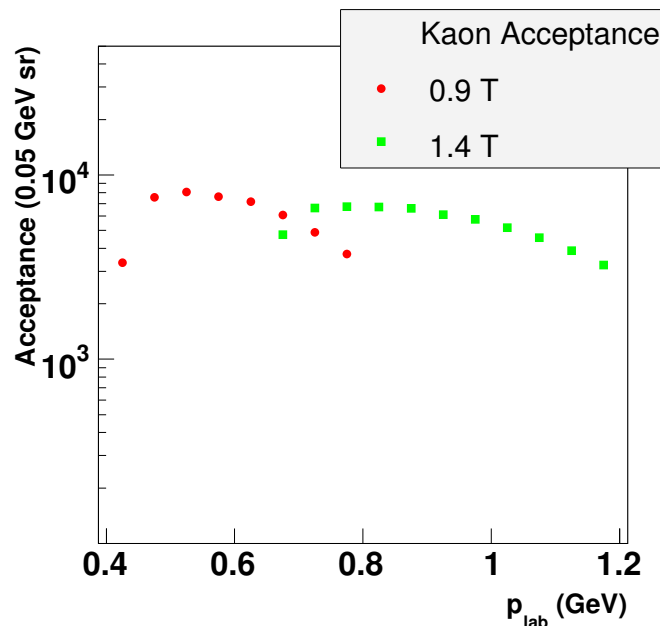


Figure A.1: *The acceptance and the in-flight decay corrections for Kaons as a function of the kaon momentum in the laboratory frame for the three measured magnetic field settings of the dipole magnet.*

## A.1 Acceptance corrections

The geometrical acceptance of the spectrometer and the kaon decay in flight was determined by the Monte Carlo simulations using the simulation package GEANT[Gro93]. Resulting values have been gathered and shown in the fig.A.1.

## A.2 Trigger efficiencies

In order to investigate the trigger efficiency for kaons (TOF trigger setting), dedicated measurements have been performed. Setting the dipole magnetic field at the certain values gives possibility to measure pions or protons falling into the time of flight window of kaons (e.g. the same velocity as kaons - so called pseudo-kaons measurement with the spectrometer trigger engaged). Trigger efficiency then is the ratio between particles detected (in the specific mass window -  $3\sigma$  around the Kaon peak) with the TOF trigger bit set ( $N^{TOF}$ ) and the total number of particles detected (falling into the same mass peak) in this measurement ( $N^{all}$ ):

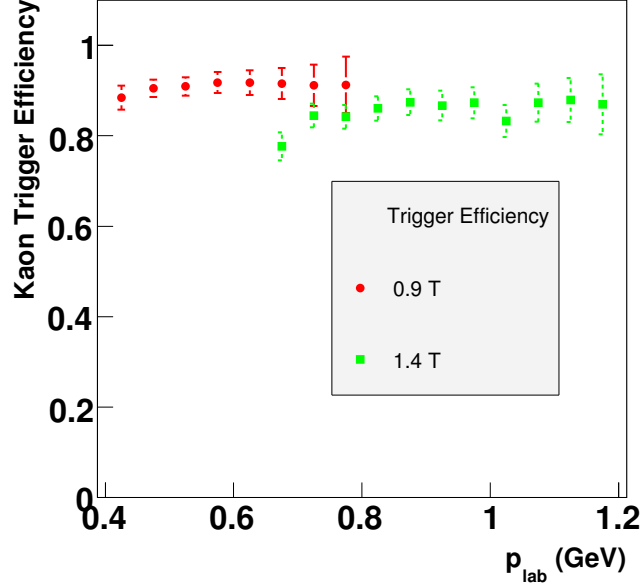


Figure A.2: *Trigger efficiency for the TOF setting as a function of the kaon momentum in the laboratory frame for the three measured magnetic field settings of the dipole magnet.*

$$\epsilon_{trigg}(p_{lab}) = \frac{N^{TOF}(p_{lab})}{N^{all}(p_{lab})}. \quad (\text{A.3})$$

Trigger efficiencies have been estimated for each of the magnetic field settings of the dipole magnet. In addition, the efficiency for the 1.4T setting includes also the Cherenkov detector efficiency (see fig.A.2). For the pions, the trigger efficiency can be assumed to be 100% as the time of flight window is open wide enough to accept all of the particles.

### A.3 MWPC's efficiencies

The chambers' efficiencies  $\epsilon_{MWPC}$  are calculated as the ratios between detected particles (of the same species) in the D-detector and L-chamber:

$$\epsilon_{MWPC-L}^{\pi,p} = \frac{N_{MWPC-L}^{\pi,p}}{N_{D-det}^{\pi,p}}. \quad (\text{A.4})$$

For the M and N-chamber it is the ratio of the relative hit counts:



$$\epsilon_{MWPC-M,N}^{\pi,p} = \frac{N_{MWPC-M,N}^{\pi,p}}{N_{MWPC-N,M}^{\pi,p}}. \quad (\text{A.5})$$

The efficiency of the MWPC's for the identification of minimum ionizing particles is measured to be better than 95%.

## A.4 Tracking efficiencies

The efficiency of the tracking procedure  $\epsilon_{track}$  has been calculated using a Monte-Carlo simulation within the GEANT[Gro93] package. The simulation produces sets of data with various numbers of the track multiplicities and additionally with some underground contamination within the multi-wire chambers. The tracking efficiency is calculated for all of those combinations. Finally, for each of the acquired files a set of trajectories with the background hits is generated providing the input for the tracking efficiency calculation. Detail description of the tracking efficiency estimation can be found in [Stu01].

## A.5 Cut efficiencies

The calculation of the cut efficiencies requires reliable kaon number per momentum bin estimation, both before ( $N_{no\_cuts}^K(pbin)$ ) and after the cut has been applied ( $N_{cut}^K(pbin)$ ). The integration of the kaon yield without any cut applied is strongly biased by the shape of the background and may introduce large systematic uncertainties also due to low statistics. Therefore, the cut efficiencies have been estimated with background free and large statistic GEANT-generated tracks for the geometrical cuts and, in case of TOF cut, pseudo-kaons measurements (pions or protons with the TOF of kaons) where used. The efficiencies have been estimated for each magnetic field setting separately.

The efficiency of the geometrical cut (in x-axis of L-chamber and in y-axis of N-chamber) has been calculated as:

$$\epsilon_{cut}^{geom}(pbin) = \epsilon_{cut}^{Lx} \cdot \epsilon_{cut}^{Ny}, \quad (\text{A.6})$$

where

$$\epsilon_{cut}^{Lx} = \frac{N_{Lx\_cut}^{K-GEANT}(pbin)}{N_{no\_cuts}^{K-GEANT}(pbin)}, \quad \epsilon_{cut}^{Ny} = \frac{N_{Ny\_cut}^{K-GEANT}(pbin)}{N_{no\_cuts}^{K-GEANT}(pbin)}. \quad (\text{A.7})$$

The TOF cut efficiency has been estimated with the measurements of particles (pions or protons) acquired with the magnetic field set such that their time of flight corresponds to the TOF of kaons.

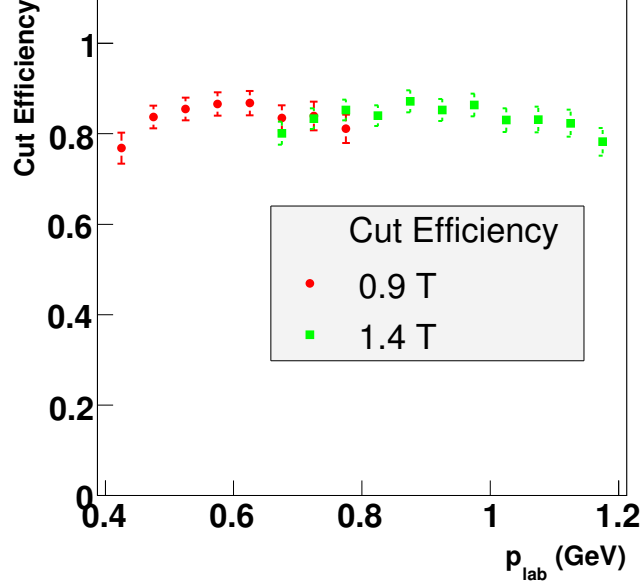


Figure A.3: Total efficiency of the  $3\sigma$  cut for the two magnetic field settings

$$\epsilon_{cut}^{beta}(p_{bin}) = \frac{N_{all\_cuts}^{Pseudo-K}(p_{bin})}{N_{geom\_cut}^{Pseudo-K}(p_{bin})}. \quad (\text{A.8})$$

The total cut efficiency ( $3\sigma$ )

$$\epsilon_{cut}^{total}(p_{bin}) = \epsilon_{cut}^{geom}(p_{bin}) \cdot \epsilon_{cut}^{beta}(p_{bin}) \quad (\text{A.9})$$

is presented for the 72 degrees measurement in fig. A.3.

## A.6 Dead time correction

In order to compensate for the dead time of the hardware one takes the scaler values of the trigger rates. Ratio of the trigger after inhibit to the value of the same trigger before inhibit estimates the dead time

$$\tau_{dead} = \frac{N_{trig}^{after\_inhibit}}{N_{trig}^{before\_inhibit}} \quad (\text{A.10})$$

of the data acquisition. Therefore the correction factor is

$$\epsilon_{dead} = 1 - \tau_{dead}. \quad (\text{A.11})$$

## A.7 The beam normalization

With use of the detectors described in the chapter 2.5, the normalization of the beam current is possible. In order to estimate the beam intensity special measurements have been performed. The first measurement estimates the number of the beam particles with a plastic scintillator ( $B1$ ) moved to the target position. Additionally in order to reduce the amount of non-correlated particles with the beam detected by the two plastic telescopes ( $Moni_{left}$  and  $Moni_{right}$ ) a coincidence between the two groups of the detectors has been set. The rates have been recorded with help of the scaler counters. Following this procedure, a scaling factor

$$F_{beam} = \frac{N_{B1}}{0.5 \cdot (N_{Moni_{left}} + N_{Moni_{right}}) - N_{bg}} \quad (\text{A.12})$$

has been obtained.

In order to estimate the correlated background particles rate ( $N_{bg}$ ) resulting from the interaction of the beam with the plastic scintillator itself additional measurements have been performed - with and without a target. The number of the background particles  $N_{bg}$  is calculated using these measurements by the formula

$$N_{bg} = 0.5 \cdot (N_{Moni_{left}}^{NoTarget} + N_{Moni_{right}}^{NoTarget}) \cdot \frac{N_{B1}^{WithTarget}}{N_{B1}^{WithTarget}} \quad (\text{A.13})$$

As a result of the above procedure the number of the beam particles  $N_{beam}$  for each of the acquired files can be obtained:

$$N_{beam} = F_{beam} \cdot 0.5 \cdot (N_{Moni_{left}} + N_{Moni_{right}}). \quad (\text{A.14})$$

## A.8 Systematic error estimations

The sources of the momentum and laboratory angle independent systematic errors and their estimates are to be taken into account as follows:

- trigger efficiency estimation - 4%
- MWPC's efficiencies estimation - 4%

- tracking efficiency - 4%
- cut efficiencies (only in the case of kaons) - 5%
- dead time correction - 5%
- beam intensity estimation - 5%
- acceptance correction (GEANT simulation) - 4%

As these errors are not independent, the total systematic error has been calculated as the square root of the sum of squares of individual contributions. Therefore, the total systematic error is to be taken as 12% for kaons and 11% for pions.

# Appendix B

## Invariant cross-section

With help of the Lorentz invariant phase-space element  $\frac{d^3p}{E}$ , one defines the invariant cross-section as

$$\sigma_{inv} = E \frac{d^3\sigma}{dp^3}. \quad (\text{B.1})$$

The element  $d^3p$  can be transformed as

$$d^3p = dp_x dp_y dp_z = p^2 dp \sin \theta d\theta d\phi = p^2 dp d\Omega. \quad (\text{B.2})$$

From the relation

$$E = \sqrt{p^2 + m^2} \quad (\text{B.3})$$

one derives identity

$$p dp = E dE. \quad (\text{B.4})$$

The invariant cross-section can be rewritten as

$$\sigma_{inv} = E \frac{d^3\sigma}{dp^3} = E \frac{1}{p^2} \frac{d^2\sigma}{dp d\Omega} = E \frac{1}{pE} \frac{d^2\sigma}{dE d\Omega} = \frac{1}{p} \frac{d^2\sigma}{dE d\Omega}. \quad (\text{B.5})$$

The invariance under the Lorentz transformations yields

$$\left( E \frac{d^3\sigma}{dp^3} \right)_{cm} = \left( \frac{1}{p} \frac{d^2\sigma}{dE d\Omega} \right)_{cm} = \left( \frac{1}{p} \frac{d^2\sigma}{dE d\Omega} \right)_{lab} = \left( \frac{E_{lab}}{p_{lab}^2} \frac{dp}{d\Omega} \right)_{lab}. \quad (\text{B.6})$$

# Bibliography

- [A<sup>+</sup>01] A. Andronic et al. Differential directed flow in Au + Au collisions. *Phys. Rev.*, C64:041604, 2001. 46
- [And05] A. Andronic. Private communication, 2005. 46
- [B<sup>+</sup>93] D. Brill et al. Azimuthally anisotropic emission of pions in symmetric heavy ion collisions. *Phys. Rev. Lett.*, 71:336–339, 1993. 7, 51
- [B<sup>+</sup>96] D. Brill et al. Studies of the out-of-plane emission of protons and light fragments in symmetric heavy-ion collisions. *Z. Phys.*, A355:61, 1996. 45
- [B<sup>+</sup>97] D. Brill et al. Studies of the out-of-plane emission of pions in symmetric heavy ion collisions. *Z. Phys.*, A357:207–213, 1997. 7, 51
- [B<sup>+</sup>98] S. A. Bass et al. Microscopic models for ultrarelativistic heavy ion collisions. *Prog. Part. Nucl. Phys.*, 41:225–370, 1998. 1
- [B<sup>+</sup>00] R. Barth et al. GSI Multi-Branch System User Manual. *GSI*, 2000. 15
- [Bal93] P. Baltes. Entwicklung eines modularen datenaufnahmesystems auf transputerbasis zur auslese der vieldrahtkammern am kaonenspektrometer. Master’s thesis, Technische Hochschule Darmstadt, Germany, 1993. 15
- [BB82] Bethe H. A. Brown, G. E. and G. Baym. Supernova theory. *Nuclear Physics A*, 375:481, 1982. 3
- [BCM97] E. L. Bratkovskaya, W. Cassing, and U. Mosel. Analysis of kaon production at SIS energies. *Nucl. Phys.*, A622:593–604, 1997. 8
- [Bec93] P. Beckerle. Aufbau und test eines detektorsystems zur bestimmung der strahlintensitaet fuer messungen am kaonenspektrometer. Master’s thesis, JWG-Uni Frankfurt am Main, Germany, 1993. 13
- [Bel66] R. E. Bell. Comparison of leading-edge and crossover timing in coincidence measurements. *Nuclear Instruments and Methods A*, 42:211, 1966. 20

- [BG95] Hartnack C. Stoecker H. Bass, S. A. and W. Greiner. Azimuthal correlations of pions in relativistic heavy-ion collisions at 1 GeV/nucleon. *Phys. Rev. C*, 51:3343–3356, 1995. 62
- [BHSG93] S. A. Bass, C. Hartnack, H. Stoecker, and W. Greiner. Out-of-plane pion emission in relativistic heavy ion collisions: Spectroscopy of delta resonance matter. *Phys. Rev. Lett.*, 71:1144–1147, 1993. 62
- [Bra05] E. Bratkovskaya. Private communication, 2005. vii, viii, 59, 60, 61, 65, 66, 67, 69, 71
- [CTBR03] W. Cassing, L. Tolos, E. L. Bratkovskaya, and A. Ramos. Antikaon production in A + A collisions at SIS energies within an off-shell G-matrix approach. *Nucl. Phys.*, A727:59–94, 2003. vii, viii, 59, 60, 61, 66, 67, 71
- [E<sup>+</sup>04] S. Eidelman et al. Review of Particle Physics. *Physics Letters B*, 592:1+, 2004. 20
- [EKL89] K. J. Eskola, K. Kajantie, and J. Lindfors. Quark and gluon production in high-energy nucleus-nucleus collisions. *Nucl. Phys.*, B323:37, 1989. 25
- [F<sup>+</sup>03] A. Förster et al. First evidence for different freeze-out conditions for kaons and antikaons observed in heavy-ion collisions. *Phys. Rev. Lett.*, 91:152301, 2003. 69
- [För03] A. Förster. *Produktion und Propagation von K<sup>+</sup>- und K<sup>-</sup>-Mesonen in Au+Au-Reaktionen bei einer kinetischen Strahlenergie von 1.5 AGeV*. PhD thesis, Technische Universität Darmstadt, 2003. xi, 7, 38, 43, 51, 56, 58, 62, 64, 68, 69
- [G<sup>+</sup>84] H. A. Gustafsson et al. Collective flow observed in relativistic nuclear collisions. *Phys. Rev. Lett.*, 52:1590–1593, 1984. 5
- [G<sup>+</sup>90] H. Gutbrod et al. Squeeze-out of nuclear matter as a function of projectile energy and mass. *Phys. Rev. C*, 42:640–651, 1990. 45
- [GEBT94] Mannque Rho G. E. Brown, Chang-Hwan Lee and Vesteinn Thorsson. From kaon-nuclear interactions to kaon condensation. *Nucl. Phys. A*, 567:937–956, 1994. 3, 59
- [Gei93] G. Geiermann. Aufbau und Test der Auswert-Elektronik einer Vieldrahtproportionalzählkammer am Kaonenspektrometer, master's thesis. *Fachhochschule Darmstadt (D), Fachbereich Automatisierungstechnik*, 1993. 13
- [Gla] R. J. Glauber. High-energy collision theory. In \*Lo, S.Y. (ed.): Geometrical pictures in hadronic collisions\*, 83-182. (see Book Index). 14

- [Gro93] CN ASD Group. Detector description and simulation tool. *Program Library W5013*, CERN(3.21Ed.), 1993. 19, 22, 23, 74, 76
- [H<sup>+</sup>98] C. Hartnack et al. Modelling the many-body dynamics of heavy ion collisions: Present status and future perspective. *Eur. Phys. J.*, A1:151–169, 1998. 66, 71
- [HA04] C Hartnack and J Aichelin. Analysis of kaon spectra at SIS energies - What remains from the kn potential? *Journal of Physics G: Nuclear and Particle Physics*, 30(1):S531–S536, 2004. 66, 69, 71
- [Heh90] J. Hehner. Bau einer Vieldraht Proportional Kammer zum Nachweis ionisierender Strahlung, master's thesis. *Fachhochschule Wiesbaden (D)*, 1990. 13
- [HOA03] C. Hartnack, H. Oeschler, and J. Aichelin. What determines the K- multiplicity at energies around 1 AGeV to 2 AGeV? *Phys. Rev. Lett.*, 90:102302, 2003. 69
- [JSBB97] Igor N. Mishustin J. Schaffner-Bielich and Jakob Bondorf. In-medium kaon production at the mean-field level. 625:325–346, 1997. iii, 4
- [KN86] D. B. Kaplan and A. E. Nelson. Strange goes on in dense nucleonic matter. *Phys. Lett.*, B175:57–63, 1986. 3, 59
- [Ko84] C. M. Ko. Effect of final state interactions on subthreshold K- production in heavy ion collisions. *Phys. Lett.*, B138:361–364, 1984. 3
- [Koc05] P. Koczon. Private communication, 2005. iv, 16
- [L<sup>+</sup>93] Y. Leifels et al. Exclusive studies of neutron and charged particle emission in collisions of Au-197 + Au-197 at 400-MeV/nucleon. *Phys. Rev. Lett.*, 71:963–966, 1993. 45
- [L<sup>+</sup>99] F. Laue et al. Medium effects in kaon and antikaon production in nuclear collisions at subthreshold beam energies. *Phys. Rev. Lett.*, 82:1640–1643, 1999. 61
- [Lab05] Argonne National Laboratory. Experimental Physics and Industrial Control System. <http://www.aps.anl.gov/epics/docs/>, 2005. 16
- [Li] Brown G. E. Li, G.Q.  $K^-/K^+$  ratios in relativistic heavy-ion collisions. *nucl-th/9804013*. 61
- [LK96] Guo-Qiang Li and C. M. Ko. Antikaon flow in heavy-ion collisions: Effects of absorption and mean-field potential. *Phys. Rev.*, C54:2159–2162, 1996. 8



- [LKB96] Guo-Qiang Li, C. M. Ko, and G. E. Brown. Kaon azimuthal distributions in heavy ion collisions. *Phys. Lett.*, B381:17–22, 1996. iii, 7, 66
- [LKB98] Guo-Qiang Li, C. M. Ko, and G. E. Brown. RBUU Stony Brook calculation - Private communication, published in Y. Shin et al. PRL 81 (1998). 1998. 7, 64, 66
- [LKL95] Guo-Qiang Li, C. M. Ko, and Bao-An Li. Kaon flow as a probe of the kaon potential in nuclear medium. *Phys. Rev. Lett.*, 74:235–238, 1995. 4
- [LLB97] Guo-Qiang Li, C. H. Lee, and G. E. Brown. Kaon production in heavy-ion collisions and maximum mass of neutron stars. *Phys. Rev. Lett.*, 79:5214–5217, 1997. 4
- [LP00] J. M. Lattimer and M. Prakash. Nuclear matter and its role in supernovae, neutron stars and compact object binary mergers. *Physics Reports*, 333-334:121, 2000. 3
- [M<sup>+</sup>00] M. Menzel et al. First measurement of antikaon phase-space distributions in nucleus nucleus collisions at subthreshold beam energies. *Phys. Lett.*, B495:26–32, 2000. 69
- [MBSB<sup>+</sup>04] A. Mishra, E. L. Bratkovskaya, J. Schaffner-Bielich, S. Schramm, and H. Stocker. Kaons and antikaons in hot and dense hadronic matter. *Phys. Rev.*, C70:044904, 2004. vii, viii, 59, 60, 61, 66, 67
- [Mis04] D. Miskowiec. *Overlap* computer program. <http://www-linux.gsi.de/misko/overlap>, 2004. iv, 27, 28
- [Oes01] Helmut Oeschler. Review of SIS experimental results on strangeness. *J. Phys.*, G27:257–266, 2001. 3
- [Oll95] J. Y. Ollitrault. Collective flow from azimuthal correlations. *Nucl. Phys. A*, 590:561c–564c, 1995. 6, 28
- [Oll97] Jean-Yves Ollitrault. Reconstructing azimuthal distributions in nucleus-nucleus collisions. 1997. 33
- [Pł099] M. Płoskoń. Slow control for Kaos experiment. *ISSP 1999 GSI report*, 1999. iv, 16, 17
- [R<sup>+</sup>84] R. E. Renfordt et al. Stopping power and collective flow of nuclear matter in the reaction Ar+Pb at 0.8-GeV/u. *Phys. Rev. Lett.*, 53:763–766, 1984. 5
- [S<sup>+</sup>90] P. Senger et al. A Start Detector for the Kaon Spectrometer. *GSI Scientific Report*, GSI (1991), 1990. 12

- [S<sup>+</sup>93] P. Senger et al. The Kaon Spectrometer at SIS(GSI). *Nuclear Instruments and Methods A*, 327:393, 1993. 9
- [S<sup>+</sup>98] Y. Shin et al. Enhanced out-of-plane emission of K<sup>+</sup> mesons observed in Au + Au collisions at 1-A-GeV. *Phys. Rev. Lett.*, 81:1576–1579, 1998. iii, 6, 7, 56, 64
- [S<sup>+</sup>02] C. Sturm et al. Kaon and antikaon production in dense nuclear matter. *J. Phys.*, G28:1895–1902, 2002. 3
- [Sar91] A. Sartorius. Aufbau und Test einer Vieldrahtproportionalkammer zum Teilchennachweis am Kaonenspektrometer, master's thesis. *Technische Hochschule Darmstadt (D)*, 1991. 13, 22
- [SHG] W. Scheid, J. Hofmann, and W. Greiner. Nuclear shock waves in relativistic heavy ion collisions. In \*Berkeley 1974, Proceedings, Lawrence Berkeley Lab Lbl-3675\*, Berkeley 1974, 1-50. 5
- [Stu01] C. Sturm. *K<sup>+</sup> Produktion in Schwerionenreaktionen als Sonde fuer die Inkompressibilitaet von Kernmaterie*. PhD thesis, Technische Universitat Darmstadt, Germany, 2001. 14, 22, 43, 76
- [SV96] Y. Zhang S. Voloshin. Flow study in relativistic nuclear collisions by fourier expansion of azimuthal particle distributions. *Zeitschrift für Physik C Particles and Fields*, 70:665–671, 1996. 29
- [U<sup>+</sup>04] F. Uhlig et al. Observation of different azimuthal emission patterns for K<sup>+</sup> and of K<sup>-</sup> mesons in heavy ion collisions at 1 - 2 AGeV. 2004. vii, viii, 7, 56, 58, 63, 64, 65, 66, 69
- [Uhl04] F. Uhlig. *Systematische Untersuchung der Emission geladener Teilchen in Ni+Ni-Reaktionen bei SIS-Energien*. PhD thesis, Technische Universitat Darmstadt, Germany, 2004. 19, 22, 51, 62, 64, 65, 68
- [W<sup>+</sup>00] A. Wagner et al. The emission pattern of high-energy pions: A new probe for the early phase of heavy ion collisions. *Phys. Rev. Lett.*, 85:18–21, 2000. 47
- [Wag92] A. Wagner. Flugzeitmessung am kaonenspektrometer. Master's thesis, Technische Hochschule Darmstadt, Germany, 1992. 12
- [Wag96] A. Wagner. *Systematische Untersuchung symmetrischer Schwerionenreaktionen: Pionen als Sonden der Reaktionsdynamik*. PhD thesis, Technische Hochschule Darmstadt, Germany, 1996. 22, 62
- [WFFGB99] Z. S. Wang, C. Fuchs, Amand Faessler, and T. Gross-Boelting. Kaon squeeze-out in heavy ion reactions. *Eur. Phys. J.*, A5:275–283, 1999. iii, 7, 64, 65, 66

- [WKW96] T. Waas, N. Kaiser, and W. Weise. Effective kaon masses in dense nuclear and neutron matter. *Phys. Lett.*, B379:34–38, 1996. 3, 59

### Acknowledgments

Thank You, God, for the Big Bang... and its consequences!

I would like to thank to my supervisors, Prof. Dr. Peter Senger and Prof. Dr. Herbert Ströbele for their great support, knowledge and experience from which I could learn and profit extensively. In the same spirit I would like to express my gratitude to Priv.-Doz. Helmut Oeschler of whom the scientific knowledge in conjunction with the sense of humor and life has made me grow. Many thanks to the management of the GSI and IKF Frankfurt heavy-ion divisions in which I have been working. Specially, I would like to thank Prof. Dr. Peter Braun-Munzinger, Prof. Dr. Reinhard Stock and Prof. Dr. Harald Appelshäuser for their constant and firm support.

Enormous amount of acknowledgments and by far not underestimated *Thank You!* goes to my fellow colleagues Dr. Andreas Förster and Dr. Florian Uhlig for their superb support in the exploration of the world of KaoS, physics and daily life. Thank You! Dr. Ingrid Kraus, Dipl. Phys. Simon Lang and Dipl. Phys. Alexander Schmah for Your friendship, help and fantastic atmosphere in our office at GSI.

Many thanks to all of the KaoS collaboration members for the opportunity to work with such a great group of people. Thank You for all the discussions I could profit from and Your constant support.

I would also like to thank Dr. Elena Bratkovskaya and Dr. Christoph Hartnack for their theoretical input to this story. Many thanks to Dr. Piotr Koczon for his consulting on the technical issues of KaoS.

Infinite thanks to my fantastic Parents and Family for their help, support and for making me sure I can count on You in absolutely any situation.

Thank You Agnieszka! ... for so many things, impossible to list.

# **LEBENS LAUF**

---

## PERSÖNLICHE DATEN

Name: **Płoskoń**  
Vornamen: Mateusz Andrzej  
Geburtsdatum: 16 November 1977  
Geburtsort: Krakau, Polen

## **SCHULAU SBILDUNG, STUDIUM**

---

1984 – 1992 Aniela Krzywoń Grundschule in Krakau  
1992 – 1996 König Jan III Sobieski Lyzeum in Krakau  
Mai 1996 Abschluss: Abitur  
1996 – 2001 Studium an der Jagellonian Universität in Krakau  
im Fachbereich Physik  
Mai 2001 Abschluss: Master  
Thema der Diplomarbeit: „Experimente mit CVD  
Diamantdetektoren für Schwerionenstrahlen bei relativistischen  
Energien“  
(in Zusammenarbeit mit der Justus-Liebig Universität Giessen und  
der Gesellschaft für Schwerionenforschung mbH, Darmstadt im  
Rahmen der HADES Kollaboration)  
seit Oktober 2001 Promotionstudium an der J.-W.-Goethe Universität in Frankfurt  
am Main im Fachbereich Physik  
Wissenschaftlicher Mitarbeiter an der GSI Darmstadt  
(HADES und KaoS Kollaborationen)

# **CURRICULUM VITAE**

---

## **PERSONAL DATA**

Surname: **Płoskoń**  
Names: Mateusz Andrzej  
Date of birth: 16 November 1977  
Place of birth: Cracow, Poland

## **EDUCATION, STUDIES**

---

1984 – 1992 Aniela Krzywoń Elementary School in Cracow  
1992 – 1996 King Jan III Sobieski Lyceum in Cracow  
Mai 1996 Conclusion: Matura  
1996 – 2001 Under graduate studies at Jagellonian University in Cracow  
in the Nuclear Physics Department  
Mai 2001 Conclusions: Master  
Title of the diploma thesis: „Experiments with CVD Diamond  
Detectors for heavy-ion beams at relativistic energies“  
(in collaboration with Justus-Liebig Universität Giessen and  
Gesellschaft für Schwerionenforschung mbH, Darmstadt within  
the HADES Collaboration)  
since October 2001 PhD studies at J.-W.-Goethe University in Frankfurt am Main in  
the Nuclear Physics Institute  
Scientific coworker at GSI Darmstadt  
(HADES and KaoS Collaborations)